Comparison of very high order (O3–18) flux and Crowley flux, and (O3–17) WENO flux schemes with a 2D nonlinear test problem

Straka, J. M. ORCID: https://orcid.org/0000-0003-3672-5858, Kanak, K. M. ORCID: https://orcid.org/0000-0003-3479-9669 and Williams, P. D. ORCID: https://orcid.org/0000-0002-9713-9820 (2023) Comparison of very high order (O3–18) flux and Crowley flux, and (O3–17) WENO flux schemes with a 2D nonlinear test problem. Quarterly Journal of the Royal Meteorological Society, 149 (757). pp. 3669-3710. ISSN 1477-870X doi: 10.1002/qj.4579 Available at https://centaur.reading.ac.uk/113477/

To link to this article DOI: http://dx.doi.org/10.1002/qj.4579

Publisher: Wiley

Straka Jerry M (Orcid ID: 0000-0003-3672-5858)
Kanak Katharine M. (Orcid ID: 0000-0003-3479-9669)
Williams Paul D. (Orcid ID: 0000-0002-9713-9820)

Comparison of very high order (O3–18) flux and Crowley flux, and (O3–17) WENO flux schemes with a 2D nonlinear test problem

Jerry M. Straka*
University of Oklahoma
Norman, Oklahoma, USA
ORCID: https://orcid.org/0000-0003-3672-5858

Katharine M. Kanak
Norman, Oklahoma, USA
ORCID: https://orcid.org/0000-0003-3479-9669

Paul D. Williams
Department of Meteorology, University of Reading
Reading, England UK
ORCID: https://orcid.org/0000-0003-3672-5858

Submitted to:

Quarterly Journal of the Royal Meteorological Society

Revision submitted: 9 June 2023

Original submitted: 16 January 2023

Corresponding Author:
Jerry M. Straka*
5113 Ladbrook Street
Norman, Oklahoma, USA 73072
Phone; 405-664–3907
email: jerrystraka@gmail.com
Prof. Emeritus School of Meteorology
University of Oklahoma, Norman, Oklahoma 73072

ABSTRACT

A two-dimensional, non-linear diffusion-limited colliding plumes simulations were used to demonstrate the improved solution accuracy with very high order O9–18 flux schemes, including upwind-biased and even-centred constant grid flux and Crowley constant grid flux schemes, and odd order weighted essentially non-oscillatory (WENO) flux schemes, along with variations and hybrids of these. All schemes were coupled with comparably high order even-centred Lagrangian interpolations and pressure gradient/divergence approximations, and O18 spatial filtering. Subgrid-scale (SGS) turbulent flux calculations, with a constant eddy-mixing coefficient, were made with O2 spatial approximations (O4–20 accurate SGS turbulent fluxes had little impact). Using a range of resolutions from $\Delta x = \Delta z = 25$–166.66… m for all schemes comparisons against an O17 flux, 25 m resolution reference solution showed solutions made with ≥ O9 fluxes produced (often substantially) improved solutions, both visually and usually objectively, compared to solutions produced with lower order (<O9/10) fluxes, especially at intermediate resolutions (33.33–100 m). Expectedly, odd order solutions were increasingly damped as accuracy was decreased, especially from O9 to O3, especially for WENO solutions, while even order solutions were increasingly contaminated with dispersion and aliasing errors as accuracy was decreased, especially from O10 to O4. Odd order schemes also produced better solutions than even order schemes for <O9/10 fluxes, while the highest order (≥ O13/14) schemes produced the best solutions, for any given resolution. Even order flux and Crowley flux (WENO) solutions were the least (most) computationally expensive, based on either floating-point operations (FPO) or CPU times. Efficient WENO-Sine and proposed hybrid Crowley-WENO(-Sine) schemes required fewer FPOs to produce more accurate solutions than traditional WENO schemes. We are encouraged by the often much improved visual and objective accuracy of very high order (≥ O9) fluxes in simulations of a complex problem, and encourage further testing in numerical weather prediction models

1 | INTRODUCTION

Very few studies have considered very high, ninth through eighteenth, order of accuracy (O9–18; hereafter, O denotes order-of-accuracy), upwind-biased odd order or centred even order advective flux finite difference approximations in the atmospheric sciences, nor have more common ≥O9 flux schemes been compared. To address this, the purpose of this paper is to evaluate accuracy and computational cost effectiveness, through visual evaluation and objective error measures, of traditional O3–18 constant grid flux, dimension-split O3–18 constant grid flux Crowley (Crowley 1968 C68; Smolarkiewicz 1982 S82; Schlesinger 1984; Tremback et al. T87; Bott 1989; Costa and Sampio 1997; Wicker and Skamarock 2002 WS02; etc.), and O3–17 weighted essentially non-oscillatory WENO flux schemes (Jiang and Shu 1996 JS96; Shu 1997 S97; Balsara and Shu 2000 BS00; Shu 2003 S03; Borges et al. 2008; Geroylmos et al. 2009 G09; etc.) for a slow (e.g., advection and turbulence modes) and fast (e.g., sound and sometimes gravity-buoyancy modes) mode-split system of equations (e.g., Skamarock and Klemp 1992) using a nonlinear diffusion-limited 2D colliding plumes problem. These types schemes are chosen as they form a relatively simple basis for many other schemes, with lower ≤O7 order versions widely used in the atmospheric sciences and ≤O9 in the gas dynamics communities. All solutions produced in this study are made with comparable or higher order numerical approximations for both interpolations wherever odd-grid calculations are needed as well as for calculations of the pressure gradient and divergence calculations in the momentum equations and divergence term in the pressure equation. Higher order (e.g., O4–18) subgrid-scale (SGS) turbulent flux approximations had little impact on solutions (Straka et al. 2023; SWK23) and, thus are not presented.

Odd order schemes generally have better phase errors compared to one-order lower even schemes, while even order schemes have better amplitude errors than one-order lower odd schemes (T87). None of the schemes were combined with flux limiters (e.g., Leonard 1991 L91; Balsara and Shu

2002) for this study. Other important types of advection and flux scheme constructs, such as finite-volume, finite-element, compact, spectral/pseudo-spectral, etc., schemes were not considered herein, but should be considered in the future.

High order advection computations based on upwind-biased odd order and centred even order traditional flux or Crowley-type flux schemes (including higher derivative terms) can be made with constant grid-based interpolation coefficients (T87), which are based on Lagrangian interpolations and adjusted so that they have the same order of error as pure advective schemes for constant advective velocity and grid spacing (T87; interpolation coefficients for constant grid flux are identical to the reconstruction coefficients used in WENO schemes S97). Higher order integrated flux schemes for odd and even order for traditional flux and Crowley flux schemes can also be based on unadjusted Lagrangian interpolations for either unstretched or stretched / irregular grids. While seemingly high order, their accuracy is not equivalent to pure advective schemes when the advective velocity and grid increment are constant and have been demonstrated to be less accurate (T87). Use of an analytical function and its derivative can be used to demonstrate that constant grid flux schemes converge at the order of the scheme, while integrated flux schemes only converge at O2 regardless of the order of the interpolation (SWK23, in review; thus, not shown here), consistent with T87. All non-WENO odd order schemes used in this study were one point-biased, although they could be constructed as up to N-point upwind-biased schemes, where N is order of accuracy. The reconstruction polynomials, which are used to compute the fluxes for WENO schemes, are numerically identical to the constant grid flux polynomials, but found by alternative methods (e.g., Shu 1998). Vertical advection terms for of scalars can be integrated for mode-split simulations on the slow time step, or on the fast mode time step using multiple small time steps to accommodate fast moving gravity waves, with the former used herein.

Traditional odd and even order higher-order advection/flux schemes are simple to implement and computationally very efficient. In addition, these flux schemes are very accurate, especially for smooth flows. However, they are subject to the production of aliasing and high frequency dispersion errors, especially near sharp gradients and discontinuities (S97), and thus require the use of flux-limiters (e.g., Bott 1989; L91; S97; BS00; etc.) and/or spatial filters (Shuman 1957; Shapiro 1970; S82; Purser 1987 P87; Purser and Leslie 1988 PL88) to control numerical "noise", especially for low-order even-centred schemes. Odd order flux schemes, which inherently damp solutions, although to a lesser extent as accuracy is increased (e.g., T05), typically require less spatial filtering than even order flux schemes.

Stable time integration for traditional flux schemes in compressible models with the slow modes (advection, diffusion, etc.) split from the fast modes (sound and gravity waves), called mode-split systems, can be accomplished with explicit two-stage O2 or three-stage O3 Runge-Kutta (RK) schemes (WS02), O4 RK4 schemes (Park and Lee 2009), as well as with some filtered leapfrog schemes (Asselin 1972; Park and Lee 2009; Williams 2009, 2011, 2013; Williams et al. 2022), among others [e.g., explicit O3 (for linear systems, O2 for non-linear systems) Adams-Bashforth-Moulton Wicker 2009].

The forward-in-time multidimensional advective or flux form type Crowley schemes (e.g., C68) can be stabilised using properly implemented dimension-split (often called time-split) approaches or by the use of explicit cross derivatives (e.g., C68; S82; Schlesinger 1985 S85; T87; Bott 1989; Easter 1993; Costa and Sampio 1997). Crowley schemes can be used in mode-split models with the two-step approach proposed by WS02 for the velocity and pressure variables, or by solving the momentum equations on the small timestep, the fast-mode part of the time integration as proposed by Walko and Avissar (2008). Most applications of Crowley schemes have used stabilising derivatives up to order N for an N-order Crowley scheme. Smolarkiewicz (1982) used a stabilising second-order derivative, but commented that the first derivative advection or flux could be approximated using any higher order scheme. As described by T87, even (odd) derivative terms in Crowley schemes mostly impact amplitude (phase) errors. Multi-dimensional, dimension-split schemes, including Crowley schemes, have been shown to produce artificial gradients (Clappier 1998) owing to errors with diagonal advection/flux in flows with deformation for at least some systems of equations. Fortunately, these artificial gradients can be eliminated by correctly formulating the flux using a very simple flux correction, which requires minimal code changes. While WS02 suggested using the Clappier (1998) flux correction, they did not use it in their mode-split Crowley scheme demonstration using the S93 density current problem, but were still successful in using the Crowley mode-split time integration scheme. Positive definite area-preserving integrated flux Crowley schemes based on nonlinearly normalising and limiting fluxes (applicable to other types of flux schemes) for up to O4 were presented by Bott (1989) and to O5–8 by Costa and Sampio (1997), along with many others who presented variations described in the literature, and these schemes been shown to be accurate and efficient, but are not considered herein. Finally, Smolarkiewicz (1985) showed that the time accuracy of the Crowley scheme for non-constant velocities could be increased from O1 to O2 by simply using the advecting velocity at time level n+1/2, denoted by $v^{n+1/2}$, after each dimensional direction update in the advection/flux computations. Values of $v^{n+1/2}$ can be obtained by using the average of the n* and n time level velocities $v^{n+1/2} = 0.5(v^* + v^n)$, or by using extrapolated velocites at time levels n-1 and n, $v^{n+1/2} = 0.5(3v^n - v^{n-1})$. However, it is not known how the WS02 mode split Crowley affects the Smolariewicz (1985) procedure in attempting to achieve O2 temporal accuracy. Thus, this procedure was not used in the results presented in the current study, as preliminary test results were somewhat encouraging to mixed.

The WENO schemes, and their many variants, are widely popular in many areas of fluid dynamics, and to a lesser extent in atmospheric and ocean sciences, and have been shown repeatedly to provide excellent solutions for non-viscous fluid problems with very complex flows and sharp boundaries/shocks. Most WENO schemes are odd order, although high order central WENO schemes for O4, 6 and 8 have been developed (e.g., Qui and Shu 2002), and can be more efficient than odd order WENO schemes. Care must be taken with some central WENO schemes to avoid negative linear weights. High computational cost associated with WENO schemes is perhaps one reason WENO schemes have not been used as often in atmospheric sciences compared to other schemes. Nevertheless, two O3–9 WENO scheme variations are available in Bryan's CM1 model (Cloud Model 1; Bryan 2021 B21, https://www2.mmm.ucar.edu/people/bryan/cm1/), and at least one O3–9 WENO scheme variation is available in at least some versions of NCAR's Weather Research and Forecast model (WRF), O3–5 WENO schemes in the Meso-NH model (Lunet et al. 2017), among other models in the atmospheric and oceanic sciences (e.g., TML05 for idealised advective atmospheric related test problems). Some of the desirable characteristics of WENO schemes include being able to stably preserve gradients, maintain non-oscillatory behaviour (although WENO schemes are not necessarily monotonic) by limiting dispersion error, and minimise dissipation of extrema near steep gradients and discontinuities through the use of nonlinearly weighted combinations of upwind, downwind, and centred (for some orders) local reconstruction polynomials for the fluxes. Examples are three third order fluxes for a fifth order scheme, four fourth order fluxes for a seventh order scheme, five fifth order fluxes for a ninth order scheme, etc., in regions of smooth flow, yet will maintain approximately third, fourth, fifth, etc. order near discontinuities, respectively; see references above, especially S97, for comprehensive explanations and descriptions for constructing WENO schemes.

While the WENO schemes can produce excellent solutions for complex non-viscous problems, especially higher >O5 solutions, these schemes become increasingly computationally expensive, with floating-point operation FPOs numbers related to R to the third power, where order O = 2R–1. In comparison, the traditional comparably high order advection or flux schemes have FPO numbers related to related to order of the scheme, and Crowley schemes have FPOs numbers related to the scheme order to the second power. Much of the computational cost of WENO schemes is associated with computing the smoothness indicators (e.g., S97; G09; Wu et al. 2020 W20; Wu et al. 2021 W21). However, W20 and W21 recently described simpler, very accurate smoothness indicators (exact for sine-waves), which are much more efficient than traditional ≥ O7 WENO schemes. The WENO-sine scheme makes the computational cost of implementing WENO related to R to the second power, rather than R to the third power for traditional WENO smoothness indicators. This cost need should not be considered excessively restrictive for using WENO schemes for numerical integration in studies of complex atmospheric problems and numerical weather prediction, as the flux computations are often only five to ten percent of the total cost (e.g., TML05). Finally, WENO schemes, as well as basic flux schemes, can be stably integrated in slow/fast mode-split models with various three-stage O3 Runge-Kutta schemes RK3 (Williamson 1980; Shu 1988; Shu and Osher 1988; WS02; Baldauf 2008; where RK3 in general is O2 for non-linear system time integrations and O3 for only linear system time integrations; Purser 2007; Baldauf 2010; Lunet et al. 2017).

A hybrid-WENO-Crowley odd order dimension-split scheme is also proposed in this study in an attempt to maintain the desirable characteristics of WENO schemes and offset a portion of the computational expense of the WENO scheme when used with Runge-Kutta time integration schemes. The proposed hybrid scheme simply uses O3–17 WENO fluxes for the advection flux terms, which are then coupled with the N-derivatives required for stability for Crowley schemes, with the N-derivative differenced with higher order constant grid fluxes. Time integration is stably carried out with the WS02 mode-split forward scheme for Crowley schemes. A higher order hybrid-WENO-Crowley scheme can allow for a combination of the desirable aspects of WENO schemes when simulating flows with sharp gradients and/or discontinuities and also be amenable to stable time integration with a simpler forward scheme, which reduces computational cost relative to RK3 time integration. The hybrid-WENO-Crowley scheme can incorporate the W20 and W21 WENO-Sine smoothness indicators to further reduce computational cost.

Some motivating questions for this study include: 1) first and foremost, which of the high order numerical schemes discussed above can most accurately simulate the nonlinear diffusion-limited 2D colliding plumes test problem by providing the most accurate representation of both physically important, but marginally resolved (6–10 Δx) flow features, as well as well-resolved and smooth features of the solutions in their thermodynamic fields, kinetic energy fields, and derivative kinematic fields (e.g., deformation and vorticity), using O3–18 flux approximations and 25–166.66 m spatial resolutions?; 2) which of these schemes can best accomplish high accuracy with high computational efficiency?; and 3) are there variations and combinations of these schemes that are more accurate and/or more efficient than the others? Objective error measures are obtained using the O17 flux scheme and 25 m grid resolution, nearly grid-converged, diffusion-limited solution of the 2D colliding plumes problem for a reference. The solutions all were integrated in time with relatively small timesteps to minimize temporal truncation errors. Both a brief description of the model and a description the design of the 2D colliding plumes problem are included in section 2. A reference solution as then described and serves as the basis for comparisons and visual comparisons and computed objective errors in section 3, as are the results and discussion of the results. A summary of the findings and the conclusions are presented in section 4.

2 | METHODS

The 3D fully-compressible model used in this study was based on the Euler equations cast in a conservative flux form for dry or moist dynamics on the staggered C-grid, following concepts discussed by Bryan and Fritsch (2002 BF02), Morrison and Bryan (2012), and B21, and nearly conserves mass and energy. Fast sound and gravity waves and slow advective and turbulent modes were split into a fast/slow time-split system of equations (Skamarock and Klemp 1992), and stably integrated by including divergence damping on the fast-mode time steps (Skamarock and Klemp 1992). The divergence damping coefficient was kept very small to minimise errors from its use (Lian et al. 2022). Importantly, divergence damping differencing has formal temporal and spatial accuracy of only O1 and O2, respectively. The turbulence scheme and spatial filtering were integrated in time with accuracy of O1 forward-in-time for Crowley, and O2 for nonlinear RK3 time integrations by computing these terms on all three RK3 stages. Flux schemes used were the traditional constant grid flux, dimension-split constant grid flux Crowley (T87), and WENO flux (e.g., JS96; S97; BS00; G09). Turbulent-fluxes for all variables, except for pressure, were computed using O2 numerical approximations and a constant eddy-mixing coefficient, which allowed for a diffusion-limited nearly grid-converged reference solution when spatial (and temporal) resolution was sufficiently reduced. Extensive tests reported elsewhere (SWK23) showed that higher order (O4–18) numerical approximations for constant eddy-mixing for constant constant grid flux or Lagrangian integrated flux based SGS turbulent fluxes had little impact on RMS errors of fully compressible colliding plume solutions. The minimal impact of higher order SGS turbulent fluxes was a result, at least in part, of differencing errors with diffusion terms not being propagated as much each timestep as they are with advection terms, rather the diffusion term errors tend to be damped locally (e.g., personal communication B. Fornberg 2019). Spatial filtering was based on the family of filters described by P87. Note that the orders associated with the high order spatial filters is the order of the derivative they are associated with and not the spatial differencing accuracy; they all are O2 accurate in space as can be seen in Fornberg's (1988) tabulations.

A descriptive summary of all numerical schemes and physics are provided in Supporting Information as Table S1 (adapted from SWK23). The Courant-Friedrichs-Lewy (CFL) conditions and critical wave number for stable RK3 solutions with linear odd and even order O1–20 advection / flux approximations following procedures described by Baldauf (2008), and for stable leapfrog even order O2–20 advection / flux approximations following Straka and Anderson (1993) for comparison, are tabulated in Appendix A as Tables AI, AII, and AIII, respectively. All constant grid flux differencing, interpolation coefficients, staggered grid coefficients for pressure gradient and divergence calculations for O1–20 schemes, and filter coefficient for even orders O2–20 are tabulated in Supporting Information tables (S2a–d) along with instructions for reproducing the reported values. The reader is referred to JS96, S97, BS00, S03, Borges et al. 2008, and G09 for instructions to construct WENO schemes as well as all coefficients. Note that the non-linear weights for WENO schemes were found using improved methods from Borges et al. 2008, rather than those proposed by Jiang and Shu (1996). Additionally, the non-linear weights for O3, 7, 11, and 15 WENO schemes suggested by Castro et al. (2011) are used. Finally, a value of ε_{min} = 1x10^{-10} (BS00) is used to prevent division by zero in computation of the nonlinear weights for the WENO scheme, while a value of ε_{max} = 1x10^{30} is used to keep the numerator in the weights from exceeding machine precision (64 bits). The exponent parameter p in the nonlinear weights for WENO fluxes can have an impact on the non-linear dissipation but not the formal accuracy of the WENO fluxes (e.g, JS96; W97; G09). This nonlinear dissipation can increase with an increasing p (e.g., G09), and thus, increasing the p can result in better control of overshoots at very sharp boundaries and shocks. Traditionally, the value of the exponent of $p=2$ is used (e.g., JS96; S97; BS00, etc.), however, a value of $p=r$ has been shown by G09 to result in more accurate solutions. The majority of WENO flux solutions shown and discussed herein are made with $p=2$, with test solutions produced and discussed for $p=r$.

Results from a comprehensive suite of simulations of a dry nonlinear 2D test problem are presented to demonstrate the impact of very-high order finite difference flux, dimension-split Crowley flux, and WENO flux schemes made using odd/even order O3/4, O5/6, O9/10, O13/14 and O17/18 numerical approximations (odd order only for WENO), combined with comparable even order Lagrangian interpolations for information required at off-grid point locations and even order staggered pressure gradient/divergence approximations (one order higher for odd order schemes; e.g., for O17 advection, O18 interpolation/pressure gradient/divergence is used). Since most studies in atmospheric sciences use at most O2–7 advection/flux, the lowest order of numerical approximations shown are O3/4. Flux correction for diagonal advection (Clappier 1998) is not used for the Crowley solutions, nor was this relatively simple correction necessary, as was also found by WS02. Simulation results for O1/2, O7/8, O11/12 and O15/16 are not shown for brevity. A summary of the spatial resolutions (166.66… (hereafter 166.66), 133.33… (133.33), 100, 66.66… (66.66), 50, 33.33… (33.33), and 25 m, time steps and domain parameters used herein, is presented in Table I. The orders of accuracy for fluxes, interpolations, and pressure gradient/divergence that comprise the simulation sets A–H are presented in Table II. All solutions were made with 64-bit mathematics, noting that round-off errors limit solution improvement beyond ~O17/18 or O19/20 for all schemes considered. Solutions in this paper were produced with the Intel compilers; 128-bit arithmetic and storage was not available with the latest Intel and GNU FORTRAN compilers.

2.1 | Efficient implementation of the Crowley schemes

The computational efficiency of an N-order Crowley scheme with N derivatives can be substantially improved, especially when a model has many scalar dependent variables. Consider the O4 flux Crowley scheme, for example, with fluxes for grid index i for some variable b(i), given by

`Flux(i+1/2) =s1+s2+s3+s4,`

where,

`s1 = (`a^1`)•(c11•b(i−1)+c12•b(i)+c13•b(i+1)+c14•b(i+2)),` s2 = (a^{2})•(c21•b(i−1)+c22•b(i)+c23•b(i+1)+c24•b(i+2)),

s3 = (a^{3})•(c31•b(i−1)+c32•b(i)+c33•b(i+1)+c34•b(i+2)),

s4 = (a^{4})•(c41•b(i−1)+c42•b(i)+c43•b(i+1)+c44•b(i+2)),

$a = u\,\Delta t\,/\,\Delta x$, is the Courant number with velocity, time step, and grid spacing given by u, Δt , Δx, respectively, and S1–4 are the terms for the O1–4 fluxes, respectively. (Note the dot • denotes multiplication.)

The fluxes can be rewritten for better computational efficiency as,

```
Flux(i+1/2) = t1•b(i−1) + t2•b(i) + t3•b(i+1) + t4•b(i+2),
```

where,

```
t1 = a•(c11+a•(c12+a•(c13+a•(c14)))),
t2 = a•(c21+a•(c22+a•(c23+a•(c24)))),
t3 = a•(c31+a•(c32+a•(c33+a•(c34)))),
t4 = a•(c41+a•(c42+a•(c43+a•(c44)))).
```

The Crowley flux term here can be written with more compact notation as,

```
Flux(i+1/2) = t(1)•b(i−1) + t(2)•b(i) + t(3)•b(i+1) + t(4)•b(i+2),
```

where,

```
t(j) = a•(c(j,i−1) + a•(c(j,i) + a•(c(j,i+1) + a•(c(j,i+2)))) for
j=1,4.
```

Importantly, the values for t1, t2, t3, and t4, or t(j) in the improved efficiency version, only need to be computed once (twice) per time step for scalars (velocity and pressure) and can be reused for each scalar in the time step. Also, the variable “a” does not have to be repeatedly taken to an integer power. Furthermore, the improved efficiency version requires dependent variables at each index in the difference stencil for scalars to be accessed only once (for the O4 flux example a total of four dependent variable accesses versus 16), both of which can be very advantageous, in terms of computer CPU and cache use, especially in models with a large number of scalar dependent variables, which is often the case for models that include aerosols, microphysics, and chemistry. This procedure theoretically results in the computational cost for even (odd) order Crowley flux schemes being equal to (twice) the ‘traditional’ odd order flux computational cost each time the flux needs to be computed. In other words, the FPO numbers become linearly related to the scheme order rather that the scheme order squared.

2.2 | Two-dimensional colliding plumes test problem

To compare the performance of a comprehensive suite of simulations using five numerical schemes, each with five orders of accuracy, and eight grid resolutions, a 2D nonlinear test problem with warm and cold spheroidal plumes colliding with each other above the ground was used. This problem was similar to the one described in Norman 2021 (N21), although with eight times smaller initial plume perturbation amplitude, as well as with inclusion of constant eddy-mixing SGS turbulent fluxes. The constant eddy-mixing SGS turbulent fluxes allow for a nearly grid-converged solution for nonlinear problems if the solution is high enough. In addition, the effects on solutions of a background mean wind of $U_t = -20$ m s^{-1} were also considered. As the plumes approach each other, vertical gradients are enhanced, and after colliding, both cold and warm air plumes spread out laterally while thermal and shear instabilities result in the development of prominent rotors. The solutions are symmetric in the horizontal, but they are not symmetric in the vertical owing to vertical gradients in density, temperature, pressure, and sound speed. Rotors of different sizes develop as the plumes spread laterally, with the rotors tending to grow upscale owing to the 2D slab-symmetry geometry of the domain (e.g., Fjortoft 1953; Soong and Ogura 1973; Appendix B includes a figure, zoomed on the left member of the symmetric circulation couplet of the colliding plumes after 1000 s using O17 fluxes, and 16.66… m resolution, in which the features discussed with respect to the results herein are denoted (the upper and lower rotors, etc.) to facilitate solution of comparisons the schemes with various orders of accuracy and resolution. The 2D colliding plume simulations produce steep gradients with strong deformation, rotation, divergence and translation kinematic characteristics, which can significantly challenge numerical schemes. The colliding plume problem has physical features and attributes, such as very sharp gradients, deformation and rotational characteristics, and smoother flow regions, which spatial grids can resolve to varying degrees. All simulations were made without the complications of physical parameterizations other than the turbulence scheme with a constant eddy diffusion coefficient and selective higher order spatial filters.

The atmosphere represented in the simulations is initially dry adiabatic (potential temperature equal to 300 K at all heights). The two plumes which collide are initiated horizontally in the centre (x = 10 km) of a 20 x 10 km x-z domain, which is periodic in the x-direction. The warm plume is centred at height z = 3050 m and the cold plume is centred at height z = 7050 m. The warm and cold plumes are prescribed by the same cosine squared function, but with potential temperature excess/deficit of $\Delta\theta = \pm 2.5$ K, respectively. The radii of both plumes are 2000 (2000) m in the x- (z-) directions. All schemes were tested with grid resolutions of $\Delta x = \Delta z$ = 25, 33.33, 50, 66.66, 100, 133.33, 166.66 m. The time steps assume a constant Courant number (C = 0.046875) with the resulting time steps given as Δt = 0.078125, 0.1041166…, 0.15625, 0.20833..., 0.3125, 0.4166, and 0.520833… (Table I). With these values all solutions are stable, although all solutions were stable with Courant numbers as large as C = 0.12, and much larger if the number of small timesteps was increased. The small Courant helped keep temporal truncation errors minimised, as discussed in SWK23. A constant eddy mixing coefficient (K_m = 10.0 m^2 s^{-1}) was applied to all variables (except pressure), which allowed for a nearly grid-converged solution when $\Delta x = \Delta z$ =25 m. A weak scale-selective O18 spatial filter (S82; P87; P88; K07) was applied in both x- and z-directions to perturbation values (from their base state; pressure was not filtered). The very small filtering coefficient used (α = 0.03) meant 2Δ spatial waves were damped 3% every time step. For comparison, a value of α = 0.24 is used in the Weather Research Forecast model (WRF; K07). The numerical spatial filter (P87) is very selective for higher wavenumber (small Δx) with coefficients for the O18 filter based on the two parameters R (rolloff) and S (smoothness); (R, S) = (18, 0) for all solutions in this paper. The spatial filter was not technically required to be as strong with odd order, upwind-biased flux scheme solutions as that needed for even order scheme solutions, and was not required at all for WENO scheme solutions, therefore, an intermediate filter coefficient α (held constant for all the schemes) was chosen so as to not overly smooth the odd order scheme solutions, or to not excessively under smooth the even order scheme solutions. Much lower values of α were able to be used for odd order schemes where higher values of α were found to be generally detrimental. On the other hand, the lower order even scheme solutions used in this paper would have significantly benefited from much stronger spatial filtering to remove large amplitude, high frequency numerical noise (dispersion error and aliasing) in the solutions presented. Use of stronger filtering for either odd and even higher order solutions would have resulted in unneeded and detrimental excessive damping of the higher order solutions. Use of a spatial filter with an order less than the order of advection/flux advection was always detrimental to the accuracy of solutions (P87, PL88), but the converse was not true.

3 | RESULTS AND DISCUSSION

3.1 | Reference solution

A nearly grid-converged reference solution (Fig. 1) was produced in order to make visual solution comparisons and calculate objective error measures based on a solution made using the odd order O17 upwind-biased constant grid flux, O18 spatial filter, O18 pressure gradient /divergence, constant eddy mixing coefficient $K_m = 10.0$ m^2 s^{-1}, $\Delta x = \Delta z = 25$ m, and $\Delta t = 0.078125$ s in order to make visual solution comparisons and calculate objective error measures. The idea of nearly grid-converged solutions herein means the flow and scalar fields become sufficiently resolved and smooth for the resolution such that the higher order derivatives become increasingly well posed and well behaved as a result of the constant eddy-mixing turbulent diffusion (or in other studies by flux-limiters; e.g., N21). As Park and Lee (2009) note, in the context of time differencing for nonlinear problems, "…the theory that a smaller time step with a low-order time-integration scheme can be better than an inefficient high-order scheme is supported only when the convergence rule is maintained" (i.e., for a linear problem). The same holds in the context of spatial differencing in that a higher spatial resolution with low-order spatial differencing can be better than a computationally intensive high order scheme. As a consequence of these concepts, "convergence" of nonlinear solutions in this study only means that the objective error measures are improving rather than converging at the theoretical linear convergence rates.

Objective error measures such root mean square RMS errors and L_∞ error norms (Fig. 2), computed for all schemes using the 25 m reference solution, for resolutions of $\Delta x = \Delta z = 25$, 33.33, 50, 66.66, 100, 133.33, and 166.66 m and fluxes of O3/4, 5/6, 9/10, 13/14, and 17/18 were used to determine which resolution could be best used for a reference solution. In addition, Richardson extrapolation (not shown) based on the $\Delta x = \Delta z = 25$ and 33.33 m solutions was used, as in Straka et al. (1993; S93), to support that the test problem solution was sufficiently grid-converged with O17 numerical approximations and $\Delta x = \Delta z = 25$ m resolution. Note that, phase errors (which vary with each scheme, as some of the solutions were not completely grid-converged for the nonlinear test problem) produced localised differences amongst the schemes. For example, in some test solutions, there were local differences from the reference solution of up to ~0.21 K in the perturbation potential temperatures, even though the simulation extrema (L_{max} and L_{min} error norms calculated against the reference solution) were identical to about four digits for all variables. Finally, as described in SWK23 for this colliding plumes problem, the L_1 error norms for perturbation potential temperature between O(3–17), 33.33 m simulations and O17, 25 m simulation, were ~4.12x10^{-3} to 1.16x10^{-3}, while L_1 error norms between the O3–17, 50 m and O17, 25 m solutions, ranged from ~4.81x10^{-3} to 3.79x10^{-3}. These error norms met the Zhang et al. (2003) L_1 error norm < 0.01 criteria to indicate near-convergence for their viscous Rayleigh-Taylor problem. The L_1 error norms 3.71x10^{-2} to 2.64x10^{-2} between O3–17, 100 m solutions and O17, 50 m solutions indicated that the 100 m solutions were not near-convergence based on the Zhang et al. (2003) criteria.

Using a spatial resolution of $\Delta x = \Delta z = 25$ m with any of the schemes produced maximums and minimums in the perturbation potential temperature, winds, and perturbation pressure fields that were generally within 0.51% of each other, with the O17, 25 m Crowley solution having the largest of these differences and largest RMS errors, and the O18 flux, O17 WENO, and O18 Crowley having the smallest differences and RMS errors from best to worst, respectively. Regardless, any of these $\Delta x = \Delta z =25$ m solutions made with O17/18 numerical approximations from any of the schemes in Set A were nearly indistinguishable and had very nearly identical maximums and minimums for up to three to four digits, as well as comparable RMS errors and L_∞ error norms. As a result, any of the O17/18, 25 m solutions made could have been used as a reference solution, without any change in the conclusions based on objective error measures (and visual appearances; analyses with different reference solutions are not shown for brevity). The O9/10–17/18, solutions made with $\Delta x = \Delta z = 25$ also were visually, very nearly indistinguishable from the reference simulation solution without any added mean wind, as were the O13/14–17/18, 25 m solutions made with an added mean wind of $U_t = -20$ m s^{-1}. Finally, it should keep in mind that numerical errors of any sort can result in buoyancy and shear instabilities to be erroneously excited or damp in problems such as the colliding plumes problem, single plume problems (Grabowksi and Clark 1991), etc., and can complicate discernment of differences owing to physical causes from those caused by numerical solution errors (Zhang et al. 2003).

3.2 | Comparisons without an added mean wind (Set A)

The results from all of the schemes, without an added mean wind were compared at $t = 1000$ s by examining solutions from all schemes made with comparably high order interpolation and pressure gradient/divergence approximations, same O18 spatial filter, same Courant number C, and $\Delta x = \Delta z = 100$ m for perturbation potential temperature (Fig. 3; Set A). Additional comparisons at $t = 1000$ s are shown for solutions with enhanced focus on in the vicinity of the marginally resolved upper rotor (Figs. 4–8) where the largest errors generally occurred for the odd order Crowley (Co; note even order Crowley Ce not shown in Figs. 4–8, but included in Supporting Information S3), odd and even constant grid flux (Fo and Fe, respectively), and WENO (W) flux schemes, comparable order interpolations and pressure gradient/divergence, same O18 filter, same Courant number C, and resolutions of $\Delta x = \Delta z = 33.33$, 66.66, and 100 m for perturbation potential temperature (Fig. 4), difference plots of between the upwind-biased constant grid flux O17, 25 m reference solution and test solutions (Fig. 5), kinetic energy per unit volume [Fig. 6; KE = 0.5 □(u_i • u_i)], 2D vorticity in the xz-plane [Fig. 7; ($\Delta u/\Delta z$-$\Delta w/\Delta x$) hereafter vorticity), and total magnitude of 2D deformation in the xz-plane {Fig. 8; [$[(\Delta w/\Delta x+\Delta u/\Delta z)^2 + (\Delta u/\Delta x - \Delta w/\Delta z)^2]^{1/2}$; hereafter deformation}, where u_i are the i=1,2,3 (u,v,w) velocity components in m s^{-1}, and ρ is the dry air density in kg m^{-3}.

As expected, higher order numerical approximations produce visually better results with respect to the upwind-biased constant grid flux O17, 25 m reference solution for all schemes for $\Delta x = \Delta z = 33.33$, 66.66, and 100 m resolutions, especially in terms of preserving the shape of the rotors. All odd / even flux and odd / even order Crowley schemes, especially the ≥ O9/10 higher order odd and even schemes, and ≤O6 even schemes, using resolutions of 66.66 and 100 m (as well as 50, 133.33 and 166.66 m not shown) produced notable (~ ≥1%; locally as high 20–40%) overshoots in the maximums and minimums of perturbations compared to the reference solution, while these overshoots were only found in the ≤O5, 25 and 33.33 m solutions (former not shown). In contrast, the ≤O9, 100 m, and ≤O13, 50 (not shown) and 66.66 m, the ≥O17, 25 (Fig. 1) and 33.33 m (Supporting Information Figure S4a) WENO flux solutions did not produce notable (~ ≥1%) overshoots in the maximums and minimums of perturbations compared to the reference solution. These behaviours are generally in agreement with G09 where ≤O9 WENO fluxes had few or no overshoots in the maximums and minimums of the scalar quantity (nearly monotonic), while ≥ O13 WENO fluxes did (not monotonic).

In spite of the overshoots, which tended to be very localized, the higher order solutions had better overall amplitude and phase errors, as well as better objective error measures including RMS errors and L_∞ error norms for potential temperature and KE made using the constant grid flux O17, 25 m reference solution (Fig. 2; RMS and L_∞). The RMS errors for potential temperature and KE fields for all schemes made with $\Delta x = \Delta z = 100$ m are also shown in Table III. By $t = 1000$ s, most schemes for the nonlinear problem used in this paper converged at best at ~O2 except for some very high order and fine resolution solutions where convergence was ~O3 and occasionally higher, (Fig. 2) with convergence rates slowly flattening at higher resolutions for <O17/18, but not for O17/18. This is similar to what N21 showed for nonlinear, shock-producing, 1D Euler simulations.

While many simulations were able to reasonably capture the resolvable and marginally resolved characteristics of the flow with $\Delta x = \Delta z = 100$ m (Fig. 3) or 133.33 m (not shown), and appear fairly similar between schemes, among like-schemes, among like-order of accuracy, and especially among the odd order schemes (Fig. 1 and Figs. 3–8), as well as among the even O10, O14, and O18 schemes, the perturbation potential temperature differences fields (Fig. 5) show some very large local differences, which were typically ~1– 2 K and occasionally larger than ± 3 K. These errors probably owe to a combination of phase and amplitude errors, and numerical dispersion and dissipation along with aliasing, all of which might not be fully appreciated from visual examination. The regions with the largest errors were especially in the regions around the boundaries of the smaller (less resolved) upper rotor and near the front and back edge of the outward (left-ward) propagating front beneath the upper rotor. Comparisons of maximums and minimums of the velocity components (not shown) have differences of 8–10% between similar order schemes (e.g., O17/18), as high as 15% for a given scheme amongst the all of the orders discussed, and an overall maximum difference of 15%. The differences in the pressure fields among the schemes were generally <5% (not shown).

Even order constant grid flux and even order constant grid flux Crowley schemes, especially the low order (O4 and O6) forms, have more prominent high frequency wave numerical noise, which can cause excitation of physical instabilities as the numerically induced high frequency waves are not well controlled. These types of errors can disrupt the evolution of the larger scale features and produce unphysical solutions, as well as exaggerated maxima, minima, etc. Importantly, the Crowley schemes have some advantage over the constant grid flux solutions in terms of reduced dispersion errors, though the Crowley schemes tend to have slightly more dissipation errors. Nevertheless, the O14 and O18 constant grid flux and constant grid flux Crowley schemes have some of the best objective error measures (objective errors for $\Delta x = \Delta z = 100$ m are tabulated in Table III, while objective errors for $\Delta x = \Delta z = 100$, 66.66, and 33.33 m are also tabulated in Table

IV along with CPU timings which are discussed later), and these were very slightly better than O13 and O17 odd order schemes. In contrast, odd-order constant grid flux numerical approximations have much less obvious dispersion/phase and aliasing errors than even order schemes (especially for <O10 fluxes), appear relatively free of numerical noise, and have the best overall visual performance and objective error measures for all orders.

Notice that the O13–17 WENO solutions using $\Delta x = \Delta z = 100$ m (Fig. 3) tend to produce a perturbation in the potential temperature field on the top left side of the interface, while none of the other solutions produce this perturbation. This same perturbation appeared in the non-viscous WENO colliding plume solutions described by N21, and appears to be associated with numerically accentuated shear and buoyancy gradients, both of which were already large, causing an unphysical feedback, based on the behaviour of the reference solution and WENO simulations with finer resolutions of $\Delta x = \Delta z = 25$, 33.33, 50, and 66.66 m for guidance, none of which have this perturbation. The objective measures (Fig. 2; Table III) show that error improvement stops and gets worse as order is increased from O13 to O17 for the 100 m WENO solutions, while all of the other schemes continue to have improved errors with increasing order. In contrast to the > O5 WENO solutions, as well as the other odd solutions with the non-WENO schemes, the O3–5 WENO solutions and especially the O3 WENO solutions, appear overly smooth with significantly smaller amplitude maxima and minima (Fig. 3–8). Moreover, the O3–5 WENO solutions (Fig. 2) are not as accurate as the odd order flux scheme solutions either visually or with objective error measures. The damped O3–5 WENO solutions herein are consistent with the well-known issue of excessive damping of gradients with O3–5 WENO schemes documented by, for example, Latini et al. 2006 and Wang et al. 2021 (WPM21). Though not shown for brevity, it is important to note that the WENO simulations show the well-known exceptional behaviour of preserving strong gradients both with and without artificial viscosity (eddy mixing and/or spatial filters), while the other schemes, especially the even order schemes, need spatial filtering.

Overall, considering all orders-of-accuracy and all resolutions tested, the results discussed for the case of no added mean wind (Set A) show that odd order constant grid flux schemes perform the best against the reference solution (as might be expected since the reference solution is obtained using the odd order constant grid flux scheme with O17, and 25 m). Additionally, the O10–18 even order constant grid flux schemes performed remarkably well for intermediate and finer grid resolutions ($\Delta x = \Delta z = 33.33$–$100$ m). However, the O4–6 even order constant grid flux solutions, and to a very slightly lesser degree the O4–6 Crowley schemes, produced solutions that were all very noisy and contaminated with significant dispersion and aliasing errors, the latter noticeable in the presence of prominent 3Δ waves, both visually identifiable and in power spectra of the velocity components, KE, vorticity, and potential temperature (not shown).

Visual inspection of the solutions in Fig. 1 and Figs. 3–8 shows that increasing the order of accuracy of approximations used to make the solutions by two to four orders is roughly comparable to making the resolution 1.5–3 times finer, consistent with Shi et al. (2003), Latini et al. (2006), and SWK23. All O9–17 solutions with $\Delta x = \Delta z = 50$ m (not shown) and 66.66 m appear nearly as good visually and perhaps better than the O3–5 solutions made with $\Delta x = \Delta z = 33.33$ m (factor of 1.5–2; in particular, see difference fields between 25 m reference and test solutions for perturbation potential temperature in Fig. 5).

The computational cost is approximated for each scheme from a theoretical perspective to avoid computer / compiler dependence as total floating-point operations (FPO) per grid point per time-step step for the three-stage RK3 mode-split time integrations using two, three, and six fast mode small time steps per slow-mode time step, for stages one, two and three, respectively times the number of grid points times the number of time steps (Fig. 9). The use of order of accuracy preserving interpolations and pressure gradient / divergence calculations results FPO numbers beyond those compared to using O2 interpolations and pressure gradient / divergence calculations as is traditionally done in most atmospheric models. Overall accuracy does not seem to be degraded if ≥O4 is used for the interpolations and pressure gradient / divergence calculations, but is for O2 (SWK23). Importantly, the use of O4 for the interpolations and pressure gradient / divergence calculations results in many fewer FPOs compared to use of comparable order of accuracy for these calculations (SWK23). Note the approximate linear increase with order of FPOs per grid point per time-step step for the flux and Crowley schemes, cubic increase for WENO schemes, and quadratic increase for WENO-sine solutions (discussed in section 3.4.2). The total FPOs in the graphs of Fig. 10 were all normalised by the $\Delta x = \Delta z = 166.66$ m O4 constant grid flux scheme FPO value (the lowest value of all schemes and resolutions considered) and are based on keeping the Courant number constant, and provides the basis which provides a relative computational cost for each scheme using with O3/4, 5/6, 9/10, 13/14, and 17/18 order numerical approximations and resolutions of $\Delta x = \Delta z = 25$, 33.33, 50, 66.66, 133.33, and 166.66 m, relative to the RMS errors for perturbation potential temperature and KE (Fig. 10). Use of a time step based on the stable CFL rather than a constant Courant number, becomes more complex, especially for the lower order (≤O5/6) solutions. First, temporal truncation errors tend to increase with longer time steps for this problem (e.g., SWK23). Second, the solutions take less time with longer, which might offset the impact of larger temporal errors.

Comparisons of computational costs based on FPOs versus potential temperature and KE RMS errors for all solutions is best seen graphically, which shows that the solutions with the best objective errors for the computational cost are solutions made at the finest resolutions with highest even order flux, odd order flux, (Fig. 10), even order Crowley solutions, while WENO solutions had significantly larger computation costs (Fig. 10). Clearly, except at the highest orders and high resolutions, most schemes are not cost-effective based on the use of the theoretical FPOs. Using near the maximum stable CFL only worsens the cost-effectiveness for each scheme. The lack of cost-effectiveness seems to be associated, at least in part, with the diffusion limited nature of the problem and temporal errors, especially temporal errors with the filter, as discussed in SWK23.

Fortunately, owing to efficient computer cache use, which can be machine dependent, can allow for significant cost-effectiveness with higher order schemes as described by, for example, Balsara an Shu (2000) and Shi et al. (2003), who showed CPU times being up to two or more times less than when estimated from FPOs. In this study, attempts at careful programing resulted in better use of faster computer caches and reduced cost for all schemes compared to expectations based on FPOs. Values for the CPU times for each scheme order along with RMS errors for perturbation potential temperature (top right of each cell) and KE (bottom left of each cell) are presented for 100, 66.66, and 33.33 m solutions in Table IV. The first set of values in the top left of each cell for each scheme order are CPU times for only the flux stencil + pressure gradient stencil + divergence stencil + interpolation stencil calculations and next to the CPU time in bold is the ratio to the lowest order scheme (O3/4) in the row. The second set of values in the bottom left of each cell for each scheme order are CPU time for only total advection + total small step + total buoyancy and next to the CPU time in bold is the ratio to the lowest order scheme (O3/4) in the row. The CPU for the SGS turbulent flux and spatial filter calculations are the same amongst Crowley solutions and same amongst RK3 solutions for any given resolution and included in the caption of Table IV. Efficient computer cache use, for example using the 100 m odd flux simulations, resulted in the ratio of the CPU time for O17 to O3 stencil calculations to be roughly only ~3.6, when theoretically using FPOs the ratio would be ~6.6 (note the flux FPOs in Fig. 9 included all calculations for fluxes, where in contrast only the stencil calculations were considered for this discussion). All calculations, including overhead calculations (e.g., dt/dx, map factor, density in the flux divergence term, etc.) needed to update dependent variables with fluxes, pressure gradient, and divergence, are significant, similar among the Crowley time integrations, similar among the RK3 time integrations, and are included in the second number in each table cell to help show why high order solutions do not dramatically increase total CPU time in comparison to much lower order solutions. In another comparison, the O17 WENO flux solution CPU times (Table IV, second number), which were dominated by the flux calculations (84–93% for O3–17 WENO fluxes, respectively), use only about ~1.5–2 times more CPU time (domain size dependent) than O3 WENO solutions, in contrast to using FPOs, for which the O17 WENO solutions could be expected to use ~10 times more CPU time that O3 WENO solutions. This made the WENO schemes much more attractive in terms of CPU time use compared to what could be expected using theoretical FPOs. The results in Table IV also show that the use of CPU times rather than FPOs to estimate cost-effectiveness allows some higher order schemes to be more competitive, at least visually, and not much more CPU compared to lower order schemes. Finally, while use of higher order numerical approximations, at least for the colliding plume problem, is not always be cost-effective, higher order numerical approximations can provide more accurate to much more accurate solutions when resolution is not changed, or cannot be changed for reasons such as limits associated with available computer memory.

3.3 | Comparisons of solutions with an added mean wind of –20 m s^{-1} (Set B)

Additional simulations, with an added mean wind of $U_t = -20$ m s^{-1}, were compared at $t = 1000$ s for all schemes made with comparably high order interpolation and pressure gradient/divergence approximations, same O18 spatial filter, same Courant number C, and $\Delta x = \Delta z = 25$–166.66 m. Use of the added mean wind proved to be more of a challenge for all schemes, as seen in the perturbation potential temperature fields (Fig. 11). As with the solutions without the added mean wind, additional comparisons were made between solutions at $t = 1000$ s in the vicinity of the marginally resolved upper rotor where the largest errors generally occurred for the odd order Crowley, odd and even order constant grid flux, and WENO flux schemes, with comparable order interpolations and pressure gradient/divergence, same O18 filter, same Courant number C, and resolutions of $\Delta x = \Delta z = 33.33$, 66.66, and 100.00 m for perturbation potential temperature (Fig. 12) and kinetic energy per unit volume (Fig. 13).

The odd order constant grid flux, odd order constant grid flux Crowley, and WENO flux schemes produced the better solutions than the even order constant grid flux and even order Crowley schemes for all orders-of-accuracy, in terms of rotor shape preservation and amplitude and phase errors, when compared to solutions without an added wind and to the reference solution from the simulations without the added wind (theoretically, the solution should be the same with and without an added mean wind due to Galilean invariance; however, the mean wind adds a further challenge to the numerical schemes not present in the no-wind simulations.) Unsurprisingly, the phase errors, which are enhanced by strong advection from the added mean wind, were minimised with the higher order approximations. The degree of improvements, which are notable and continued up to O17/18, and were somewhat unexpected. Some minor loss in symmetry in the rotor shape and flow fields (features on left side versus right side of domain) occurred with all schemes, especially with the even order schemes and spatial resolutions of 100, 66.66, and 33.33 m (all schemes and all orders are shown in Supporting Information S4) for the simulations with the added mean wind owing to variations in dispersion and phase errors in the parts of the solutions moving with and opposing the flow, especially for lower order even flux schemes. The even order Crowley schemes produced less asymmetries than for even order flux schemes, while the WENO schemes produced the least asymmetries at any order for any accuracy at any given resolution compared to the odd / even Crowley and odd even flux schemes. The asymmetries decreased with both increasing scheme orders and spatial resolutions but were still present for spatial resolutions of 33.33 m, however they were barely visible (Supporting Information S4).

Interestingly, the apparent phase errors (based on visual assessment of the placement of the leading potential temperature front (relative to the reference solution, dashed contour) are the smallest in the O17 WENO solutions made with $\Delta x = \Delta z = 100$ m (Fig. 11) compared to all of the other solutions for this resolution regardless of the order of accuracy with which they were made. Additionally, the O5, 9, 13, and 17 WENO solutions also tend to have the lowest RMS errors (Table III) for potential temperature and KE among the schemes for Set B. However, the O3–5 (and to a lesser degree O9) WENO solutions with the added mean wind have the worst visual appearance, followed by the O3 and O5 Crowley solutions, even at finer resolutions of $\Delta x = \Delta z =$ 50 and 33.33… m (not shown). The solutions made with even order flux finite difference schemes, and to a slightly lesser extent the even order Crowley schemes, were adversely affected by dispersion/phase and aliasing errors, especially those with <O10 numerical approximations, and much more so than the odd order scheme solutions. Additional spatial filtering (factor of 10 or more, higher) was needed with lower order even-centred constant grid flux schemes to control adverse dispersion and aliasing, etc. errors (not shown) enough to make them as visually free of numerical noise as the odd order solutions. However, increasing filtering strength can adversely affect the overall accuracy, especially when evaluated in terms of amplitude error. In summary, the results with the added mean wind simulations showed that the highest order odd order schemes as well as the very highest order (≥ O9) even order schemes, were remarkably accurate and had minimal numerical noise for the case with an added mean wind.

3.4 | Constant grid, Crowley, and WENO flux advection scheme hybrids and variations

Several variations of odd order versions of constant grid, Crowley, and WENO flux schemes are evaluated next, as are various hybrids of these schemes, including a hybrid-WENO/Crowley scheme. Additionally, the WENO flux schemes, integrated with three-stage O3 RK3 time integration schemes, slowly continue to gain use in the atmospheric sciences. Given the high computational cost of numerical weather models, WENO and other schemes sometimes have been used with “short-cuts” to improve efficiency. However, the evaluation of the impact of any detriment to the scheme accuracy associated with some of these implementation practices to improve computational efficiency, has not always been demonstrated and/or documented for either linear or nonlinear atmospheric problems. The impacts of some of these implementations are presented in Sets C–H using $\Delta x = \Delta z = 100$ m resolution.

3.4.1 | WENO smoothness indicator power (Set C)

Gerolymos et al. (2009) showed examples WENO of solutions with up to O17, in which the WENO scheme smoothness indicator exponent parameter by $p = R$ (denoted as WR), where order of accuracy O = 2R–1, rather than the traditional value of $p = 2$ (JS96; BS00; G09). (Note for O3 WR and W are the same with R= 2 for both). Briefly, the O5–17 WENO flux solutions shown by G09 made using a value of $p = R$ were generally more monotonic, and more accurately captured the solutions in regions of very sharp boundaries/shocks for linear and nonlinear 1D problems compared to solutions made with $p = 2$. Comparisons of examples of WENO flux scheme solutions presented herein with the smoothness indicator exponent parameter given by $p = R$ (hereafter denoted as WR), instead of the traditional value of $p = 2$ (e.g., JS96; S97), and $\Delta x = \Delta z = 100$ m resolution, showed that the perturbation potential temperature field maximums and minimums in the for O5, 9, 13, and 17 WR solutions did not over shoot values (e.g., were more monotonic) found in the reference solution. In contrast, for example, the perturbation potential temperatures maximums and minimums in the O17, 100 m solutions made using of $p = 2$ (the worse-case) by 4.7 and 23.1%, respectively. These precents decreased in the O17, 66.66 m (50 m) resolution WENO flux solutions ($p = 2$) to 2.6% (1.6%) for perturbation potential temperature maximums, with no overshoots for the minimums for either 66.66 or 5m. Minimising overshoots and better monotonic behaviour by using $p = R$ was one of the defining impacts shown and discussed by G09. However, RMS errors were somewhat degraded for O5, 9, and 13 WR perturbation potential temperature and KE solutions herein using $p = R$ (Fig. 14 rows one–three, WR, zoomed as in Figs. 4–8; Table III), although somewhat improved in for O17 WR solutions, as compared to WENO with $p = 2$ (see Figs. 4–6. It seems that using $p = R$ may have overdamped the solutions at 100 m resolutions resulting in larger RMS errors. Finer resolution solutions (e.g., $\Delta x = \Delta z = 66.66$ and 50 m) made using $p = R$ (Fig. 14 rows five–six as in Fig. 3) showed somewhat less damped solutions compared to solutions made using 100 m resolution and p = R (Fig. 14 rows four as in Fig. 3), with no overshooting maximums and minimums of perturbation potential temperatures for ≤O13, WR solutions, although there were minor overshoots for the O17, WR solutions as noted above. These higher resolution, WR solutions still had larger RMS errors than found using WENO $p = 2$. In addition, the ≥O13, 66.66 and 50 m resolution solutions had enhanced shear instabilities on the warm-cold air interface, resulting in small-scale rollups, which were not found in the reference solution. The rollups seemed to be less apparent as resolutions were made finer where diffusion could control them better, and eventually converged to the reference solution, but at finer resolutions than required for WENO solutions made with $p = 2$. In summary, the use of $p = R$ in computing WENO fluxes produced potentially both worse and better solutions are possible for the complex dynamical problem employed in this paper depending on resolution, SGS turbulence, WENO flux order, and the error metrics of most interest. Although the WR solutions were more likely to be monotonic, they had larger RMS errors, and the higher order (≥O13) solutions had more shape differences from anomalous shear instabilities at intermediate resolutions, both of which contributed to the larger RMS errors.

3.4.2 | Accurate and more efficient smoothness indicators for WENO schemes (Set C)

Recently proposed and demonstrated, efficient, sine wave-based WENO smoothness indicators (exact for sine waves; hereafter WS; W20 and W21; note that the coefficients suggested by W21 were recomputed and corrected for this paper owing to a couple of typographical errors in W21), for $R \geq 4$ (≥ O7) WENO schemes (with comparable order interpolations and pressure gradient/divergence), provided visually better solutions (Fig. 14, rows eight-ten, WS; zoomed as in Figs. 4–8) for perturbation potential temperature and KE fields, as well as better objective error measure results (Table III) when compared to solutions with the traditional smoothness indicators for O9, 13, and 17 WENO schemes given by JS96, BS00, and G09. Importantly, the anomalous perturbations in the inner front on top of the lower rotors in the original O13 and O17 WENO solutions are not produced and the maximums and minimums are much better behaved with WENO-sine scheme (compare row five in Fig. 3 with row ten in Fig. 14). (Solutions for cases with and without a mean wind for resolutions of 33.33, 66.66, 100 m are provided in Supporting Information S3, and for the nearly full domain, with and without a mean wind, for resolution of 100 m and for with a mean wind for resolutions of 33.33 and 66.66 m are provided in Supporting information 4). These newer smoothness indicators required increasingly fewer computations per grid point per time step with each increase in R when compared to traditional WENO schemes of equivalent order as there are three versus R for each stencil for $R \geq 4$. The results herein are in agreement with the findings of W21 who stated that a value of $p = 1$ provided the best solutions for the power with their smoothness indicators. The use of either $p = 2$ or $p = R$ (in general > 1) with the W21 sine-based smoothness indicators degraded the results for the perturbation potential temperature and KE fields (not shown), as W21 found and explained. These results support the use of the W21 sine-based WENO scheme smoothness indicators for the colliding plumes test problem as formulated as they provided more accurate WENO type solutions using fewer FPOs.

3.4.3 | Lower WENO approximations for stage 1 and 2 of RK3 time integrations (Set D)

One way to reduce the computational cost of implementing very high order advection schemes that are coupled to multi-stage time schemes is to use lower-order flux approximations, for example, in the 1st and 2nd stage calculations of the RK3 time scheme, followed by a very high-order advection scheme for 3rd stage. As an example of the impact of this procedure, Gadd's (1978) multi-dimensional implementation of an O4 advection scheme with a two-step Lax-Wendroff time-integration scheme, used O2 advection for the first Lax-Wendroff "half time step", followed by O4 advection in the second Lax-Wendroff "half time step", maintained the high order accuracy of the O4 advection.

The use of Gadd's approach of computing lower order advection on all but the last stage of a multi-stage time step, was applied herein on the 1st and 2nd stages of RK3/WENO integrations and is shown to be stable and accurate for the combinations considered. Specifically, tests were made for five examples with orders for the RK3 time integration stages one: two: three given by O3:3:17, O5:5:17, O9:9:17, O13:13:17 and O17:17:17 (Fig. 15, rows one-three, WL; zoomed as in Figs. 4–8). The results from these experiments show that requiring the same high order advection/flux be used for each RK3 stage is not necessary, at least from a practical view, based on perturbation potential temperature and KE fields (Fig. 15), and objective error measures (Table III; compare the values in each column with the values in the last column, as all solutions have O17 for the third stage of the RK3 time integration). Interestingly, the errors were often slightly improved for the most part for the O3:3:17, O5:5:17, O9:9:17 WENO solutions compared to using O17 WENO for all three RK3 stages. For the WL results, the order of accuracy of the interpolations and pressure gradient/divergence at each stage were all kept the same as the ones used in the last (third) stage of RK3 time integration; i.e., they were all compatible with the highest order scheme used in the last (third) stage of RK3 time integration, which was O18 for these WL results.

Unsurprisingly, solutions with high order WENO flux for the first two RK3 stages and low order WENO flux for the third stage (i.e., O17:17:3–13; Fig. 15, rows four–six, WH solutions; Table III), only shown for demonstration purposes, generally did not improve the solutions, when compared to those produced with WL solutions or those with the same order of WENO flux at each RK3 stage. The solutions were made with interpolations and pressure gradient/divergence that were either O18 for all stages (Fig. 15 for WL and WH solutions) or the lowest comparable order of accuracy of any of the three stages (not shown; errors provided in Table III). This demonstration shows that using higher order WENO fluxes, on the 1st and 2nd, than those on the 3rd stage, regardless of the order of accuracy of interpolations and pressure gradient/divergence that were considered, generally did not improve the appearance or objective measures of the WENO solutions. However, solutions for the same order-N WENO fluxes for all three RK3 stages were about the same as using order < N flux on the first two RK3 stages (WL scheme), making the use of WENO potentially much less computationally expensive. Although not tested for other schemes in this paper, these results are expected hold for any of the other schemes besides WENO fluxes considered herein.

3.4.4 | WENO approximations for scalars and constant grid flux for velocity and pressure and vice versa (Set E)

A set of experiments were made using WENO flux only for scalars and constant grid flux for velocity and pressure to determine if these are as accurate as using WENO flux for all variables. While this might not be true for non-viscous problems, especially those with shocks, it might hold for smoother diffusion-limited problems. Both Pressel et al. (2015 P15) and WPM21 commented that they did not find degradation of solutions when comparing solutions made with WENO fluxes on only scalars compared to solutions made with WENO fluxes for scalars, velocity and pressure, but neither showed these results as both studies focused on other issues. Both also noted that perhaps the reason for the minimal impact when WENO was not used for velocity fields was that velocity fields tend to be smoother than scalar fields. Simulations with the test problem herein using WENO flux for scalars only (e.g., only potential temperature, but not pressure, which is strongly coupled to velocity for sound waves; arguably, potential temperature is also strongly coupled to velocity for gravity waves through buoyancy), and comparably high order odd order upwind-biased constant grid fluxes for velocity and pressure resulted in perturbation potential temperature and KE fields (Fig. 16 rows one–three Ws Fv; zoomed as in Figs. 4–8; Table III) that were better objectively than those that used WENO flux for all variables (Table III). However, the perturbation potential temperature field was somewhat distorted, although the 0.2 K contour of the potential temperature appeared to capture the upper rotor better. The potential temperature difference fields in the upper rotor were improved, perhaps more for O13–17, when compared to results with WENO flux for all variables in Fig. 5.

Simulations with WENO for scalars and constant grid flux for velocity were repeated except using constant grid flux for scalars and WENO flux for velocity and pressure Fig. 16, rows 4–6 Fs Wv; zoomed as in Figs. 4–8), which interestingly produced solutions with somewhat worse visual appearances in terms of the shape of 0.2 K contour for potential temperature as well as in some parts of the potential temperature difference fields on the inside and around the base of the upper rotor. In contrast, as in the case for Fv Ws solutions, these Fs Wv solutions also had better objective errors for the all solutions for both perturbation potential temperature and KE fields than the solutions with WENO fluxes on all variables (Table III). The generally reduced objective errors were related to the much better reproduction of the overall amplitude of potential temperature fields compared to the reference solution, even though the L_{max} and L_{min} values for KE were not reproduced as well as in the Fv Ws experiments or experiments using WENO for all fluxes. These results were mixed in terms of supporting the use of WENO only for scalar fluxes, or only for velocity and pressure, rather than all fluxes, as objective errors were reduced for some measures, but various aspects of solution appearance were found to be worse for the colliding plumes test problem as formulated.

3.4.5 | Number of derivatives for Crowley schemes (Set F)

Smolarkiewicz (1982) successfully developed dimension-split/time-split 3D and explicit cross-derivative Crowley schemes, which use any order approximation for the advection and O2 approximations for the stabilising second derivatives. Tremback et al. (1987), similar to C68, further developed the dimension-split/time-split 3D Crowley schemes by adding stabilising derivatives up to O10 for both odd and even order O1–10 Crowley schemes (N-stabilising derivatives for an N-order scheme). Test simulations made for this paper with O3, 5, 9, 13, and 17

Crowley schemes using only the second stabilising derivative (N = 2), rather than all N stabilising higher derivatives for an N-order Crowley schemes, produced solutions for perturbation potential temperature and KE fields (Fig. 17 row one and two, C2; zoomed as in Figs. 4–8; Table III; note the traditional Crowley solutions with N-derivative for an N-order scheme are shown in Figs. 3 and 4) that were virtually indistinguishable from each other, both visually and objectively (the schemes with N-higher derivatives were nearly identical or very slightly better objectively for some of solutions), for any given scheme order. Importantly, these Crowley solutions with N = 2 were produced with lower computational costs as only two derivatives were evaluated and not N derivatives. This result can be explained in part by noting that when the Courant number value of $C = u\ \Delta t/\Delta x$ becomes increasingly small (<1), the values of C^{N} that are multiplied with each N^th^ derivative become increasingly small and less impactful (e.g., with a Courant number value used in this study of $C = 0.046875$, values for $C^{2} \sim 2.197\text{x}10^{-3}$, $C^{3} \sim 1.03\text{x}10^{-4}$, … , $C^{9} = {\sim}1.09\text{x}10^{-12}$, $C^{17} = {\sim}2.547\text{x}10^{-23}$, etc.), than if $C = 0.9$ ($C^{2} = 0.8100$, $C^{3} = 0.7290$, … , $C^{9} = {\sim}0.3874$, $C^{17} = {\sim}0.1668$, etc.). The Crowley simulations shown all use the difference-stencils (related to order of accuracy) for the higher order derivatives suggested by T87, noting that the order accuracy for the approximations for lower derivatives are generally higher order, but the highest order derivatives in T87 are not the order of the higher order derivatives (presumably this practice is not a serious issue as at least the even order derivatives are dissipative). Rather the approximations are the highest order of accuracy that will fit in the length of the stencil used to compute each specific derivative. Note that comparable order interpolations and pressure gradient/divergence were used for all Set E simulations. In summary, these results support the use of only the second stabilising derivative, as objective and visual appearances were not changed and solutions were computationally less expensive than using N derivatives for an N-order Crowley scheme.

3.4.6 | Hybrid-WENO/Crowley schemes (Set G)

Dimension-split/time-split hybrid-WENO/Crowley schemes were tested as the use of higher order derivatives sometimes can help reduce phase errors (e.g., T87; WS02). Furthermore, the WS02 forward-in-time Crowley scheme time integration procedure for mode-split systems with only one/two functions per time step for scalars, velocities, and pressure is notably less computationally intensive in terms of total FPOs for any given order of flux using the spatial differencing algorithm discussed in section 2, compared to the RK3 time integration scheme, which requires three functions per time step for scalars, velocities, and pressure, respectively. With this in mind, the use of WENO fluxes in a Crowley scheme framework might be advantageous computationally as well as numerically. Experiments were conducted with a proposed hybrid-WENO/Crowley scheme, which has interpolation for the flux obtained from the WENO scheme, and upwind-biased constant grid flux higher order derivatives. Comparable order interpolations and pressure gradient/divergence were used for all Set G simulations.

Visually accurate perturbation potential temperature and KE solutions were obtained with the Hybrid-WENO-Crowley schemes (Hy) when compared to the WENO and odd order Crowley solutions in Set A (e.g., Fig. 4). The potential temperature perturbation difference plots (Fig. 17, row four) showed patterns and regions of errors for Hybrid-WENO-Crowley that were more similar to those with the Set A, WENO solutions than the Set A, odd order Crowley solutions (Fig. 5). Objective errors, including RMS for perturbation potential temperature and KE (Table III) for the Hybrid-WENO-Crowley schemes were similar to those with the WENO schemes for these simulations. Additionally, like with the WENO scheme, the Hybrid-WENO-Crowley scheme and sine-based WENO smoothness indicators scheme, also produced improved perturbation potential temperature difference fields from the reference solution and improved RMS errors, based on the reference solution, over those made with traditional smoothness indicators by ~5% to ≥20%, especially for the O17 solutions as compared to solutions made solutions with traditional smoothness indicators. These results are important as the computational cost based on FPOs of the forward in time Hybrid-WENO-Crowley schemes, for either traditional or sine-based smoothness indicators, are markedly less than RK3 WENO solutions, especially for higher order solutions.

Using hybrid-WENO/Crowley flux for scalars and Crowley flux on velocities and pressure also performed well (Fig. 17, rows seven and eight, Hs Cv; zoomed as in Figs 4–8; Table III), while the use hybrid-WENO/Crowley on velocities and pressure only and Crowley flux on scalars produced better results for perturbation potential temperature (Fig. 17, rows nine and ten, Hv Cs; zoomed as in Figs 4–8; Table III) and KE fields (not shown), than using WENO on all variables, both with further reductions in computational cost from the cases of using WENO fluxes on all variables (the differences were again somewhat worse than for odd order Crowley). Although not shown, comparably accurate solutions, which were virtually indistinguishable, either visually (not shown) or objectively (Table III; H2S) were also possible using only the stabilising second derivative and no other higher order stabilising derivatives in these hybrid schemes. In summary, computational costs can be reduced, and objective errors notably improved using hybrid-WENO/Crowley schemes with or without the sine-based smoothness indicators, as well as with or without stabilising higher order derivative or only the stabilising second derivative. Additionally, use of hybrid WENO/Crowley fluxes on either scalars or velocities and pressure, especially for the hybrid-WENO on velocities and pressure and Crowley on scalars (Hs Cv) might help provide more accurate solutions than using WENO flux on all variables; the HsCv and HvCs solutions appeared visually better compared to the WENO solutions, but visually not as good as the Crowley solutions. This appeared to be the case for the objective errors as well.

3.4.7 | Use of lower order approximations for velocity and pressure advection and higher order for scalars and vice versa (Set H)

Finally, a set of simulations was made to determine whether higher order accuracy flux of velocities and pressure or higher order flux of scalars (potential temperature) was more important to solution accuracy, while potentially allowing for some reduced computational costs. Pressel et al. (2015) and WPM21 both stated that the velocity fields are generally smoother than the scalar fields in their atmospheric planetary boundary layer simulations (which was also seen with KE fields herein), and thus did not require velocity flux schemes to be as accurate as scalar flux schemes. The simulations shown herein include those made with O17 fluxes for scalars and O3–17 fluxes for velocities and pressure, and well as those made using O17 fluxes for velocities and pressure, and O3–17 fluxes for scalars. These were used to compare with simulations using O17 fluxes for all variables (Figs. 3 and 4–8). All Set H simulations (Fig. 18) used O(18) interpolations and pressure gradient/divergence.

The amplitudes of the perturbation potential temperature fields in the most marginally resolved features of the upper rotor for the first subset of experiments were best preserved with O17 scalar fluxes, although the shape is not as well preserved (as compared to the Set A odd order flux solutions in Fig. 4) or the reference solution) in association with less accurate velocity and pressure fluxes (Fig. 18, rows one–three, Fv s17; zoomed as in Figs 4–8; Table III). In addition, the 0.2 K perturbation potential temperature contour was not as well preserved compared to the Set A solutions or the reference solution. Conversely, the second subset of experiments produced worse amplitude preservation of the perturbation potential temperature fields with O3–13 scalar fluxes, compared to the reference solution, but about the same as in Set A, with slightly better placement and shape for the rotor associated with O17 velocities (Fig. 18, rows four–six Fs v17; zoomed as in Figs 4–8; Table III). Interestingly, the use of lower order fluxes with scalars than velocity and pressure resulted in generally better objective error measures than Set A odd order flux solutions and better 0.2 K perturbation potential temperature contour preservation in the upper rotor, especially in the narrow warm regions for most solutions, owing to lower order scalar fluxes being more dispersive, which makes the > 0.2 K regions wider, especially in finer scale regions of the upper rotor. The perturbation potential temperature difference fields also had smaller differences when using lower order (O3–5) scalar fluxes. These characteristics permit gross determinations as to which of these subsets of experiments produce the best solutions for all orders considering competing factors. The best solutions in these experiments were the Fs v17 solutions based on RMS errors for potential temperature and KE, as well as for perturbation potential temperature field differences, especially for O3–9 solutions.

4 | CONCLUSIONS

The main conclusions of this study include; The visual appearances and objective error measures for solutions produced by all schemes considered continued to improve well through flux orders of O3/4–9/10, which are the highest orders available/used in most popular research and operational 3D atmospheric science numerical models, and all the up way to O17/18. Most of the visual and objective improvements were from O3 to O5, and then from O5 to O9, and so on, although they often were not negligible from O13–17. Higher order numerical approximations also improved the accuracy of kinematic aspects of flows as seen using quantities such as KE, deformation, and vorticity. Upwind-biased, odd order, very high order flux schemes produced the least dispersion/phase errors with only minimally damped extrema at very high orders of accuracy > O13 when compared to the reference solution. Very high order even order ≥O14 schemes, which better preserve amplitude errors over one order lower odd schemes and have slightly worse phase errors than one order higher odd schemes, also performed very well. Excessive round-off error accumulation argues against using much higher than O17/18 constant grid flux and constant grid flux Crowley schemes, and especially against using higher than O13 or O17 WENO flux schemes.

The WENO flux schemes did not perform as well as the constant grid flux and constant grid flux Crowley schemes for O3–9 solutions made with resolutions coarser than 50 m, supporting the results described by Latini et al. (2006) and WPM21 that ≤ O5 WENO solutions could be excessively dissipative. Interestingly, the very high order O9–17 WENO flux scheme solutions made with a strong added mean wind were the most accurate for a given resolution, with some of the lowest overall objective errors, in this study. Importantly, the ≤O13 WENO flux solutions also tended to be more monotonic at intermediate and coarser solutions, in contrast to other schemes, even though WENO scheme solutions are technically not monotonic. While WENO schemes certainly were much more computationally expensive than most schemes considered in terms of FPOs, they were not necessarily excessively/prohibitively expensive with careful use of cache memory in making computations; the CPU time for O17 WENO was at most three to four times more than the CPU time O17 flux.

Only weak numerical spatial filters were generally needed with odd order high order constant grid flux and constant grid flux Crowley schemes in contrast to even-order schemes, which required much more filtering for low orders of accuracy as they tend to produce more dispersion and aliasing errors. Very high order constant grid flux non-WENO schemes, with had appropriate spatial filters for the diffusion-limited problem, produce solutions that were comparable or better than both lower order and higher order WENO based solutions at a fraction of the cost in terms of FPOs or CPU time, especially the forward in time WS02 Crowley based flux solutions.

The WENO flux solutions made with the exponent parameter $p = R$ in the nonlinear weights for WENO fluxes were generally less accurate based on RMS errors than those using the traditional value of $p = 2$ for the test problem. Using by $p = R$ improved maximum and minimum perturbation potential temperature overshoots and generally helped maintain more monotonic WENO flux solutions, although shear instabilities formed in these WENO solutions on the warm-cold air interface at coarser resolutions of 50 m with higher order >O13 WENO schemes, that was not present in the reference solution. Importantly, the use of recently proposed, efficient and fewer (three versus R for each stencil; for $R \geq 4$) sine-wave WENO smoothness indicators, which are exact for sine waves, along with $p = 1$, produced solutions that were in good agreement with the reference solution, and were more accurate than solutions made with traditional WENO smoothness indicators. Using less than order N WENO flux for the first two stages of the three RK3 stages of order N WENO solutions produced solutions that were as accurate as using order N WENO flux advection on all three RK3 stages, especially if the WENO flux order for the first two stages is not very small (e.g., O3) compared to the last stage (e.g., O17). Other findings include that, solutions made with odd order constant grid flux for velocities and pressure and WENO flux for scalars, were better solutions than those made with odd order constant grid flux for scalars and WENO flux for velocities and pressure, and both were more accurate, especially the former, compared to the reference solution or the use of WENO flux advection for all variables. The anti-WENO (A-WENO) O3 and O5 flux schemes proposed by WPM21 to improve the excessive smoothing of lower order WENO schemes might be considered for improvement of high order WENO schemes, but the A-WENO approach might not be necessary with higher order (≥ O7) WENO or other flux schemes. Finally, the adaptive order WENO flux schemes based on Legendre polynomials, which result in much simpler smoothness indicator approximations (Balsara et al. 2009; Balsara et al. 2016), as well as the use of hybrid-WENO flux schemes, which only use nonlinear WENO fluxes in regions of steep gradients or approximate discontinuities with efficient high order flux schemes in smoother flow regions (Hu et al. 2015) should be explored for atmospheric problems. These schemes seem very attractive as most regions in atmospheric flows are rather smooth compared to non-viscous gas dynamics flows. The proposed hybrid-WENO flux scheme is promising as WENO flux is only applied at a small number of grid points (<1%) and requires only a simple numerical test to determine whether the WENO flux should replace the more efficient high order flux.

A proposed dimension-split hybrid-WENO/Crowley advection scheme integrated in time with the WS02 two-step Crowley forward-in-time integration scheme, which allowed for fast/slow mode-split time integration, produced accurate solutions with fewer FPOs compared with either traditional or newer efficient smoothness indicators, with $p = 2$ for the traditional, or $p = 1$ for the newer smoothness indicators, respectively. This was true for hybrid-WENO/Crowley flux scheme used for all scalars, velocity and pressure, or with hybrid-WENO/Crowley flux scheme for only scalars and constant grid flux Crowley for velocity and pressure.

Crowley scheme solutions with just the stabilising O2 spatial derivative Crowley, compared to those with N higher order derivatives for an N^{th} order scheme, produce nearly identical solutions and lowers the number of FPOs. This also was true for the hybrid-WENO/Crowley flux scheme. Use of lower order odd order constant grid flux for scalars, and high order odd order constant grid flux for velocities produced better solutions in terms of the shape of the flow field features, but worse amplitudes of the potential temperature compared to the reference solution in the marginally resolved regions, than the use of the high order odd order constant grid flux for velocity and pressure, and lower order odd constant grid flux for scalars. Finally, the mode-split time integration solutions produced with constant grid flux Crowley schemes were the least computationally expensive of all schemes considered in terms of either FPOs or CPU in this study for any given order of accuracy and resolution owing largely to being amenable to being written in a condensed form. Otherwise, they would have been more computationally expensive than the constant grid flux RK3 integrations, as was found by WS02.

Future assessments of very high order numerical schemes should be made using realistic atmospheric forecast problems, especially those that require high accuracy, have complex physics, and can be integrated for relatively long periods of time relative to their spatial scales. Examples of problems that might be considered are those related to significant weather forecast for hail, winds, and tornadoes with severe storms, extreme winds and precipitation with hurricanes, heavy snow with lake effect and synoptic systems, as well as a multitude of short-term climate problems associated with excess precipitation, heat and drought, and cold waves.

In summation, upwind-biased, very high order (O9–18) flux schemes performed very well in the experiments described in this paper, especially the non-WENO flux schemes, although the high order WENO flux schemes produced very good solutions in experiments with a strong mean wind. The odd order schemes, which generally require less spatial filtering (WENO flux schemes technically required none) compared to the lower order even schemes that were considered, were only slightly more computationally expensive (two function evaluations are required for odd order schemes for each step or sub-step), when compared to even order centred flux schemes. Objective error measures for non-WENO flux schemes improved to O17/18, while those for WENO flux schemes did not improve much past O9 or O13 for intermediate resolutions of ≥ 50 m. The use of high order flux computations coupled with high order interpolation and pressure gradient/divergence numerical approximations (≥O4) are recommended to attain the best solutions, especially for physically important, marginally resolved phenomena, as was found for short-term integrations presented in this paper. The results of this study lead us to encourage the further testing of very high order ≥ O9 flux schemes in numerical weather prediction and weather research models.

ACKNOWLEDGEMENTS

The first author is grateful to Drs. G. Gerolymos, B. Fornberg, C.-W, Shu for very promptly answering many questions about high order schemes over the past several years.

AUTHOR CONTRIBUTIONS

Jerry Straka: Conceptualization; formal analysis; investigation; methodology; software; validation; visualisation; writing – original draft; writing – review and editing. Katharine Kanak: Conceptualization; formal analysis; methodology; investigation; visualisation; writing – review and editing. Paul D. Williams: Conceptualization; investigation; methodology; writing – review and editing.

DATA AVAILABILITY STATEMENT

The source codes and input files are available from authors.

FUNDING STATEMENT

There are no funding statements to report.

CONFLICT OF INTEREST DISCOSURE

There are no conflicts of interest disclosure, ethics approval statement, patient consent statement, permissions to reproduce material from other sources, or clinical trial registration, to report.

SUPPORTING INFORMATION

S1; Summary of 3D Compressible model numerical techniques and physics

S2a–d; Tables and construction instructions for all basic constant grid flux and integrated grid flux finite differences, interpolations, and filters

S3; Zoomed in figures for solutions without and with a mean wind for centred even order Crowley and Weno-Sine with resolutions of 33.33, 66.66, and 100 m.

S4; Figures for sub-domain from x = –8 to 8 km and z = 1 to 9 km for odd and even order flux, Crowley, WENO, and Weno-Sine using all orders of accuracy with and without a mean added and 100 m resolutions and with a mean for all orders of accuracy with 33.33 and 66.66 m resolution.

REFERENCES

Asselin, R. (1972) Frequency filter for time integrations. *Monthly Weather Review*, 100, 487–490, https://doi.org/10.1175/1520-0493(1972)100<0487:FFFTI>2.3.CO;2.

Baldauf, M. (2008) Stability analysis for linear discretisations of the advection equation with Runge–Kutta time integration. *Journal of Computational Physics,* 227 (2008), 6638–6659. doi:10.1016/j.jcp.2008.03.025

Baldauf, M. (2010) Linear stability analysis of Runge–Kutta-based partial time-splitting schemes for the Euler equations. *Monthly Weather Review*, 138(12), 4475–4496. https://doi.org/10.1175/2010MWR3355.1.

Balsara, D.S., Shu, C.-W. (2000) Monotonicity reserving weighted essentially non-oscillatory schemes with increasingly high order of accuracy, *Journal of Computational Physics*,160, 405–452.

Balsara, D.S., Rumpf, T., Dumbser, M., and Munz, C.-D. (2009) Efficient, high accuracy ADER-WENO schemes for hydrodynamics and divergence-free magnetohydrodynamics. *Journal of Computational Physics*, *228*(7), 2480–2516. https://doi.org/10.1016/j.jcp.2008.12.003

Balsara, D.S., S. Garain, and Shu, C.-W. (2016) An efficient class of WENO schemes with adaptive order. *Journal of Computational Physics*, 326, 780–804, https://doi.org/10.1016/j.jcp.2016.09.009.

Borges, R., Carmona, M., Costa, B. and Don, W.S. (2008): An improved weighted essentially non-oscillatory scheme for hyperbolic conservation laws. *Journal of Computational Physics*, 227, 3191–3211, https://doi.org/10.1016/j.jcp.2007.11.038.

Bott, A. (1989) A positive definite advection scheme obtained by nonlinear renormalization of the advective fluxes. *Monthly Weather Review*, 117, 1006–1015.

Bryan, G.H. (2021) The governing equations for CM1. UCAR Tech. Note, 30 pp., https://www2.mmm.ucar.edu/people/bryan/cm1/ cm1_equations.pdf.

Bryan, G.H. and Fritsch, J.M. (2002) A benchmark simulation for moist nonhydrostatic numerical models. *Monthly Weather Review*, 130(12), 2917–2928. https://doi.org/10.1175/ 1520-0493(2002)130<2917:ABSFMN>2.0.CO;2.

Castro, M., Costa, B. and W.S. Don (2011) High Order Weighted Essentially Non-Oscillatory WENO-Z schemes for Hyperbolic Conservation Laws. *Journal of Computational Physics*, 230, 1766-1792.

Clappier, A. (1998) A correction method for use in multidimensional time-splitting advection algorithms: Application to two- and three-dimensional transport. *Monthly Weather Review*, 126, 232–242.

Costa, A.A. and Sampio, A.J.C. (1997) Bott's area-preserving flux-form advection algorithm: Extension to higher orders and additional tests. *Monthly Weather Review*, 125, 1983–1989.

Crowley, W.P. (1968) Numerical advection experiments. *Monthly Weather Review.*, 96, 1–11, https://doi.org/10.1175/1520-0493(1968)096<0001:NAE>2.0.CO;2.

Durran, D.R. (2010) *Numerical Methods for Fluid Dynamics.* Second Edition. New York: Springer-Verlag.

Easter, R.C. (1993) Two modified versions of Bott's positive definite numerical advection scheme. *Monthly Weather Review*, 121, 297–304.

Fjortoft, R. (1953) On the changes in spectral distribution of kinetic energy for two dimensional nondivergent flow. *Tellus*, 5, 225–230. DOI: 10.3402/ tellusa.v5i3.8647.

Fornberg, B. (1987) The pseudospectral method: Comparisons with finite differences for the elastic wave equation. *Geophysics*, 52, 483–501.

Fornberg, B. (1988) Generation of finite difference formulas on arbitrarily spaced grids, *Mathematics of Computation*, 51, 699–706.

Gadd, A.J. (1978) A numerical advection scheme with small phase speed errors. *Quarterly Journal of the Royal Meteorological Society*, 104, 583–594.

Gerolymos, G.A., Sénéchal, D. and Vallet, I. (2009) Very-high-order WENO schemes. *Journal of Computational Physics*, 228, 8481-8524, 2009.

Grabowski, W.W. and Clark, T.L. (1991) Cloud–environment interface instability: Rising thermal calculations in two spatial dimensions. *Journal of the Atmospheric Sciences*, 48(4), 527–546. https://doi.org/10.1175/1520-0469(1991)048<0527:CIIRTC>2.0. CO;2.

Haltiner, G.J and Williams,R.T. (1980) Numerical Prediction and Dynamical Meteorology. John Wiley and Sons, Inc. 477 pp. ISBN 0-471-05971-4.

Hu. X, Wang B. and Adams N.A. (2015) An efficient low-dissipation hybrid weighted essentially non-oscillatory scheme. *Journal of Computational Physics*, 301, 415–424.

Hundsdorfer, W. B., Koren, B., van Loon, M. and Verwer, J. G. (1995) A positive finite difference advection scheme. *Journal of Computational Physics*, 117, 35–46.

Jiang, G.-S. and Shu, C.-W. (1996) Efficient implementation of Weighted ENO schemes. *Journal of Computational Physics*, 126, 202–228.

Latini, M., Schilling, O. and Don, W. (2006) Effects of WENO flux reconstruction order and spatial resolution on reshocked two-dimensional Richtmyer-Meshkov instability. Lawrence Livermore National Laboratory, UCRL-TR–220015.

Leonard, B. P. (1991) The ULTIMATE conservative difference scheme applied to unsteady one-dimensional advection. *Computational Methods in Applied Mechanical Engineering*, 88, 17–74.

Lian, Y, Richardson, M.I., Newman, C.E., Lee, C., Toigo, A., Guzewich, S. and Yelle, R.V. (2022) Dynamical core damping of thermal tides in the Martian atmosphere. *Journal of the Atmospheric Sciences,* early release.

Lunet, T., Christine L., Auguste, **F.,** Visentin, F., Masson, V. **and** Escobar, J. (2017) Combination of WENO and explicit Runge–Kutta Methods for wind transport in the Meso-NH Model**.** *Monthly Weather Review* 145, 3817-3838. doi: 10.1175/MWR-D_16_0343.1.

Morrison, H. and Bryan, G.H. (2012) Sensitivity of a simulated squall line to horizontal resolution and parameterization of microphysics. *Monthly Weather Review* 140, 202–225. doi: 10.1175/MWR-D–11-00046.1.

Norman, M.R. (2021) A high-order WENO- limited finite- volume algorithm for atmospheric flow using the ADER-differential transform time discretization. *Quarterly Journal of the Royal Meteorological Society*, 147, 1661–1690, https://doi.org/10.1002/qj.3989

Park, S.-H. and Lee, T.-Y. (2009) High-order time-integration schemes with explicit time-splitting methods. *Monthly Weather Review* 137, 4047–4060. doi: 10.1175/2009MWR2885–1.

Pressel, K.G., Kaul, C.M., Schneider, T., Tan, Z. and Mishra, S. (2015) Large-eddy simulation in an anelastic framework with closed water and entropy balances. *Journal of Advances in Modeling Earth Systems*, 7, 1425–1456, doi:10.1002/ 2015MS000496.

Purser, R.J. (1987) The filtering of meteorological fields. *Journal of Applied Meteorology and Climatology*, 26(12), 1764–1769. https://doi.org/10.1175/1520-0450(1987)026<1764:TFOMF>2.0. CO;2.

Purser, R.J. and Leslie, L.M. (1988) A semi-implicit, semi-Lagrangian finite difference scheme using high-order spatial differences on a nonstaggered grid. *Monthly Weather Review*, 116, 2069–2080.

Purser, R.J. (2007) Accuracy considerations of time-splitting methods for models using two-time-levels schemes. *Monthly Weather Review* 135, 3, 1158–1164. https://doi.org/10.1175/MWR3339.1.

Qiu, J. and Shu C.-W. (2002) On the Construction, Comparison, and Local Characteristic Decomposition for High-Order Central WENO Schemes. *Journal of Computational Physics*, 183, 187–209. https://doi.org/10.1006/jcph.2002.7191

Schlesinger, R.E. (1984) Mature thunderstorm cloud top structure and dynamics: A three-dimensional numerical simulation study. *Journal of the Atmospheric Sciences*, 41, 1551–1570.

Schlesinger, R.E. (1985) Effects of upstream-biased third-order space correction terms on multidimensional Crowley advection schemes. *Monthly Weather Review*, 113(7), 1109–1130. https://doi.org/10.1175/1520-0493(1985)113<1109:EOUBTO> 2.0.CO;2.

Shapiro, R. (1970) Smoothing, filtering, and boundary effects. *Reviews of Geophysics*, 8(2), 359–387. https://doi.org/10.1029/ RG008i002p00359.

Shi, J, Zhang, Y.-T., and Shu, C.-W. (2003) High order WENO schemes for complicated flow structures. *Journal of Computational Physics*, 186, 690-691.

Shu, C.-W. (1988) Total-variation-diminishing time discretizations. *SIAM Journal on Scientific Computing*, 9, 12, http://dx.doi.org.ezproxy.lib.ou.edu/10.1137/0909073.

Shu, C.-W. (1997) Essentially non-oscillatory and weighted essentially non-oscillatory schemes for hyperbolic conservation laws. NASA/CR-97–206253 ICASE Report No. 97-65. 79 pp.

Shu, C.-W. (2003) High-order finite difference and finite volume WENO schemes and discontinuous Galerkin methods for CFD. *International Journal of Computational Fluid Dynamics,* 17, 107–118, https://doi.org/ 10.1080/1061856031000104851.

Shu, C.-W. and Osher, S. (1988) Efficient implementation of essentially non-oscillatory shock-capturing schemes. *Journal of Computational Physics*, 77, 439–471, https://doi.org/10.1016/0021-9991(88)90177-5.

Shuman, F.G. (1957) Numerical methods in weather prediction. II: Smoothing and filtering. *Monthly Weather Review*, 85(11), 357–361. https://doi.org/10.1175/1520-0493(1957)085<0357:NMIWPI>2.0.CO;2.

Skamarock, W.C. and Klemp, J.B. (1992) The stability of time-split numerical methods for the hydrostatic and the nonhydrostatic elastic equations. *Monthly Weather Review*, 120(9), 2109–2127. https://doi.org/10.1175/1520-0493(1992)120<2109:TSOTSN> 2.0.CO;2.

Smolarkiewicz, P.K. (1982) The multi-dimensional Crowley advection scheme. *Monthly Weather Review*, 110(12), 1968–1983. https://doi.org/10.1175/1520-0493(1982)110<1968:TMDCAS> 2.0.CO;2.

Smolarkiewicz, P.K. (1985) On the accuracy of the Crowley advection scheme. *Monthly Weather Review*, 113(8), 1425–1429. http://dx.doi.org/10.1175/1520-0493(1985)113<1425:OTAOTC>2.0.CO;2.

Soong, S.-T. and. Ogura, Y. (1973) A comparison between axisymmetric and slab-symmetric cumulus models. *Journal of the Atmospheric Sciences*, 30, 879-893.

Straka, J.M. and Anderson, J.R. (1993) Extension and application of a local, minimum aliasing method to multidimensional problems in limited-area domains. *Monthly Weather Review*, 121, 2903–2918, https://doi.org/10.1175/1520-0493(1993)121<2903:EAAOAL>2.0.CO;2. rso

Straka, J.M., Wilhelmson, R.B., Wicker, L.J., Anderson, J.R. and Droegemeier, K.K. (1993) Numerical solutions of a non-linear density current: A benchmark solution and comparisons. *International Journal for Numerical Methods in Fluids*, 17(1), 1–22. https://doi.org/10.1002/fld.1650170103.

Straka, J.M., Williams, P.D. and Kanak, K.M. (2023) Nonlinear diffusion-limited 2D colliding plume simulations with very high order O3–17 flux, O2–18 interpolation, O2–18 pressure gradient/divergence, and O2–10 turbulent flux numerical approximations. Revision submitted to *Quarterly Journal of the Royal Meteorological Society*.

Tan, K.-A., Morison, R. and Leslie, L.M. (2005). A comparison of high-order explicit and non-oscillatory finite difference advection schemes for climate and weather models. *Meteorology and Atmospheric Physics*, 89, 251–267. https://doi.org/10.1007/s00703-005-0132-0

Tremback, C.J., Powell, J., Cotton, W.R. and Pielke, R.A. (1987) The forward–in-time upstream advection scheme: Extension to higher orders. *Monthly Weather Review*, 115(2), 540–555. https://doi.org/10.1175/1520-0493(1987)115<0540:TFTUAS> 2.0.CO;2.

Walko, R.L. and Avissar, R. (2008) The ocean–land–atmosphere model (OLAM). Part II: Formulation and tests of the nonhydrostatic dynamic core. *Monthly Weather Review*, 136(11), 4045–4062. https://doi.org/10.1175/2008MWR2523.1.

Wang, A., Pan, Y. and Markowski, P.M. (2021) The influence of WENO schemes on large-eddy simulations of a neutral atmospheric boundary layer. *Journal of the Atmospheric Sciences*, 78, (12), 3613-3628. DOI: https://doi.org/10.1175/JAS-D–21-0033.1

Wicker, L.J. and Skamarock, W.C. (2002) Time-splitting methods for elastic models using forward time schemes. *Monthly Weather Review*, 130(8), 2088–2097. https://doi.org/10.1175/ 1520-0493(2002)130<2088:TSMFEM>2.0.CO;2.

Williams, P.D. (2009) A proposed modification to the Robert–Asselin time filter. *Monthly Weather Review,* 137, 2538–2546, https://doi.org/10.1175/2009MWR2724.1.

Williams, P.D. (2011) The RAW Filter: An improvement to the Robert–Asselin filter in semi-implicit integrations. *Monthly Weather Review*, 139, 1996–2007, https://doi.org/10.1175/2010MWR3601.1.

Williams, P.D. (2013) Achieving seventh-order amplitude accuracy in leapfrog integrations. *Monthly Weather Review*, 141(9), 3037–3051. https://doi.org/10.1175/MWR-D–12-00303.1.

Williams, P.D., Straka, J.M. and Kanak, K.M. (2022) The performance of filtered leapfrog schemes in benchmark simulations. *Quarterly Journal of the Royal Meteorological Society*, 148, 784-808. doi: https://doi.org/10.1002/qj.4231

Williamson, J.H. 1980: Low storage Runge-Kutta schemes**.** *Journal of Computational Physics*, **35,** 48–56.

Wu, C., Wu, L. and Zhang, S. (2020) A smoothness indicator constant for sine functions. *Journal of Computational Physics*, 419, 109661. https://doi.org/10.1016/j.jcp.2020.109661s

Wu, C., Wu, L., Li, H. and Zhang, S. (2021) Very high order WENO schemes using efficient smoothness indicators. *Journal of Computational Physics*, 432, 110158. https://doi.org/10.1016/j.jcp.2021.110158

Zhang, Y.T., Shi, J., Shu, C.W. and Zhou, Y. (2003) Numerical viscosity and resolution of high-order weighted essentially nonoscillatory schemes for compressible flows with high Reynolds numbers. *Physical Review E*, 68, 046709. DOI: 10.1103/PhysRevE.68.046709.

Title: **Comparison of very high order (O3–18) flux and Crowley flux, and (O3–17) WENO flux schemes with a 2D nonlinear test problem**

Authors: Jerry M. Straka*, Katharine M. Kanak, Paul D. Williams

Corresponding Author:
Jerry M. Straka*
5113 Ladbrook Street
Norman, Oklahoma, USA 73072
Phone; 405-664–3907
email: jerrystraka@gmail.com
Prof. Emeritus School of Meteorology
University of Oklahoma, Norman, Oklahoma 73072

Summary of key findings: Very high order odd and even order flux and Crowley flux, and odd order WENO flux were evaluated for orders of accuracy that ranged from order 3–20 and resolutions that varied by a factor of six, using simulations of nonlinear 2D colliding plumes. At intermediate resolutions, which only marginally resolved important flow structures, the best solutions were obtained with ≥O13/14 flux, Crowley flux, and O13–17 WENO flux. For a given resolution, the Crowley solutions were least computationally intensive.

Summary figure:

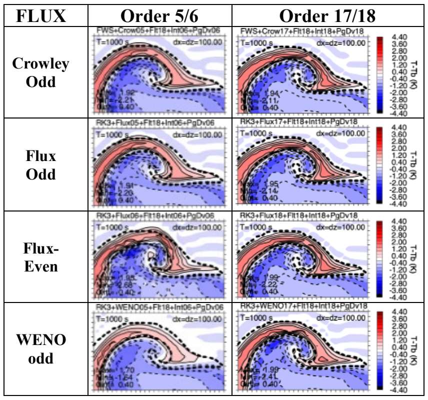

Caption: Part of nonlinear 2D colliding plumes solutions the stronger rotors that forms, using odd order 5 and 17 Crowley, odd/even order 5/6 and 17/18 order Flux, and odd order 5 and 17 WENO flux.

TABLE OF CONTENTS

AUTHOR CONTRIBUTIONS

DATA AVAILABILITY STATEMENT

SUPPORTING INFORMATION

REFERENCES

TABLE I Domain and timestep parameters. Nx (Nz) is equal to the number of scalar grid points in *x*- (*z*-) directions for a staggered grid. The total number of grid points = Nx • Nz, and Nt is the number of time steps for 1000 s of integration. The *x*-direction velocity (*u*) has one extra point in the *x*-direction and the *z*-direction velocity (w) has one extra point in the *z*-direction for the staggered C-grid. The time steps for each resolution are found using $\Delta t = C \bullet \Delta x / V_{max}(s)$, where Courant number C = 0.046875, values of Δ*x* are grid resolutions, and approximate maximum velocity $V_{max} = 15 \text{ m s}^{-1}$.

Δ*x* (m)	Δ*z* (m)	Lx (m)	Lz (m)	Nx	Nz	Nx • Nz	Nt	Δ*t* (s)
166.66…	166.66…	20000	10000	121	61	7381	1920	0.520833…
133.33…	133.33…	20000	10000	151	76	11476	2400	0.4166…
100.00	100.00	20000	10000	201	101	20301	3200	0.3125
66.66…	66.66…	20000	10000	301	151	45451	4800	0.20833...
50.00	50.00	20000	10000	401	201	80601	6400	0.15625
33.33…	33.33…	20000	10000	601	301	180901	9600	0.104166…
25	25	20000	10000	801	401	321201	12800	0.078125

Table II Simulation sets, resolutions, and orders of accuracy. Abbreviations are: **Co** = odd order upwind-biased constant grid flux Crowley; **Ce** = even order constant grid flux Crowley; **Fo** = upwind-biased odd order constant grid flux; **Fe** = even order constant grid flux; **W** = WENO flux; **WS** = W with sine-based smoothness indicators; **WR** = W with smoothness indicator power given by p = R, where O = 2R–1; **WL** c:c:17 = O3, 5, 9, 13,17 W for stages one and two of RK3, and O17 W for stage three of RK3; **WH** = (17:17:c) = O17 W for stages one and two of RK3, and O3, 5, 9, 13, 17 W for stage three of RK3; **WH PIc** = (17:17:c) = O17 W for stages one and two of RK3, and O3, 5, 9, 13, 17 W for stage three of RK3 with comparable order interpolations and pressure gradient/divergence; **Ws Fv** = W for scalars and Fo for velocities/pressure; **Fs Wv** = Fo for scalars and W for velocities/pressure; **C2** = O3, 5, 9, 13, 17 Co with N = 2 derivatives in place of N = Nth order Crowley scheme; **Hy** = hybrid WENO/Crowley flux; **HS** = hybrid WENO/Crowley flux with sine-based smoothness indicators (p = 1); **Hs Cv** = hybrid W for scalars and Co for velocities/pressure; **Hv Cs** = hybrid W for velocities/pressure and Co for scalars; **Fv s17** = lower order Fo (O3, 5, 9, 13, 17) for velocities/pressure and O17 Fo for scalars; and **Fs v17** = lower order Fo (O3, 5, 9, 13 17) for scalars and O17 for velocities/pressure. Other abbreviations are U_t = added mean wind; scl = scalar, vp = velocity/pressure; SF = spatial filter; PD = pressure gradient and divergence; and I=interpolations; Oc = comparable order (same order as even order flux and one order higher for odd order flux).

Sets	Schemes	Experiment description	$\Delta x = \Delta z$ (m)	Order Flux	Order of SF / PD / I
A	**Co, Ce, Fo, Fe, W**	Co, Ce, Fo, Fe, W with $U_t = 0$ m s^{-1}	25, 33.33, 50, 66.66, 100, 133.33, 166.66	O3,5,9,13,17 O4,6,10,14,18	O18 / Oc / Oc
B	**Co, Ce, Fo, Fe, W**	Co, Fo, Fe, W with $U_t = -20$ m s^{-1}	25, 33.33, 50, 66.66, 100, 133.33, 166.66	O3,5,9,13,17 O4,6,10,14,18	O18 / Oc / Oc
C	**WS** **WR**	WS (w-sine, p = 1) WR (p = R)	100	O3,5,9,13,17	O18 / Oc / Oc
D	**WL c:c:17** **WH17:17:c** **WH PIc**	WL (WH) has low (high) order WENO for first two stages of RK3 time integrations	100	O3,5,9,13,17	O18 / O18 / O18
E	**Ws Fv** **Wv Fs**	Ws Fv is W for scl, Fo for vp Wv Fs is W for vp, Fo for scl	100	O3,5,9,13,17	O18 / O18 / O18
F	**C2**	Co with N=2 derivatives	100	O3,5,9,13,17	O18 / Oc / Oc
G	**Hy, HS** **Hs Cv** **Hv Cs**	Hy W/Co, Hy W-sine (p=1)/Co Hy scl and Co vp Hy vp and Co scl	100	O3,5,9,13,17	O18 / Oc / Oc
H	**Fv s17** **Fs v17**	Fo vp, O17 scl Fo sc, O17 vp	100	O3,5,9,13,17	O18 / O18 / O18

TABLE III RMS errors with four significant digits for potential temperature / kinetic energy per unit volume in simulation Sets A–H for $\Delta x = \Delta z = 100$ m simulations with errors computed using the O 17, 25 m reference simulation. The top row indicates odd/even order solutions from O3/4–17/18. Abbreviations include: **Co** = odd order upwind-biased constant grid flux Crowley; **Ce** = even order constant grid flux Crowley; **Fo** = upwind-biased odd order constant grid flux; **Fe** = even order constant grid flux; **W** = WENO flux; **WS** = W with sine-based smoothness indicators; **WR** = W with smoothness indicator power given by $p = R$, where $O = 2R–1$; **WL** c:c:17 = O3, 5, 9, or 13 W for stages one and two of RK3, and O17 W for stage three of RK3; **WH** = (17:17:c) = O17 W for stages one and two of RK3, and O3, 5, 9, or 13 W for stage three of RK3; **WH PIc** = (17:17:c) = O17 W for stages one and two of RK3, and O3, 5, 9, or 13 W for stage three of RK3 with comparable order interpolations and pressure gradient/divergence; **Ws Fv** = W for scalars and Fo for velocities/pressure; **Fs Wv** = Fo for scalars and W for velocities/pressure; **Co2** = O3, 5, 9, 13, or 17 Co with N = 2 derivatives in place of N = order of Crowley scheme; **Hy** = hybrid WENO/Crowley flux; **HS** = hybrid WENO/Crowley flux with sine-based smoothness indicators ($p = 1$); **H2S** = hybrid W for scalars and Co with N = 2 derivatives in place of N = order of Crowley scheme; **Hs Cv** = hybrid W for scalars and Co for velocities/pressure; **Hv Cs** = hybrid W for velocities/pressure and Co for scalars; **Fv s17** = lower order Fo (O3, 5, 9, or 13) for velocities/pressure and O17 Fo for scalars; and **Fs v17** = lower order Fo (O3, 5, 9, or 13) for scalars and O17 Fo for velocities/pressure. NA = not available. The bold numbers are the four lowest RMS errors for each set.

	Schemes	O3/4	O5/6	O9/10	O13/14	O17/18
A	**Co**	0.1399 / 1.768	0.1064 / 1.302	0.08396 / 1.088	0.07378 / 1.024	**0.07001 / 1.012**
	Ce	0.1980 / 2.472	0.1352 / 1.439	0.08735 / 1.075	0.07347 / 1.001	**0.06984 / 0.09552**
	Fo	0.1420 / 1.811	0.1069 / 1.302	0.07862 / 1.035	0.07149 / 1.002	**0.07037 / 1.050**
	Fe	0.2106 / 2.623	0.1413 / 1.497	0.08670 / 1.058	0.07183 / 0.9846	**0.07038 / 1.002**
	W	0.1909 / 2.429	0.1200 / 1.527	0.08947 / 1.163	0.08698 / 1.130	0.1023 / 1.154
B	**Co**	0.2123 / 3.018	0.1983 / 2.587	0.2054 / 2.821	0.2084 / 2.854	0.2093 / 2.875
	Ce	0.2467 / 3.465	0.2225 / 3.045	0.2093 / 2.883	0.2083 / 2.873	0.2099 / 2.897
	Fo	0.2026 / 2.893	0.1811 / 2.698	0.1801 / 2.659	0.1803 / 2.680	**0.1798 / 2.692**
	Fe	0.2513 / 3.910	0.2289 / 3.323	0.1993 / 2.972	0.1850 / 2.758	0.1842 / 2.751
	W	0.2499 / 3.992	0.1838 / 2.700	**0.1715 / 2.587**	**0.1739 / 2.622**	**0.1742 / 2.569**
C	**WR**	0.1909 / 2.429	0.1299 / 1.642	0.1095 / 1.380	0.1029 / 1.283	**0.09734 / 1.271**
	WS	NA	NA	**0.08055 / 1.137**	**0.08110 / 1.136**	**0.07697 / 1.077**
D	**WL c:c:17**	0.1007 / 1.136	0.1013 / 1.144	0.1015 / 1.148	0.1023 / 1.155	0.1023 / 1.154
	WH17:17:c	0.1649 / 2.436	0.1217 / 1.548	**0.09241 / 1.180**	**0.08866 / 1.136**	0.1023 / 1.154
	WH PIc	0.1908 / 2.427	0.1199 / 1.527	**0.08956 / 1.162**	**0.08707 / 1.131**	0.1023 / 1.154
E	**Fs Wv**	0.1648 / 2.104	0.1102 / 1.424	0.08707 / 1.151	**0.08363 / 1.098**	**0.08235 / 1.071**
	Fv Ws	0.1711 / 2.072	0.1121 / 1.283	**0.08226 / 1.035**	**0.07877 / 1.033**	0.09121 / 1.061
F	**Co2**	0.1399 / 1.768	0.1064 / 1.302	0.08401 / 1.088	0.07380 / 1.024	0.07001 / 1.012
G	**Hy**	0.1918 / 2.421	0.1204 / 1.525	0.09058 / 1.171	0.08820 / 1.135	0.1002 / 1.147
	HS	NA	NA	0.08247 / 1.135	0.08315 / 1.171	**0.07554 / 1.060**
	H2S	NA	NA	0.08247 / 1.135	0.08315 / 1.171	**0.07554 / 1.060**
	Hs Cv	0.1715 / 2.066	0.1123 / 1.293	**0.08236 / 1.065**	**0.07909 / 1.053**	0.08803 / 1.069
	Hv Cs	0.1640 / 2.078	0.1117 / 1.434	0.09012 / 1.180	0.08500 / 1.107	0.08374 / 1.064
H	**Fv s17**	0.1452 / 1.820	0.1109 / 1.318	0.08671 / 1.140	0.08113 / 1.144	**0.07037 / 1.050**
	Fs v17	0.1143 / 1.372	0.08570 / 1.060	**0.07148 / 0.9861**	**0.07029 / 1.006**	**0.07037 / 1.050**

TABLE IV CPU times (s) for odd and even order Crowley flux (**schemes Co** and **Ce**), odd and even order flux (schemes **Fo** and **Fe**), and odd order WENO flux (scheme **W**), using 100, 66.66, and 33.33 m and time *t* = 31.25 s (100, 200, and 300 steps), along with RMS errors for perturbation potential temperature (top number in each cell) and kinetic energy per unit volume (bottom number in each cell). Top values for each scheme and order are CPU times for only the flux stencil + pressure gradient stencil + divergence stencil + interpolation stencil calculations and next to the CPU time in bold is the ratio to the lowest order scheme (O3/4) in the row. The second value for each scheme and order are CPU time for only total advection + total small step + total buoyancy and next to the CPU time in bold is the ratio to the lowest order scheme (O3/4) in the row. The CPU times for the O18 filter (SGS turbulence) are ~0.1, 0.3, and 0.9 s (7, 14, and 38 s) for Crowley simulations, and 0.2, 0.4, 1.4 s (11, 21, 57 s) for RK3 solutions (both odd and even flux and odd WENO) using 100, 66.66, and 33.33 m, respectively. Note with a constant Courant number, 66.66 and 33.33 m resolution solutions take 1.5 and 3 times more time steps than the 100 m resolution solutions. (The flux stencil CPU times were not collected for the WENO solutions and labeled NA or not available, however the total advection time was so row two in each cell was available).

TABLE IV.A CPU times and RMS errors using a resolution of 100 m

100 m scheme	**O3/4 CPU**	**O3/4 RMS**	**O5/6 CPU**	**O5/6 RMS**	**O9/10 CPU**	**O9/10 RMS**	**O13/14 CPU**	**O13/14 RMS**	**O17/18 CPU**	**O17/18 RMS**
Co	1.81 / **1.00** 20.8 / **1.00**	0.1399 1.768	2.48 / **1.37** 21.2 / **1.02**	0.1064 1.302	4.53 / **2.50** 23.9 / **1.15**	0.08396 1.088	5.56 / **3.07** 25.2 / **1.21**	0.07378 1.024	6.31 / **3.49** 25.3 / **1.22**	0.07001 1.012
Ce	1.59 / **1.00** 18.4 / **1.00**	0.1980 2.472	2.37 / **1.49** 19.6 / **1.07**	0.1352 1.439	3.36 / **2.11** 21.0 / **1.14**	0.08735 1.075	4.38 / **2.75** 22.0 / **1.20**	0.07347 1.001	5.21 / **3.28** 22.0 / **1.20**	0.06984 0.9952
Fo	1.38 / **1.00** 27.0 / **1.00**	0.142 1.811	2.22 / **1.61** 28.5 / **1.06**	0.1069 1.302	3.12 / **2.26** 30.1 / **1.11**	0.07862 1.035	3.91 / **2.83** 30.5 / **1.13**	0.07149 1.002	4.96 / **3.59** 31.9 / **1.18**	0.07037 1.017
Fe	1.28 / **1.00** 19.0 / **1.00**	0.2106 2.623	2.02 / **1.57** 20.1 / **1.06**	0.1413 1.497	2.91 / **2.23** 20.6 / **1.08**	0.08670 1.058	3.90 / **3.04** 21.9 / **1.15**	0.07183 0.9846	4.87 / **3.80** 23.3 / **1.23**	0.07377 1.003
W	NA 44.8 / **1.00**	0.1909 2.429	NA 52.0 / **1.16**	0.1200 1.527	NA 56.4 / **1.26**	0.08975 1.163	NA 61.3 / **1.37**	0.08698 1.130	NA 67.4 / **1.50**	0.1023 1.154

TABLE IV.B CPU times and RMS errors as in TABLE IV.A, except using a resolution of 66.66 m

66 m scheme	**O3/4 CPU**	**O3/4 RMS**	**O5/6 CPU**	**O5/6 RMS**	**O9/10 CPU**	**O9/10 RMS**	**O13/14 CPU**	**O13/14 RMS**	**O17/18 CPU**	**O17/18 RMS**
Co	5.79 / **1.00** 56.3 / **1.00**	0.08712 1.027	8.13 / **1.34** 58.8 / **1.04**	0.05272 0.7156	14.7 / **2.38** 65.5 / **1.16**	0.04601 0.6818	17.7 / **2.80** 70.5 / **1.25**	0.04318 0.6605	21.0 / **3.62** 76.1 / **1.35**	0.03923 0.6025
Ce	4.94 / **1.00** 50.4 / **1.00**	0.09374 1.0271	7.29 / **1.48** 53.8 / **1.07**	0.06561 0.8279	11.2 / **2.27** 58.5 / **1.16**	0.04721 0.6800	14.2 / **2.87** 62.3 / **1.24**	0.04245 0.6386	17.0 / **3.44** 63.9 / **1.27**	0.03915 0.5873
Fo	3.93 / **1.00** 76.3 / **1.00**	0.08788 1.032	6.68 / **1.70** 80.8 / **1.06**	0.04953 0.6744	9.67 / **2.46** 88.3 / **1.16**	0.0403 0.6150	12.5 / **3.18** 90.1 / **1.18**	0.03884 0.6001	15.8 / **4.02** 95.4 / **1.25**	0.03981 0.5705
Fe	3.84 / **1.00** 49.5 / **1.00**	0.09472 1.063	5.83 / **1.82** 53.5 / **1.08**	0.06503 0.7991	9.53 / **2.48** 57.1 / **1.15**	0.04409 0.6364	12.5 / **3.26** 61.3 / **1.24**	0.03973 0.5988	15.4 / **4.01** 64.7 / **1.31**	0.03871 0.5674
W	NA 133.2 / **1.00**	0.1383 1.618	NA 172.5 / **1.30**	0.06915 0.9237	NA 183.2 / **1.38**	0.04632 0.6768	NA 200.7 / **1.51**	0.04628 0.6492	NA 225.3 / **1.69**	0.04512 0.6126

TABLE IV.C CPU times and RMS errors as in TABLE IV.A, except using a resolution of 33.33 m.

33 m scheme	**O3/4 CPU**	**O3/4 RMS**	**O5/6 CPU**	**O5/6 RMS**	**O9/10 CPU**	**O9/10 RMS**	**O13/14 CPU**	**O13/14 RMS**	**O17/18 CPU**	**O17/18 RMS**
Co	45.0 / **1.00** 364.8 / **1.00**	0.02868 0.3777	62.4 / **1.39** 381.3 / **1.05**	0.02401 0.3125	108.3 / **2.41** 430.5 / **1.18**	0.02849 0.3503	131.1 / **2.91** 461.4 / **1.26**	0.02369 0.2962	150.9 / **3.35** 483.6 / **1.33**	0.0115 0.1639
Ce	36.0 / **1.00** 316.8 / **1.00**	0.02577 0.3580	55.0 / **1.53** 339.0 / **1.07**	0.02441 0.3146	81.0 / **2.25** 365.4 / **1.15**	0.02432 0.3077	104.7 / **2.76** 391.8 / **1.24**	0.01839 0.2365	124.8 / **3.47** 414.3 / **1.31**	0.00885 0.1355
Fo	28.0 / **1.00** 459.6 / **1.00**	0.02581 0.3421	48.1 / **1.72** 493.2 / **1.07**	0.02026 0.2674	69.9 / **2.50** 528.9 / **1.15**	0.02035 0.2610	92.1 / **3.30** 564.9 / **1.23**	0.01576 0.2100	117.0 / **4.19** 604.5 / **1.32**	0.00755 0.1163
Fe	28.1 / **1.00** 311.4 / **1.00**	0.02233 0.3158	47.7/ **1.70** 343.5 / **1.10**	0.02070 0.2702	69.0 / **2.46** 357.6 / **1.15**	0.02064 0.2634	92.1 / **3.23** 380.7 / **1.22**	0.01589 0.2110	114.9 / **4.09** 404.4 / **1.30**	0.00758 0.1165
W	NA 1088.4 / **1.00**	0.05527 0.6198	NA 1548.0 / **1.42**	0.01941 0.2487	NA 1692.7 / **1.56**	0.02072 0.2646	NA 1860.3 / **1.71**	0.01526 0.2116	NA 2085.9 / **1.92**	0.00768 0.1234

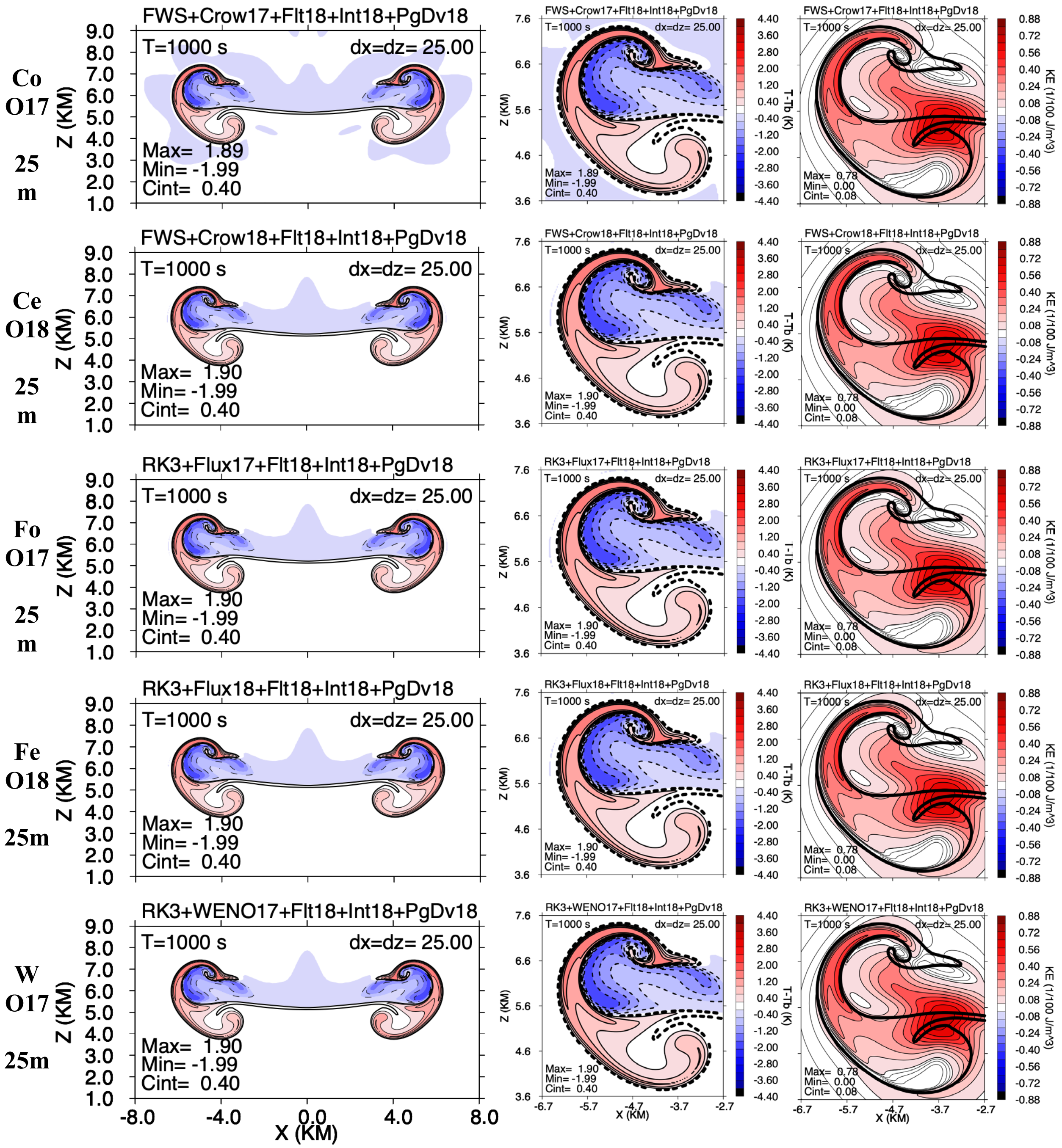

FIGURE 1 Set A perturbation potential temperature ($T - T_b$; K) fields at $t = 1000$ s made with grid resolution $\Delta x = \Delta z = 25$ m with odd/even order O17/18 upwind-biased/centred constant grid flux Crowley (Co = odd; Ce = even), upwind-biased/centred constant grid flux (Fo = odd; Fe = even), and WENO (W) flux schemes, with O18 interpolations and pressure gradient/divergence, O18 spatial filter, same Courant number C, and constant eddy mixing coefficient of $K_m = 10$ m^2 s^{-1} shown in left and centre columns. Kinetic Energy per unit volume (KE; 1/100 J m^{-3}) fields shown in the right column. Maximum (Max) and minimum (Min) values and contour interval (Cint) values are on each plot. The bold solid line is the 0.2 K perturbation potential temperature contour of the simulation in the plot. The bold dashed line in the centre column plots is the 0.2 K perturbation potential temperature contour of the upwind-biased constant grid flux O17, 25 m reference solution. Only a sub-domain (most of the whole domain) from $x = -8$ to 8 km and $z = 1$ to 9 km in the left column, $x = -6.7$ to -2.7 km and $z = 3.6$ to 7.6 km (left rotor) in the centre column and right column are shown.

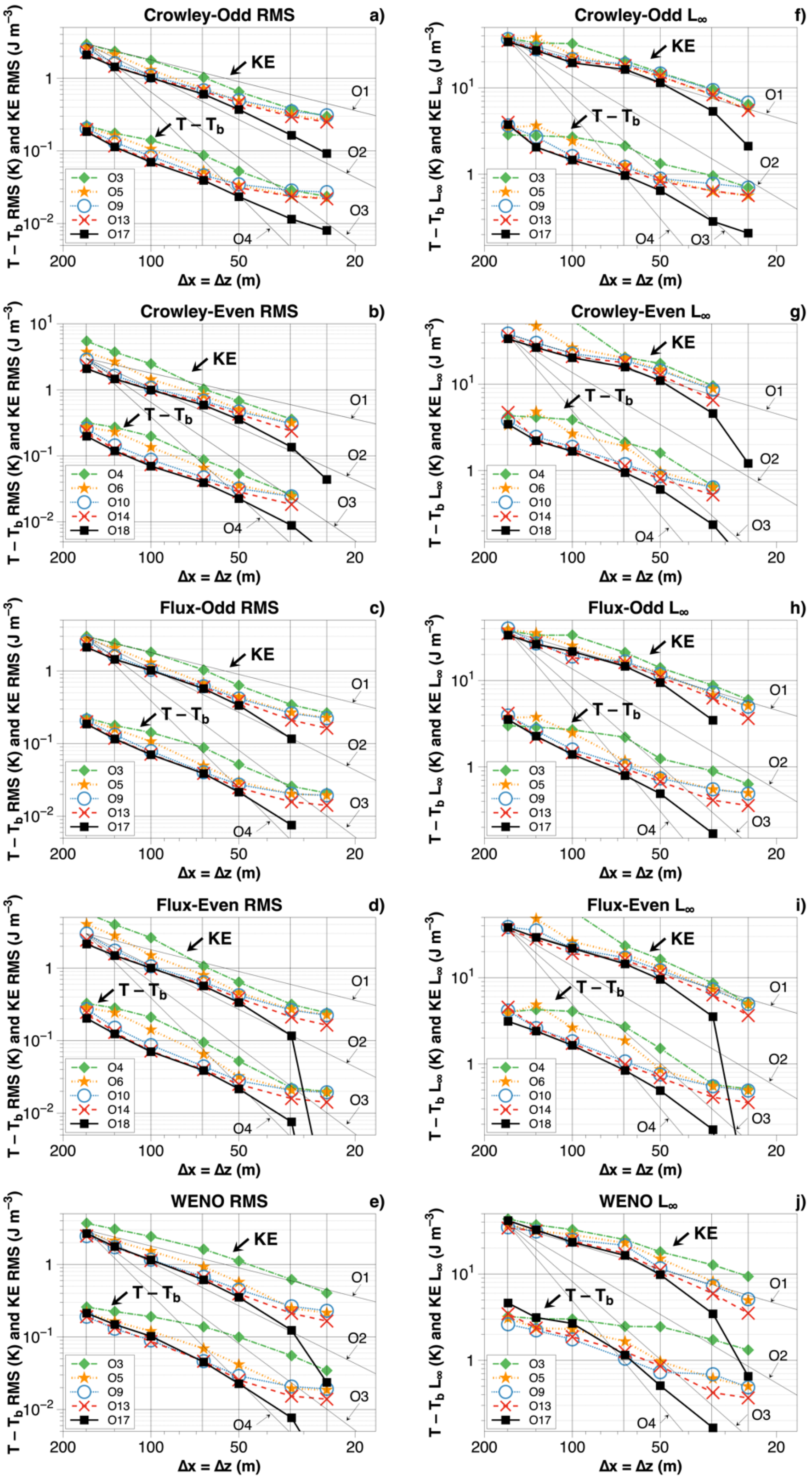

FIGURE 2 Set A objective error measures. Perturbation potential temperature ($T - T_b$; K; lower curve cluster in each panel) and Kinetic Energy (KE; J m^{-3}; upper curve cluster in each panel) Root Mean Square errors (RMS; left) and L$_\infty$ error norms (right) calculated against the flux O17, 25 m reference solution for the odd O3, 5, 9, 13, and 17) and even order (O4, 8, 10,14, and 18) upwind-biased constant grid flux Crowley schemes, odd order and even order constant grid flux, and odd order (O3, 5, 9, 13, and 17) WENO flux schemes, with comparable order interpolations and pressure gradient/divergence, O18 spatial filter,

same Courant number C, and constant eddy mixing coefficient of $K_m = 10$ m^2 s^{-1} versus resolution $\Delta x = \Delta z$ (m).

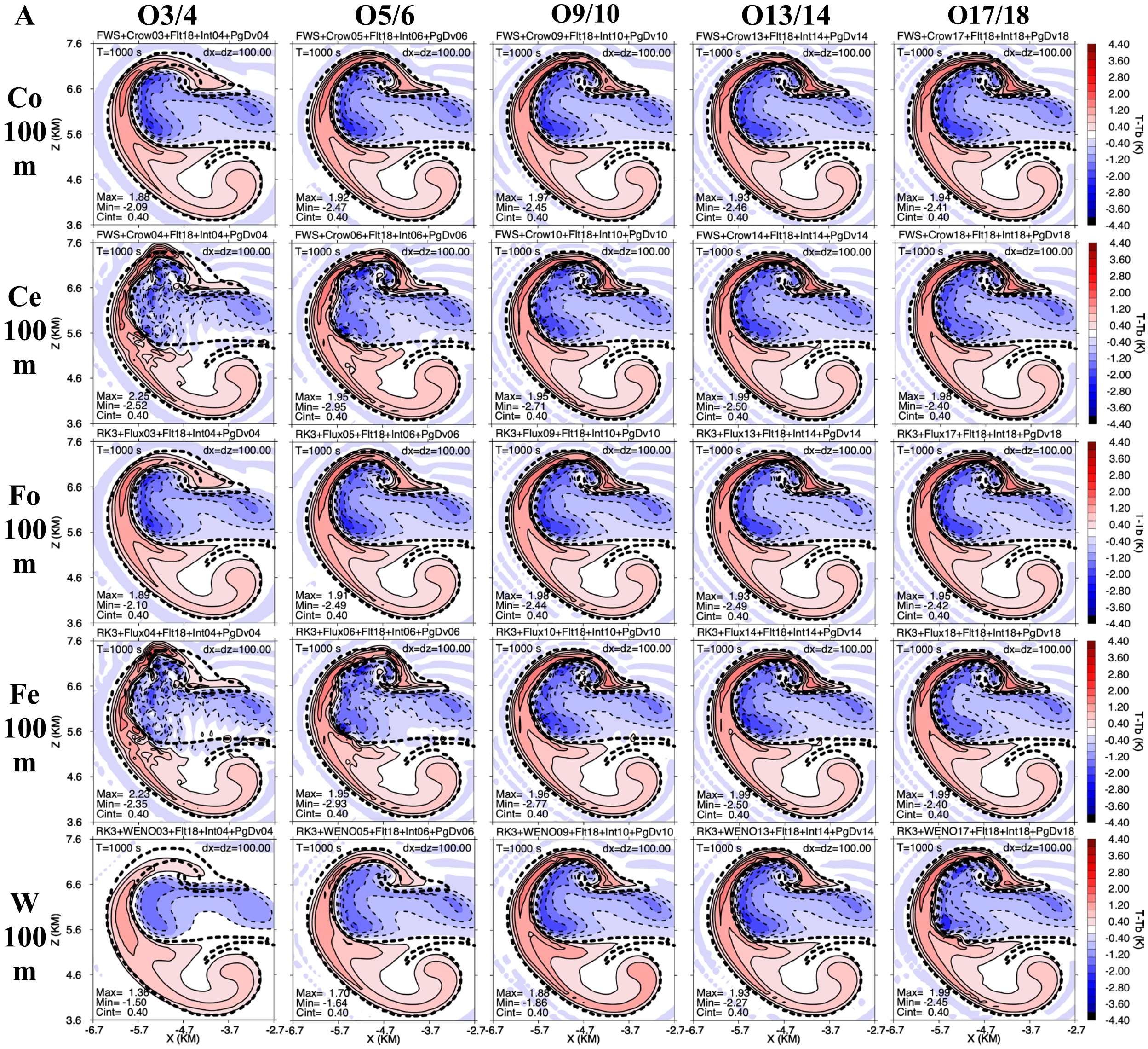

FIGURE 3. Set A perturbation potential temperature ($T - T_b$; K) fields at t = 1000 s made with grid resolution $\Delta x = \Delta z$ = 100 m, with odd/even order O3/4, 5/6, 9/10, 13/14, and 17/18 upwind-biased/centred constant grid flux Crowley (Co = odd; Ce = even), odd/even order upwind-biased/centred constant grid flux (Fo = odd; Fe = even), and WENO flux (W) schemes, comparable order interpolations and pressure gradient/divergence, O18 spatial filter, same Courant number C, and constant eddy mixing coefficient of $K_m = 10$ m^2 s^{-1}. Maximum (Max) and minimum (Min) values and contour interval (Cint) values are on each plot. The bold dashed line is the 0.2 K perturbation potential temperature contour of the upwind-biased constant grid flux O17, 25 m reference solution interpolated to the grid in the plot. Only a left-side subdomain from x = –6.7 to –2.7 km and z = 3.6 to 7.6 km is shown.

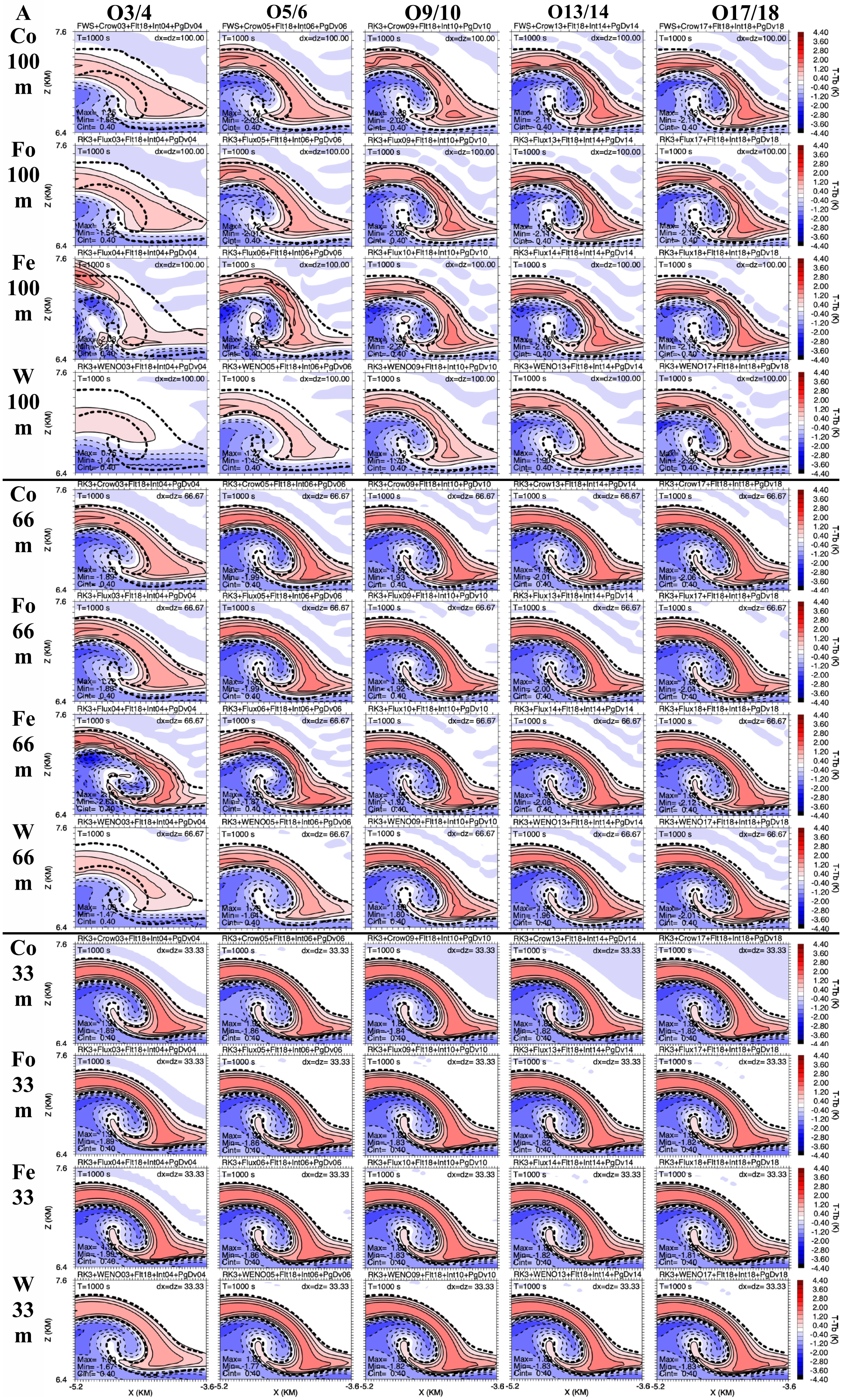
A
O3/4
O5/6
O9/10
O13/14
O17/18
Co 100 m
Fo 100 m
Fe 100 m
W 100 m
Co 66 m
Fo 66 m
Fe 66 m
W 66 m
Co 33 m
Fo 33 m
Fe 33
W 33 m
FWS+Crow03+Flt18+Int04+PgDv04
FWS+Crow05+Flt18+Int06+PgDv06
RK3+Crow09+Flt18+Int10+PgDv10
FWS+Crow13+Flt18+Int14+PgDv14
FWS+Crow17+Flt18+Int18+PgDv18
RK3+Flux03+Flt18+Int04+PgDv04
RK3+Flux05+Flt18+Int06+PgDv06
RK3+Flux09+Flt18+Int10+PgDv10
RK3+Flux13+Flt18+Int14+PgDv14
RK3+Flux17+Flt18+Int18+PgDv18
RK3+Flux04+Flt18+Int04+PgDv04
RK3+Flux06+Flt18+Int06+PgDv06
RK3+Flux10+Flt18+Int10+PgDv10
RK3+Flux14+Flt18+Int14+PgDv14
RK3+Flux18+Flt18+Int18+PgDv18
RK3+WENO03+Flt18+Int04+PgDv04
RK3+WENO05+Flt18+Int06+PgDv06
RK3+WENO09+Flt18+Int10+PgDv10
RK3+WENO13+Flt18+Int14+PgDv14
RK3+WENO17+Flt18+Int18+PgDv18
RK3+Crow03+Flt18+Int04+PgDv04
RK3+Crow05+Flt18+Int06+PgDv06
RK3+Crow09+Flt18+Int10+PgDv10
RK3+Crow13+Flt18+Int14+PgDv14
RK3+Crow17+Flt18+Int18+PgDv18
T=1000 s
dx=dz=100.00
dx=dz= 66.67
dx=dz= 33.33
Cint= 0.40
Z (KM)
X (KM)
7.6
6.4
-5.2
-3.6
T-Tb (K)
4.40
3.60
2.80
2.00
1.20
0.40
-0.40
-1.20
-2.00
-2.80
-3.60
-4.40

FIGURE 4 Set A perturbation potential temperature ($T - T_b$; K) fields at t = 1000 s made with grid resolutions $\Delta x = \Delta z$ = 100, 66.66, and 33.33 m, with odd order O3, 5, 9, 13, and 17 upwind-biased constant grid flux Crowley (Co), odd/even order O3/4, 5/6, 9/10, 13/14, and 17/18 upwind-biased/centred constant grid flux (Fo = odd; Fe = even), and WENO flux (W) schemes, comparable order interpolations and pressure gradient/divergence, O18 spatial filter, same Courant number C, and constant eddy mixing coefficient of K_m = 10 $\mathrm{m^2\,s^{-1}}$. Maximum (Max) and minimum (Min) values and contour interval (Cint) values are on each plot. The bold dashed line is the 0.2 K perturbation potential temperature contour of the upwind-biased constant grid flux O17, 25 m reference solution interpolated to the grid in each plot. Only a zoomed-in sub-domain from x = –5.2 to –3.6 km and z = 6.4 to 7.6 km on the left side of the simulation domain is shown.

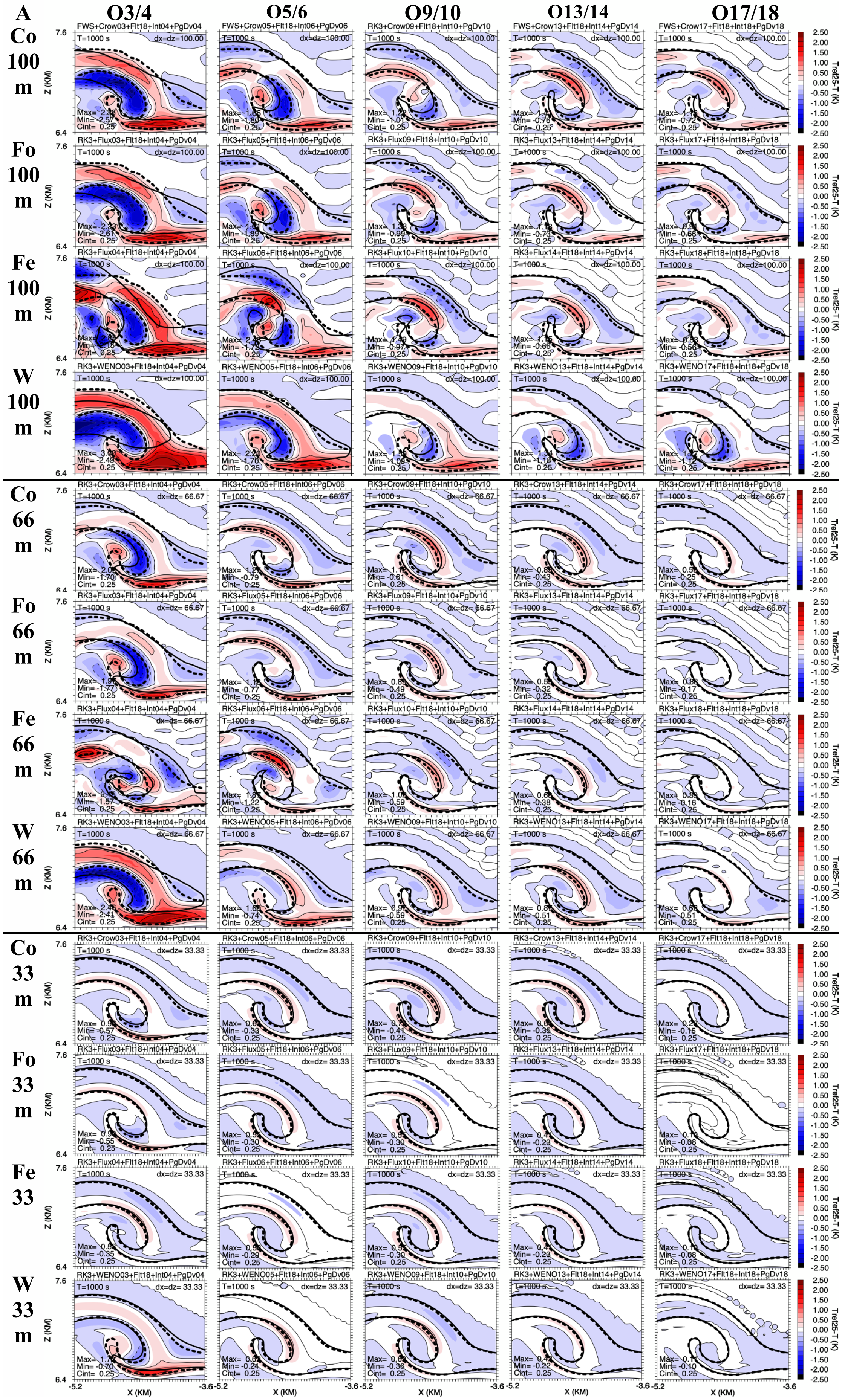
A
O3/4
O5/6
O9/10
O13/14
O17/18
Co
100
m
Fo
100
m
Fe
100
m
W
100
m
Co
66
m
Fo
66
m
Fe
66
m
W
66
m
Co
33
m
Fo
33
m
Fe
33
W
33
m
FWS+Crow03+Flt18+Int04+PgDv04
FWS+Crow05+Flt18+Int06+PgDv06
RK3+Crow09+Flt18+Int10+PgDv10
FWS+Crow13+Flt18+Int14+PgDv14
FWS+Crow17+Flt18+Int18+PgDv18
RK3+Flux03+Flt18+Int04+PgDv04
RK3+Flux05+Flt18+Int06+PgDv06
RK3+Flux09+Flt18+Int10+PgDv10
RK3+Flux13+Flt18+Int14+PgDv14
RK3+Flux17+Flt18+Int18+PgDv18
RK3+Flux04+Flt18+Int04+PgDv04
RK3+Flux06+Flt18+Int06+PgDv06
RK3+Flux10+Flt18+Int10+PgDv10
RK3+Flux14+Flt18+Int14+PgDv14
RK3+Flux18+Flt18+Int18+PgDv18
RK3+WENO03+Flt18+Int04+PgDv04
RK3+WENO05+Flt18+Int06+PgDv06
RK3+WENO09+Flt18+Int10+PgDv10
RK3+WENO13+Flt18+Int14+PgDv14
RK3+WENO17+Flt18+Int18+PgDv18
RK3+Crow03+Flt18+Int04+PgDv04
RK3+Crow05+Flt18+Int06+PgDv06
RK3+Crow09+Flt18+Int10+PgDv10
RK3+Crow13+Flt18+Int14+PgDv14
RK3+Crow17+Flt18+Int18+PgDv18
T=1000 s
dx=dz=100.00
dx=dz= 66.67
dx=dz= 33.33
Cint= 0.25
Z (KM)
X (KM)
7.6
6.4
-5.2
-3.6
Tref25-T (K)
2.50
2.00
1.50
1.00
0.50
0.00
-0.50
-1.00
-1.50
-2.00
-2.50

FIGURE 5 Set A difference between reference and test potential temperature ($T_{Ref} - T$; K) fields at t = 1000 s made with grid resolutions $\Delta x = \Delta z$ = 100, 66.66, and 33.33 m, with odd order O3, 5, 9, 13, and 17 upwind-biased constant grid flux Crowley (Co), odd/even order O3/4, 5/6, 9/10, 13/14, and 17/18 upwind-biased/centred constant grid flux (Fo = odd; Fe = even), and WENO flux (W) schemes, comparable order interpolations and pressure gradient/divergence, O18 spatial filter, same Courant number C, and constant eddy mixing coefficient of K_m = 10 m^2 s^{-1}. Maximum (Max) and minimum (Min) values and contour interval (Cint) are on each plot. The bold dashed line is the 0.2 K perturbation potential temperature contour of the upwind-biased constant grid flux O17, 25 m reference solution interpolated to the grid in each plot. The bold solid line is the 0.2 K perturbation potential temperature contour of the simulation in the plot. Only a zoomed-in sub-domain from x = –5.2 to –3.6 km and z = 6.4 to 7.6 km on the left side of the simulation domain is shown.

Suggestion for shorter figure caption:
FIGURE 5 As in Fig. 4, except for the difference between reference and test potential temperature (T_{Ref} – T; K). The bold dashed line is the 0.2 K perturbation potential temperature contour of the upwind-biased constant grid flux O17, 25 m reference solution interpolated to the grid in each plot. The bold solid line is the 0.2 K perturbation potential temperature contour of the simulation in the plot.

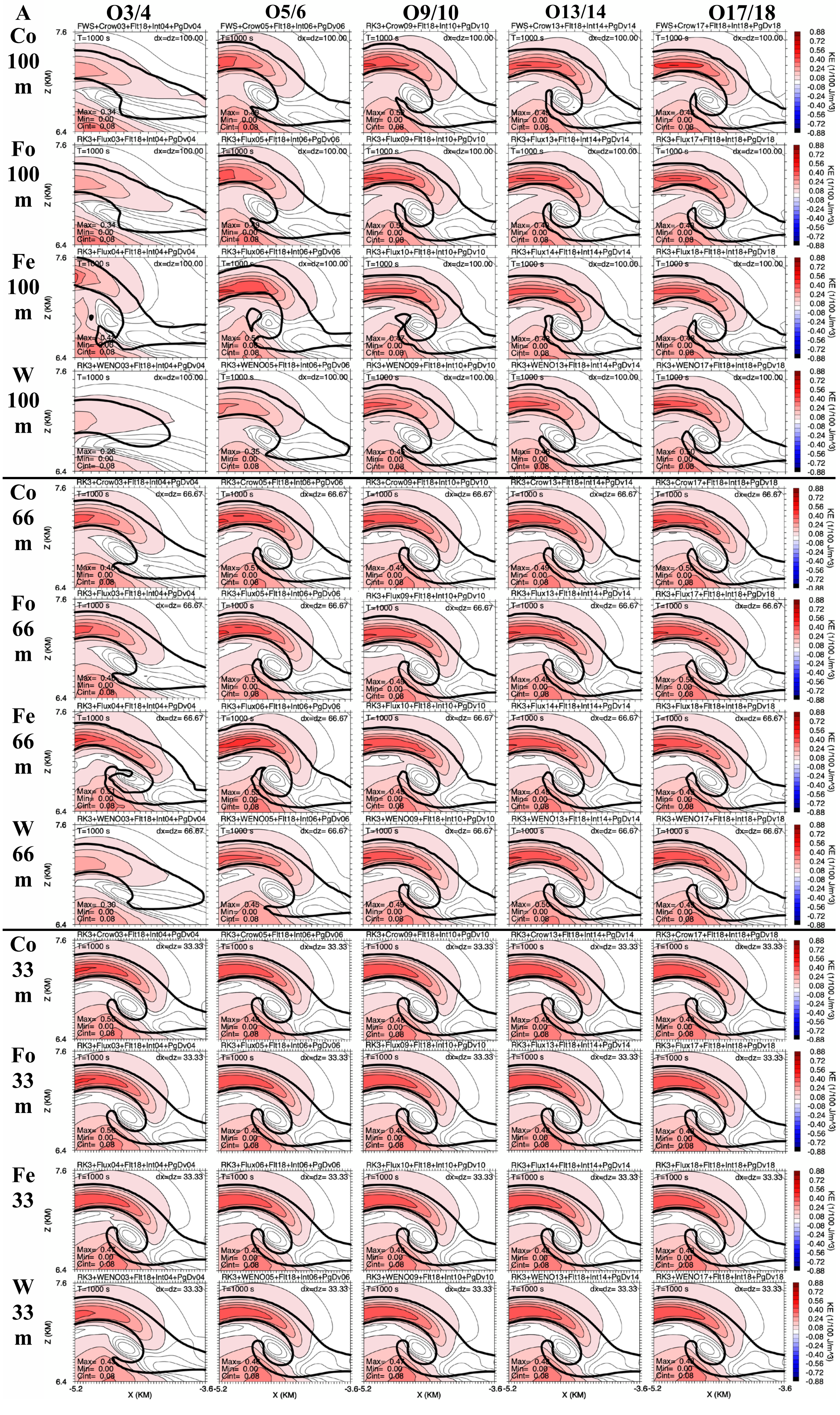
A
O3/4
O5/6
O9/10
O13/14
O17/18
Co 100 m
Fo 100 m
Fe 100 m
W 100 m
Co 66 m
Fo 66 m
Fe 66 m
W 66 m
Co 33 m
Fo 33 m
Fe 33
W 33 m
FWS+Crow03+Flt18+Int04+PgDv04
FWS+Crow05+Flt18+Int06+PgDv06
RK3+Crow09+Flt18+Int10+PgDv10
FWS+Crow13+Flt18+Int14+PgDv14
FWS+Crow17+Flt18+Int18+PgDv18
RK3+Flux03+Flt18+Int04+PgDv04
RK3+Flux05+Flt18+Int06+PgDv06
RK3+Flux09+Flt18+Int10+PgDv10
RK3+Flux13+Flt18+Int14+PgDv14
RK3+Flux17+Flt18+Int18+PgDv18
RK3+Flux04+Flt18+Int04+PgDv04
RK3+Flux06+Flt18+Int06+PgDv06
RK3+Flux10+Flt18+Int10+PgDv10
RK3+Flux14+Flt18+Int14+PgDv14
RK3+Flux18+Flt18+Int18+PgDv18
RK3+WENO03+Flt18+Int04+PgDv04
RK3+WENO05+Flt18+Int06+PgDv06
RK3+WENO09+Flt18+Int10+PgDv10
RK3+WENO13+Flt18+Int14+PgDv14
RK3+WENO17+Flt18+Int18+PgDv18
RK3+Crow03+Flt18+Int04+PgDv04
RK3+Crow05+Flt18+Int06+PgDv06
RK3+Crow09+Flt18+Int10+PgDv10
RK3+Crow13+Flt18+Int14+PgDv14
RK3+Crow17+Flt18+Int18+PgDv18
T=1000 s
dx=dz=100.00
dx=dz= 66.67
dx=dz= 33.33
Max=
Min= 0.00
Cint= 0.08
Z (KM)
7.6
6.4
X (KM)
-5.2
-3.6
KE (1/100 J/m^3)
0.88
0.72
0.56
0.40
0.24
0.08
-0.08
-0.24
-0.40
-0.56
-0.72
-0.88

FIGURE 6 Set A Kinetic Energy per unit volume (KE; 1/100 J m^{-3}) fields at t = 1000 s made with grid resolutions $\Delta x = \Delta z$ = 100, 66.66, and 33.33 m, with odd order O3, 5, 9, 13, and 17 upwind-biased constant grid flux Crowley (Co), odd/even order O3/4, 5/6, 9/10, 13/14, and 17/18 upwind-biased/centred constant grid flux (Fo = odd; Fe = even), and WENO flux (W) schemes, comparable order interpolations and pressure gradient/divergence, O18 spatial filter, same Courant number C, and constant eddy mixing coefficient of K_m = 10 m^2 s^{-1}. Maximum (Max) and minimum (Min) values and contour interval (Cint) values are on each plot. The bold solid line is the 0.2 K perturbation potential temperature contour of the simulation in the plot. Only a zoomed-in sub-domain from x = –5.2 to –3.6 km and z = 6.4 to 7.6 km on the left side of the simulation domain is shown.

Suggestion for shorter figure caption:
FIGURE 6 As in Fig. 5, except for Kinetic Energy per unit volume (KE; 1/100 J m^{-3}). The bold solid line is the 0.2 K perturbation potential temperature contour of the simulation in the plot.

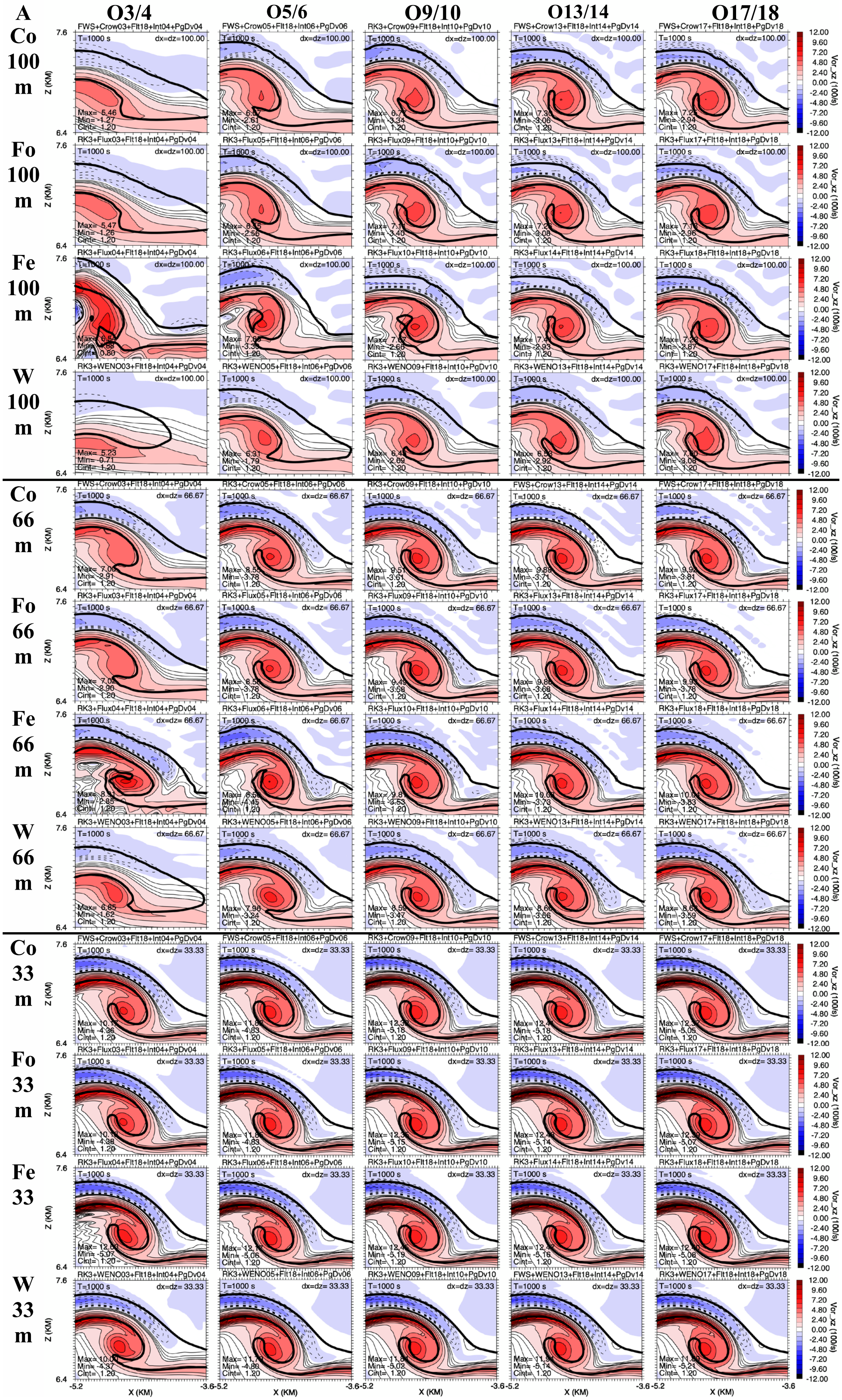
A
O3/4
O5/6
O9/10
O13/14
O17/18
Co 100 m
Fo 100 m
Fe 100 m
W 100 m
Co 66 m
Fo 66 m
Fe 66 m
W 66 m
Co 33 m
Fo 33 m
Fe 33
W 33 m
FWS+Crow03+Flt18+Int04+PgDv04
FWS+Crow05+Flt18+Int06+PgDv06
RK3+Crow09+Flt18+Int10+PgDv10
FWS+Crow13+Flt18+Int14+PgDv14
FWS+Crow17+Flt18+Int18+PgDv18
RK3+Flux03+Flt18+Int04+PgDv04
RK3+Flux05+Flt18+Int06+PgDv06
RK3+Flux09+Flt18+Int10+PgDv10
RK3+Flux13+Flt18+Int14+PgDv14
RK3+Flux17+Flt18+Int18+PgDv18
RK3+Flux04+Flt18+Int04+PgDv04
RK3+Flux06+Flt18+Int06+PgDv06
RK3+Flux10+Flt18+Int10+PgDv10
RK3+Flux14+Flt18+Int14+PgDv14
RK3+Flux18+Flt18+Int18+PgDv18
RK3+WENO03+Flt18+Int04+PgDv04
RK3+WENO05+Flt18+Int06+PgDv06
RK3+WENO09+Flt18+Int10+PgDv10
RK3+WENO13+Flt18+Int14+PgDv14
FWS+WENO13+Flt18+Int14+PgDv14
RK3+WENO17+Flt18+Int18+PgDv18
T=1000 s
dx=dz=100.00
dx=dz= 66.67
dx=dz= 33.33
Max=
Min=
Cint= 1.20
Z (KM)
7.6
6.4
X (KM)
-5.2
-3.6
12.00
9.60
7.20
4.80
2.40
0.00
-2.40
-4.80
-7.20
-9.60
-12.00
Vor_xz (100/s)

FIGURE 7 Set A vorticity (100 s^{-1}) fields at t = 1000 s made with grid resolutions $\Delta x = \Delta z$ = 100, 66.66, and 33.33 m, with odd order O3, 5, 9, 13, and 17 upwind-biased constant grid flux Crowley (Co), odd/even order O3/4, 5/6, 9/10, 13/14, and 17/18 upwind-biased/centred constant grid flux (Fo = odd; Fe = even), and WENO flux (W) schemes, comparable order interpolations and pressure gradient/divergence, O18 spatial filter, same Courant number C, and constant eddy mixing coefficient of K_m = 10 m^2 s^{-1}. Maximum (Max) and minimum (Min) values and contour interval (Cint) values are on each plot. The bold solid line is the 0.2 K perturbation potential temperature contour of the simulation in the plot. Only a zoomed-in sub-domain from x = –5.2 to –3.6 km and z = 6.4 to 7.6 km on the left side of the simulation domain is shown.

Suggestion for shorter figure caption:
FIGURE 7 As in Fig. 6, except for vorticity (100 s^{-1}). The bold solid line is the 0.2 K perturbation potential temperature contour of the simulation in the plot.

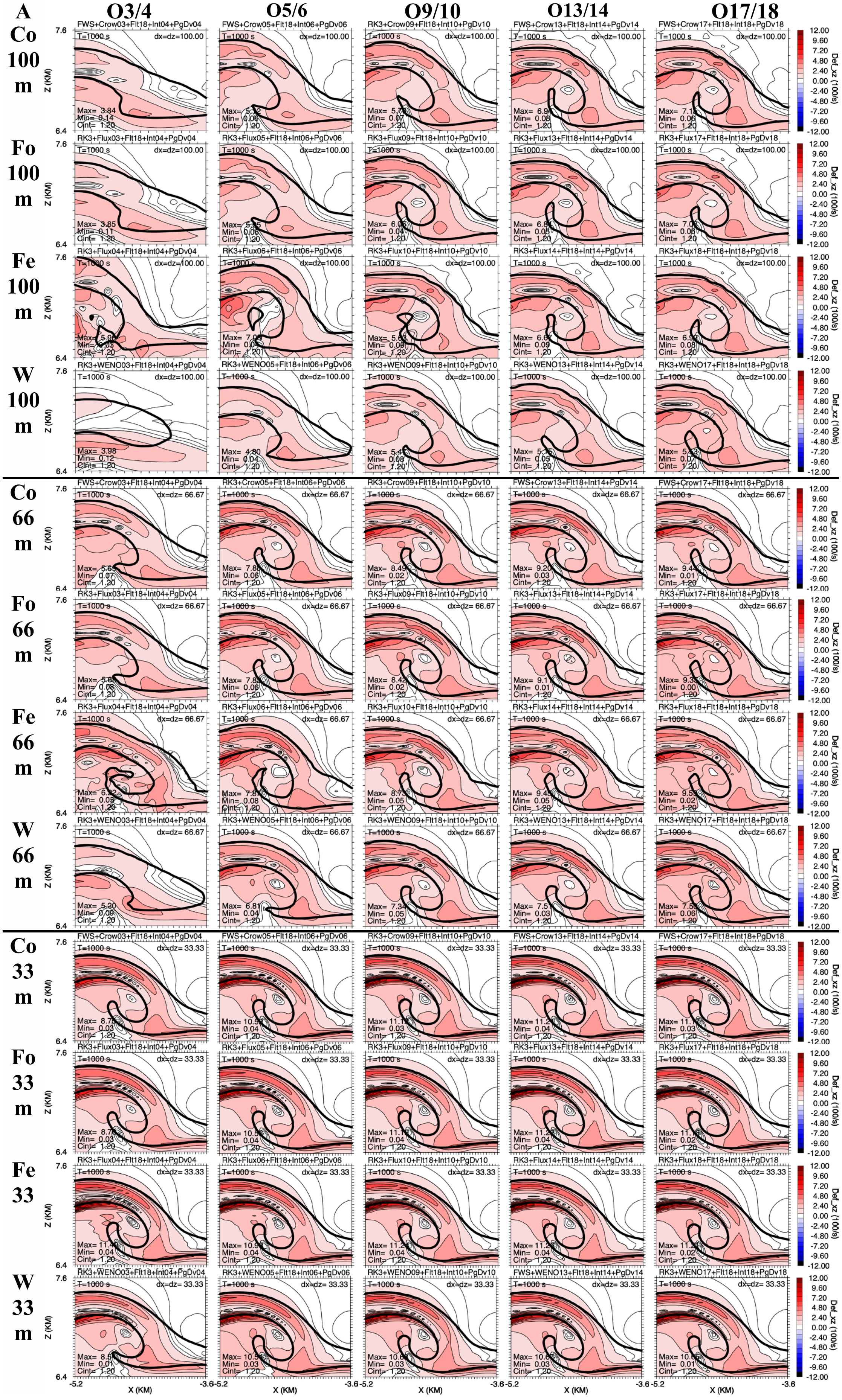
A
O3/4
O5/6
O9/10
O13/14
O17/18
Co 100 m
Fo 100 m
Fe 100 m
W 100 m
Co 66 m
Fo 66 m
Fe 66 m
W 66 m
Co 33 m
Fo 33 m
Fe 33
W 33 m
FWS+Crow03+Flt18+Int04+PgDv04
FWS+Crow05+Flt18+Int06+PgDv06
RK3+Crow05+Flt18+Int06+PgDv06
RK3+Crow09+Flt18+Int10+PgDv10
FWS+Crow13+Flt18+Int14+PgDv14
FWS+Crow17+Flt18+Int18+PgDv18
RK3+Flux03+Flt18+Int04+PgDv04
RK3+Flux05+Flt18+Int06+PgDv06
RK3+Flux09+Flt18+Int10+PgDv10
RK3+Flux13+Flt18+Int14+PgDv14
RK3+Flux17+Flt18+Int18+PgDv18
RK3+Flux04+Flt18+Int04+PgDv04
RK3+Flux06+Flt18+Int06+PgDv06
RK3+Flux10+Flt18+Int10+PgDv10
RK3+Flux14+Flt18+Int14+PgDv14
RK3+Flux18+Flt18+Int18+PgDv18
RK3+WENO03+Flt18+Int04+PgDv04
RK3+WENO05+Flt18+Int06+PgDv06
RK3+WENO09+Flt18+Int10+PgDv10
RK3+WENO13+Flt18+Int14+PgDv14
FWS+WENO13+Flt18+Int14+PgDv14
RK3+WENO17+Flt18+Int18+PgDv18
T=1000 s
dx=dz=100.00
dx=dz= 66.67
dx=dz= 33.33
Max=
Min=
Cint= 1.20
Z (KM)
7.6
6.4
X (KM)
-5.2
-3.6
Del_xz (100/s)
12.00
9.60
7.20
4.80
2.40
0.00
-2.40
-4.80
-7.20
-9.60
-12.00

FIGURE 8 Set A deformation (100 s^{-1}) fields at t = 1000 s made with grid resolutions $\Delta x = \Delta z$ = 100, 66.66, and 33.33 m, with odd order O3, 5, 9, 13, and 17 upwind-biased constant grid flux Crowley (Co), odd/even order O3/4, 5/6, 9/10, 13/14, and 17/18 upwind-biased/centred constant grid flux (Fo = odd; Fe = even), and WENO flux (W) schemes, comparable order interpolations and pressure gradient/divergence, O18 spatial filter, same Courant number C, and constant eddy mixing coefficient of K_m = 10 m^2 s^{-1}. Maximum (Max) and minimum (Min) values and contour interval (Cint) values are on each plot. The bold solid line is the 0.2 K perturbation potential temperature contour of the simulation in the plot. Only a zoomed-in sub-domain from x = –5.2 to –3.6 km and z = 6.4 to 7.6 km on the left side of the simulation domain is shown.

Suggestion for shorter figure caption:

FIGURE 8 As in Fig. 7, except for deformation (100 s^{-1}). The bold solid line is the 0.2 K perturbation potential temperature contour of the simulation in the plot.

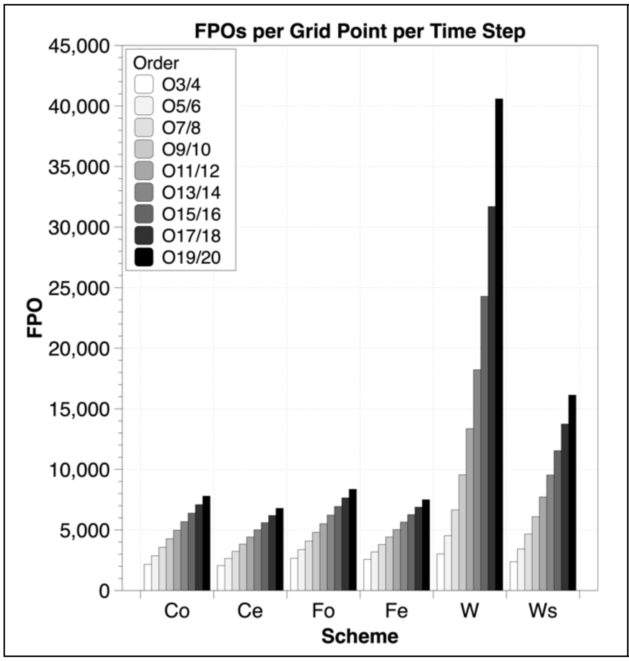

	Scheme	O3/4	O5/6	O9/10	O13/14	O17/18
Total	**Co**	2163	2867	4275	5683	7091
	Ce	2051	2643	3827	5011	6195
	Fo	2665	3377	4801	6225	7649
	Fe	2569	3185	4417	5649	6881
	W	3025	4529	9553	18225	31697
	WS	NA	NA	6097	9537	13745
FLX	**Co**	420	644	1092	1540	1988
	Ce	308	420	644	868	1092
	Fo	432	624	1008	1392	1776
	Fe	336	528	624	816	1008
	W	792	1776	5760	13392	25824
	WS	NA	NA	2304	4704	7872
PD	**RK3**	528	704	1056	1408	1760
	C	576	768	1152	1536	1920
Int	**RK3**	688	1032	1720	2408	3096
	C	576	864	1440	2016	2592
Sum	**RK3**	2233	2753	3793	4833	5873
	C	1743	2223	3183	4143	5103

FIGURE 9 Set A approximate (Total) Floating-Point Operations (FPOs) per grid point per time step for each scheme (left chart), constant grid flux Crowley (Co = odd; Ce = even), flux (Fo = odd; Fe = even), WENO flux (W), and WENO with sine wave-based smoothness indicator (WS; for R≥4, which is ≥O7). The table (right) includes the approximate total floating-point operations (FPO) per grid point per time step (Total) and the FPO for advection (FLX). The bottom six rows of the table contain the approximate FPO for WS02 forward mode-split Crowley (C) and mode-split RK3 time integrations for pressure gradient/divergence (PD); all non-flux interpolations (Int), and the sum (Sum) of FPOs for PD, Int, buoyancy, and filter terms. The FPO values for Sum of PD, Int, buoyancy, and filter terms using O2 and O4 numerical approximations are 1713 and 2233 for mode-split RK3, and 1263 and 1743 for WS02 forward mode-split Crowley, respectively.

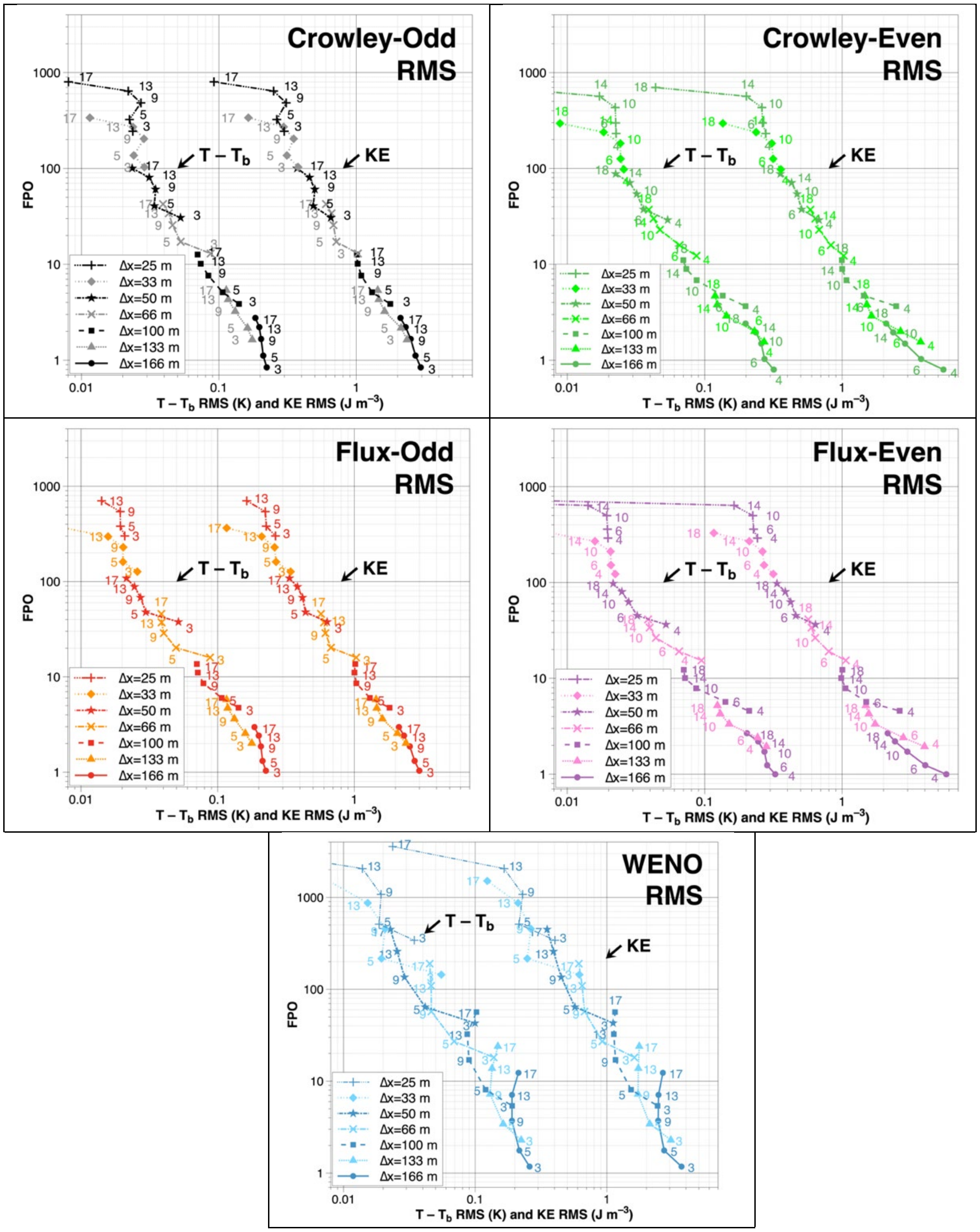

Crowley-Odd RMS

Crowley-Even RMS

Flux-Odd RMS

Flux-Even RMS

WENO RMS

FIGURE 10 Set A log-log charts of the computational cost (total Floating-Point Operations FPO) versus Root Mean Square errors (RMS) for Perturbation potential temperature ($T - T_b$; K; left-most curve cluster in each panel) and Kinetic Energy (KE; J m^{-3}; right-most curve cluster in each panel) calculated against the upwind-biased constant grid flux O17, 25 m reference solution for the odd/even order O3/4, 5/6, 9/10, 13/14, and 17/18 upwind-biased/centred constant grid flux (Co = odd, upper left; Ce = even, upper right) odd/even order O3/4, 5/6, 9/10, 13/14, and 17/18 upwind-biased/centred constant grid flux (Fo = odd, middle left; Fe = even, middle right) and WENO flux (W; bottom) schemes comparable order interpolations and pressure gradient/divergence, O18 spatial filter, same Courant number C, and constant eddy mixing coefficient of $K_m = 10$ m^2 s^{-1} for grid resolutions of $\Delta x = \Delta z = 25$, 33.33, 50, 66.66, 100, 133.33, and 166.66 m (legend). The total FPO values (for all grid points and all timesteps, i.e., the entire simulation) are all normalised by the FPO value for the centred constant grid flux O4 $\Delta x = \Delta z = 166.66$ m simulation for comparison purposes.

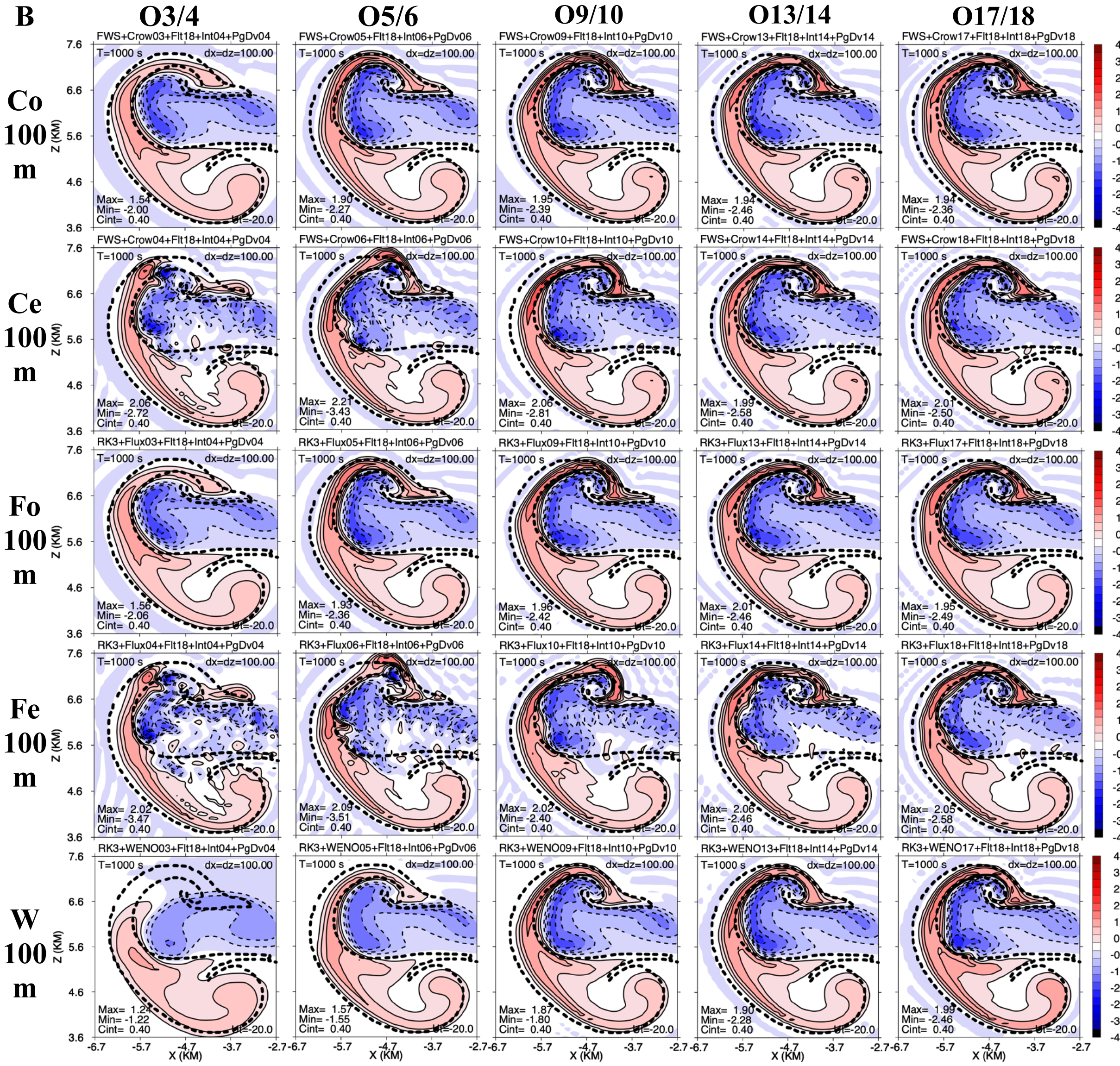

FIGURE 11 Set B perturbation potential temperature ($T - T_b$; K) fields at t = 1000 s made with grid resolution $\Delta x = \Delta z = 100$ m, with an added mean wind of $U_t = -20$ m s^{-1}, odd/even order O3/4, 5/6, 9/10, 13/14, and 17/18 order upwind-biased/centred constant grid flux Crowley (Co = odd; Ce = even), odd/even order upwind-biased/centred constant grid flux (Fo = odd; Fe = even), and WENO flux (W) schemes, comparable order interpolations and pressure gradient/divergence, O18 spatial filter, same Courant number C, and constant eddy mixing coefficient of $K_m = 10$ m^2 s^{-1}. Maximum (Max) and minimum (Min) values and contour interval (Cint) are on each plot. The bold dashed line is the 0.2 K perturbation potential temperature contour of the upwind-biased constant grid flux O17, 25 m reference solution interpolated to the grid in each plot. Only a left-side sub-domain from $x = -6.7$ to -2.7 km and $z = 3.6$ to 7.6 km is shown.

Suggestion for shorter figure caption:

FIGURE 11 As in Fig. 3, except for Perturbation potential temperature (T - T_b K) fields at $t = 1000$ s for simulations in Set B (i.e., with an added mean wind of $U_t = -20$ m s^{-1}). The bold dashed line is the 0.4 K perturbation potential temperature contour of the simulation in the plot.

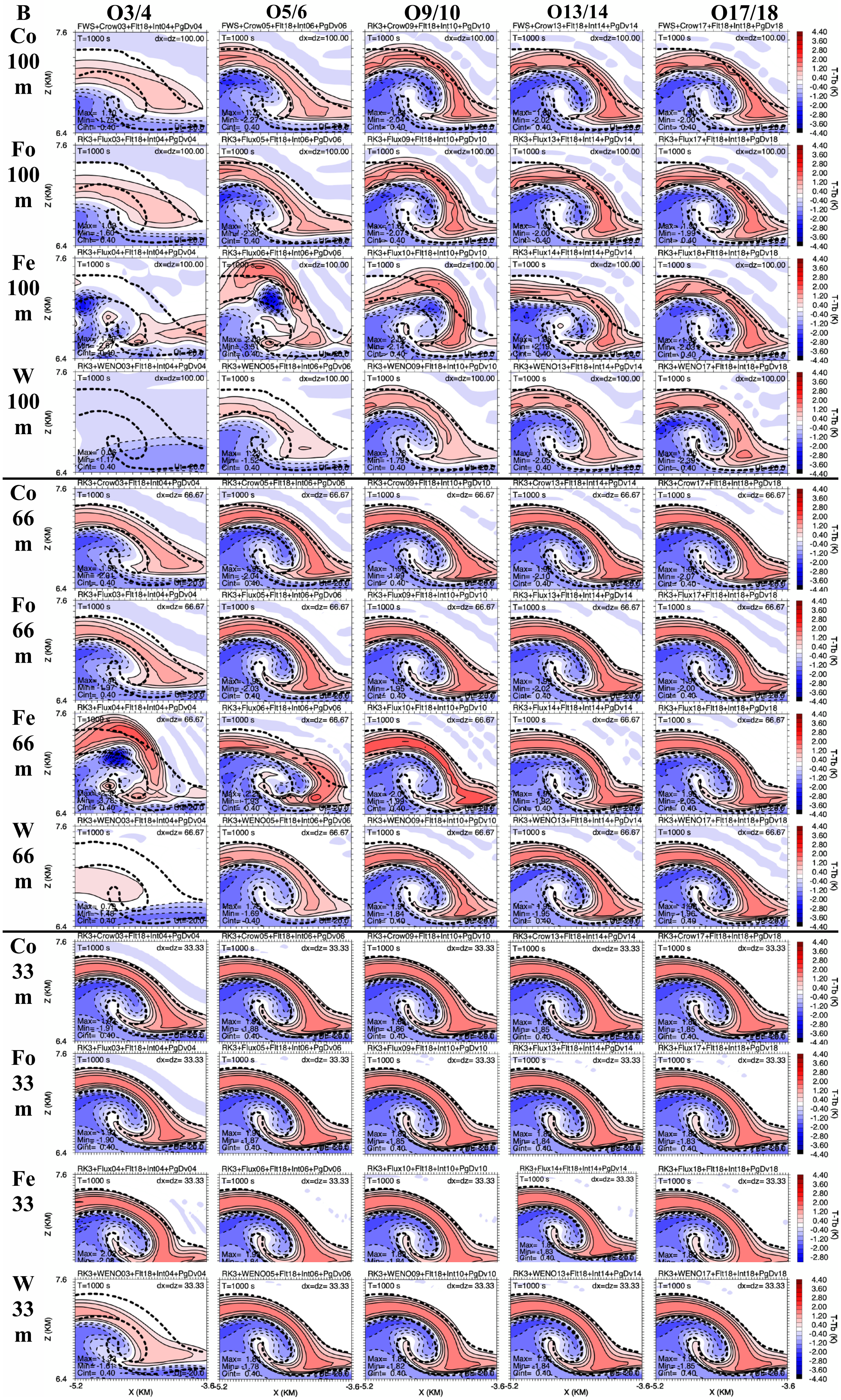
B
O3/4
O5/6
O9/10
O13/14
O17/18
Co 100 m
Fo 100 m
Fe 100 m
W 100 m
Co 66 m
Fo 66 m
Fe 66 m
W 66 m
Co 33 m
Fo 33 m
Fe 33
W 33 m
FWS+Crow03+Flt18+Int04+PgDv04
FWS+Crow05+Flt18+Int06+PgDv06
RK3+Crow09+Flt18+Int10+PgDv10
FWS+Crow13+Flt18+Int14+PgDv14
FWS+Crow17+Flt18+Int18+PgDv18
RK3+Crow03+Flt18+Int04+PgDv04
RK3+Crow05+Flt18+Int06+PgDv06
RK3+Crow13+Flt18+Int14+PgDv14
RK3+Crow17+Flt18+Int18+PgDv18
RK3+Flux03+Flt18+Int04+PgDv04
RK3+Flux05+Flt18+Int06+PgDv06
RK3+Flux09+Flt18+Int10+PgDv10
RK3+Flux13+Flt18+Int14+PgDv14
RK3+Flux17+Flt18+Int18+PgDv18
RK3+Flux04+Flt18+Int04+PgDv04
RK3+Flux06+Flt18+Int06+PgDv06
RK3+Flux10+Flt18+Int10+PgDv10
RK3+Flux14+Flt18+Int14+PgDv14
RK3+Flux18+Flt18+Int18+PgDv18
RK3+WENO03+Flt18+Int04+PgDv04
RK3+WENO05+Flt18+Int06+PgDv06
RK3+WENO09+Flt18+Int10+PgDv10
RK3+WENO13+Flt18+Int14+PgDv14
RK3+WENO17+Flt18+Int18+PgDv18
T=1000 s
dx=dz=100.00
dx=dz= 66.67
dx=dz= 33.33
Cint= 0.40
Z (KM)
7.6
6.4
X (KM)
-5.2
-3.6
T-Tb (K)
4.40
3.60
2.80
2.00
1.20
0.40
-0.40
-1.20
-2.00
-2.80
-3.60
-4.40

FIGURE 12 Set B perturbation potential temperature ($T - T_b$; K) fields at t = 1000 s made with grid resolutions $\Delta x = \Delta z$ = 100, 66.66, and 33.33 m, with an added mean wind of U_t = –20 m s^{-1}, odd order O3, 5, 9, 13, and 17 upwind-biased constant grid flux Crowley (Co = odd; Ce = even), odd/even order O3/4, 5/6, 9/10, 13/14, and 17/18 upwind-biased/centred constant grid flux (Fo = odd; Fe = even), and WENO flux (W) schemes, comparable order interpolations and pressure gradient/divergence, O18 spatial filter, same Courant number C, and constant eddy mixing coefficient of K_m = 10 m^2 s^{-1}. Maximum (Max) and minimum (Min) values and contour interval (Cint) values are on each plot. The bold dashed line is the 0.2 K perturbation potential temperature contour of the upwind-biased constant grid flux O17, 25 m reference solution interpolated to the grid in each plot. Only a zoomed-in sub-domain from x = –5.2 to –3.6 km and z = 6.4 to 7.6 km on the left side of the simulation domain is shown.

Suggestion for shorter figure caption:
FIGURE 12 As in Fig. 4, except for Perturbation potential temperature (T - T_b K) fields at t = 1000 s for simulations in Set B (i.e., with an added mean wind of U_t = –20 m s^{-1}). The bold dashed line is the 0.4 K perturbation potential temperature contour of the simulation in the plot.

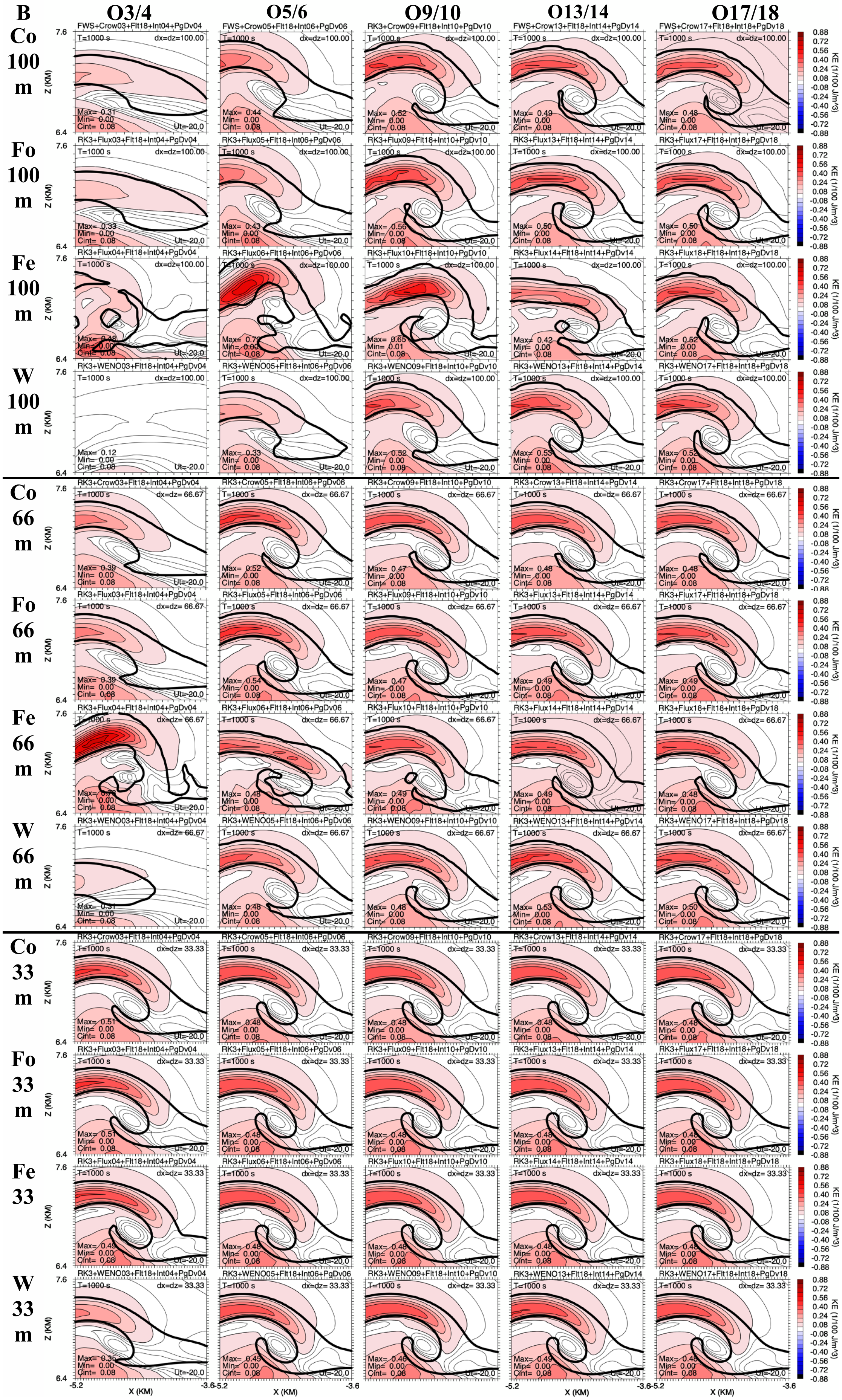
B
O3/4
O5/6
O9/10
O13/14
O17/18
Co 100 m
Fo 100 m
Fe 100 m
W 100 m
Co 66 m
Fo 66 m
Fe 66 m
W 66 m
Co 33 m
Fo 33 m
Fe 33
W 33 m
FWS+Crow03+Flt18+Int04+PgDv04
FWS+Crow05+Flt18+Int06+PgDv06
RK3+Crow09+Flt18+Int10+PgDv10
FWS+Crow13+Flt18+Int14+PgDv14
FWS+Crow17+Flt18+Int18+PgDv18
RK3+Flux03+Flt18+Int04+PgDv04
RK3+Flux05+Flt18+Int06+PgDv06
RK3+Flux09+Flt18+Int10+PgDv10
RK3+Flux13+Flt18+Int14+PgDv14
RK3+Flux17+Flt18+Int18+PgDv18
RK3+Flux04+Flt18+Int04+PgDv04
RK3+Flux06+Flt18+Int06+PgDv06
RK3+Flux10+Flt18+Int10+PgDv10
RK3+Flux14+Flt18+Int14+PgDv14
RK3+Flux18+Flt18+Int18+PgDv18
RK3+WENO03+Flt18+Int04+PgDv04
RK3+WENO05+Flt18+Int06+PgDv06
RK3+WENO09+Flt18+Int10+PgDv10
RK3+WENO13+Flt18+Int14+PgDv14
RK3+WENO17+Flt18+Int18+PgDv18
RK3+Crow03+Flt18+Int04+PgDv04
RK3+Crow05+Flt18+Int06+PgDv06
RK3+Crow09+Flt18+Int10+PgDv10
RK3+Crow13+Flt18+Int14+PgDv14
RK3+Crow17+Flt18+Int18+PgDv18
T=1000 s
dx=dz=100.00
dx=dz= 66.67
dx=dz= 33.33
Max=
Min=
Cint= 0.08
Ut=-20.0
Z (KM)
X (KM)
7.6
6.4
-5.2
-3.6
KE (1/100 J/m^3)
0.88
0.72
0.56
0.40
0.24
0.08
-0.08
-0.24
-0.40
-0.56
-0.72
-0.88

FIGURE 13 Set B Kinetic Energy per unit volume (KE; 1/100 J m^{-3}) fields at t = 1000 s for simulations made with grid resolutions $\Delta x = \Delta z$ = 100, 66.66, and 33.33 m, with an added mean wind of $U_t = -20$ m s^{-1}, odd order O3, 5, 9, 13, and 17 upwind-biased constant grid flux Crowley (Co = odd; Ce = even), odd/even order O3/4, 5/6, 9/10, 13/14, and 17/18 upwind-biased/centred constant grid flux (Fo = odd; Fe = even), and WENO flux (W) schemes, comparable order interpolations and pressure gradient/divergence, O18 spatial filter, same Courant number C, and constant eddy mixing coefficient of K_m = 10 m^2 s^{-1}. Maximum (Max) and minimum (Min) values and contour interval (Cint) values are on each plot. The bold solid line is the 0.2 K perturbation potential temperature contour of the simulation in the plot. Only a zoomed-in sub-domain from x = –5.2 to –3.6 km and z = 6.4 to 7.6 km on the left side of the simulation domain is shown.

Suggestion for shorter figure caption:

FIGURE 13 As in Fig. 12 (i.e., with an added mean wind of $U_t = -20$ m s^{-1}), except for Kinetic Energy per unit volume (KE; 1/100 J m^{-3}). The bold solid line is the 0.2 K perturbation potential temperature contour of the simulation in the plot.

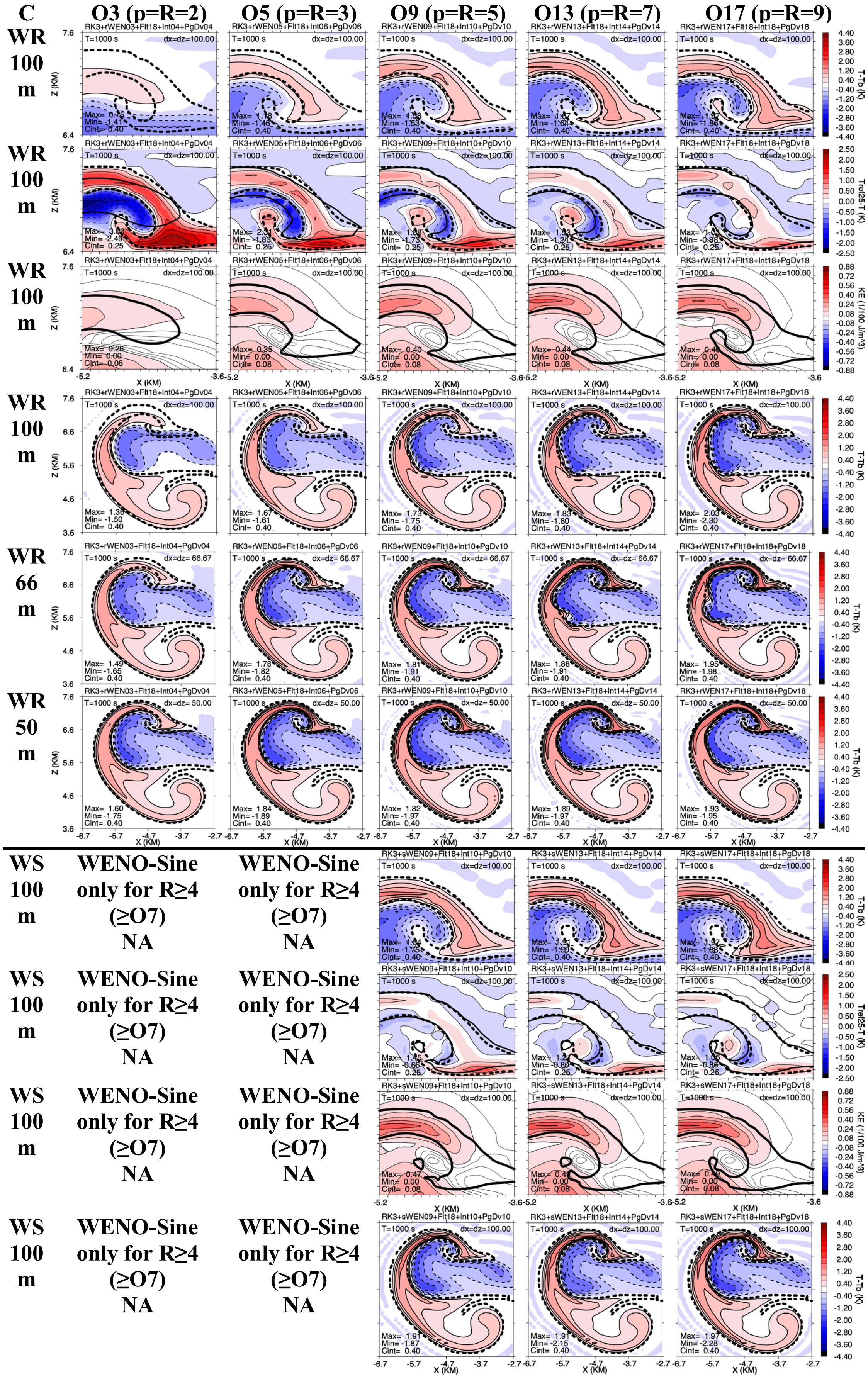
C
O3 (p=R=2)
O5 (p=R=3)
O9 (p=R=5)
O13 (p=R=7)
O17 (p=R=9)
WR 100 m
WR 100 m
WR 100 m
WR 100 m
WR 66 m
WR 50 m
WS 100 m
WS 100 m
WS 100 m
WS 100 m
WENO-Sine only for R≥4 (≥O7) NA
WENO-Sine only for R≥4 (≥O7) NA
RK3+rWENO03+Flt18+Int04+PgDv04
RK3+rWENO05+Flt18+Int06+PgDv06
RK3+rWENO09+Flt18+Int10+PgDv10
RK3+rWEN13+Flt18+Int14+PgDv14
RK3+rWEN17+Flt18+Int18+PgDv18
RK3+sWENO09+Flt18+Int10+PgDv10
RK3+sWEN13+Flt18+Int14+PgDv14
RK3+sWEN17+Flt18+Int18+PgDv18
T=1000 s
dx=dz=100.00
dx=dz= 66.67
dx=dz= 50.00
Z (KM)
X (KM)
T-Tb (K)
Tref25-T (K)
KE (1/100 J/m^3)

FIGURE 14 Set C perturbation potential temperature ($T - T_b$; K; rows one, four, five, six, seven, and ten), difference between reference and test solution potential temperature ($T_{Ref} - T$; K; rows two and eight), and Kinetic Energy per unit volume (KE; 1/100 J m^{-3}; rows three and six) fields at t = 1000 s made with grid resolution of $\Delta x = \Delta z$ = 100 m, with O3, 5, 9, 13, and 17 WENO-R (WR) and O9, 13, and 17 WENO-Sine (WS) flux schemes, comparable order interpolations and pressure gradient/divergence, O18 spatial filter, same Courant number C, and constant eddy mixing coefficient of K_m = 10 m^2 s^{-1}. The top six rows are for the WR solutions with the smoothness indicator exponent parameter given by p = R (G09; order of accuracy given by O = 2R – 1), rather than the traditional value of p = 2 (JS96; S97), with rows four, five, and six WR solutions using 100, 66.66, and 50 m. Rows seven–ten are for the WENO solutions with sine wave-based smoothness indicators (WS in left-hand table) made with p = 1. Row seven is as in row four for perturbation potential temperature ($T - T_b$; K) for the efficient sine wave-exact WENO-Sine (WS) smoothness indicators and p = 1 solution but in the larger sub-domain (compare with Fig. 3; notice the absence of anomalous perturbation potential temperature found for the WENO solutions). Maximum (Max) and minimum (Min) values and contour interval (Cint) are on each plot. The bold solid line is the 0.2 K perturbation potential temperature contour of the simulation in the plot. The bold dashed line is the 0.2 K perturbation potential temperature contour of the upwind-biased constant grid flux O17, 25 m reference solution interpolated to the grid in each plot. Only a zoomed-in sub-domain from x = –5.2 to –3.6 km and z = 6.4 to 7.6 km on the left side of the simulation domain is shown, except in the bottom row where a sub-domain is from x = –6.7 to –2.7 km and z = 3.6 to 7.6 km on the left side of the simulation domain is shown.

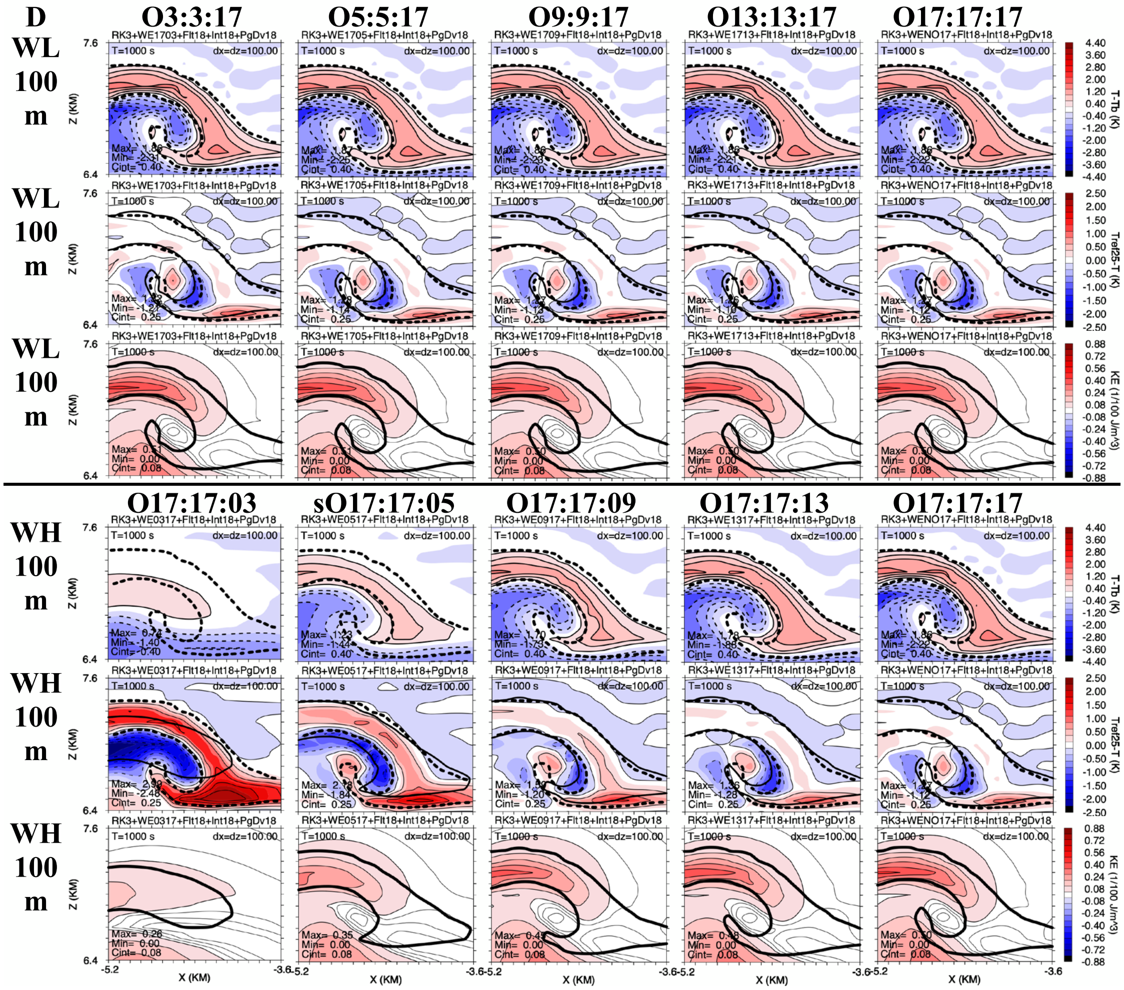

FIGURE 15 Set D perturbation potential temperature ($T - T_b$; K; rows one and four), difference between reference and test solution potential temperature ($T_{Ref} - T$; K; rows two and five), and Kinetic Energy per unit volume (KE; 1/100 J m^{-3}; rows three and six) fields at t = 1000 s made with grid resolution $\Delta x = \Delta z$ = 100 m, with mixed orders of WENO flux for scalars, velocity and pressure, O18 for all interpolations and pressure gradient/divergence, O18 spatial filter, same Courant number C, and constant eddy mixing coefficient of K_m = 10 m^2 s^{-1}. Rows one–three are WENO flux solutions with orders for RK3 time integrations stages one, two and three given by O3:3:17; O5:5:17, O9:9:17, O13:13:17, and O17:17:17 (WL). Rows four– six are WENO flux solutions with orders for RK3 time integrations stages one, two and three given by O17:17:3; O17:17:5, O17:17:9, O17:17:13 (WH). Maximum (Max) and minimum (Min) values and contour interval (Cint) values are on each plot. The bold solid line is the 0.2 K perturbation potential temperature contour of the simulation in the plot. The bold dashed line is the 0.2 K perturbation potential temperature contour of the upwind-biased constant grid flux O17, 25 m reference solution interpolated to the grid in each plot. Only a zoomed-in sub-domain from x = –5.2 to –3.6 km and z = 6.4 to 7.6 km on the left side of the simulation domain is shown.

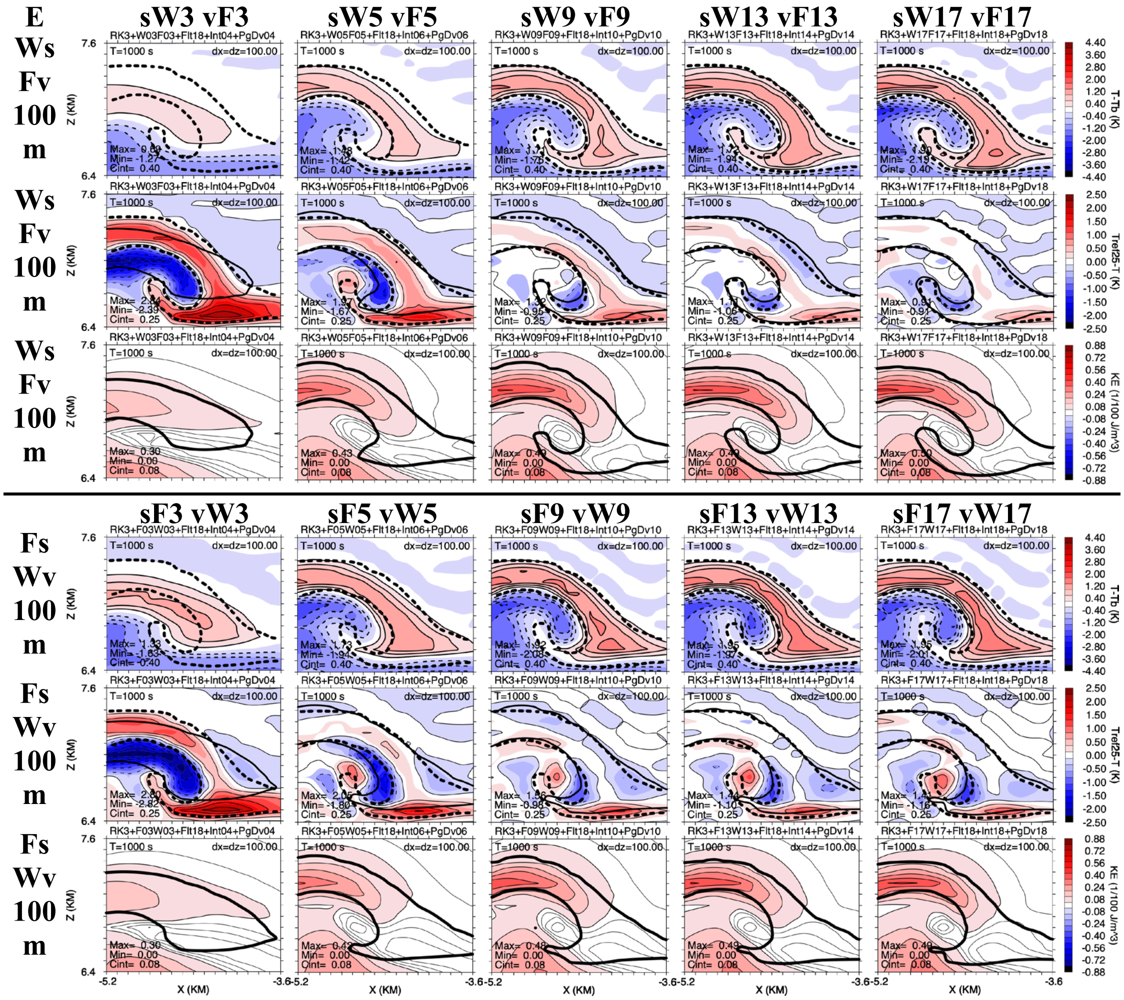

FIGURE 16 Set E perturbation potential temperature ($T - T_b$; K; rows one and four), difference between reference and test solution potential temperature ($T_{Ref} - T$; K; rows two and five), and Kinetic Energy per unit volume (KE; 1/100 J m^{-3}; rows three and six) fields at $t = 1000$ s made with grid resolution $\Delta x = \Delta z = 100$ m, with hybrids of order O3, 5, 9, 13 and 17 WENO flux schemes and comparable odd order upwind-biased constant grid flux, O18 for all interpolations and pressure gradient/divergence, O18 spatial filter, same Courant number C, and constant eddy mixing coefficient of $K_m = 10$ m^2 s^{-1}. The top three rows are for order O3, 5, 9, 13, and O17 WENO flux for scalars (Ws) and comparable order constant grid flux for velocity and pressure (Fv). The bottom three rows are for O3, 5, 9, 13, and 17 WENO flux for velocity and pressure (Wv) and comparable order constant grid flux for scalars (Fs). Maximum (Max) and minimum (Min) values and contour interval (Cint) values are on each plot. The bold dashed line is the 0.2 K perturbation potential temperature contour of the upwind-biased constant grid flux O17, 25 m reference solution interpolated to the grid in each plot. The bold solid line is the 0.2 K perturbation potential temperature contour of the simulation in the plot. Only a zoomed-in sub-domain from $x = -5.2$ to -3.6 km and $z = 6.4$ to 7.6 km on the left side of the simulation domain is shown.

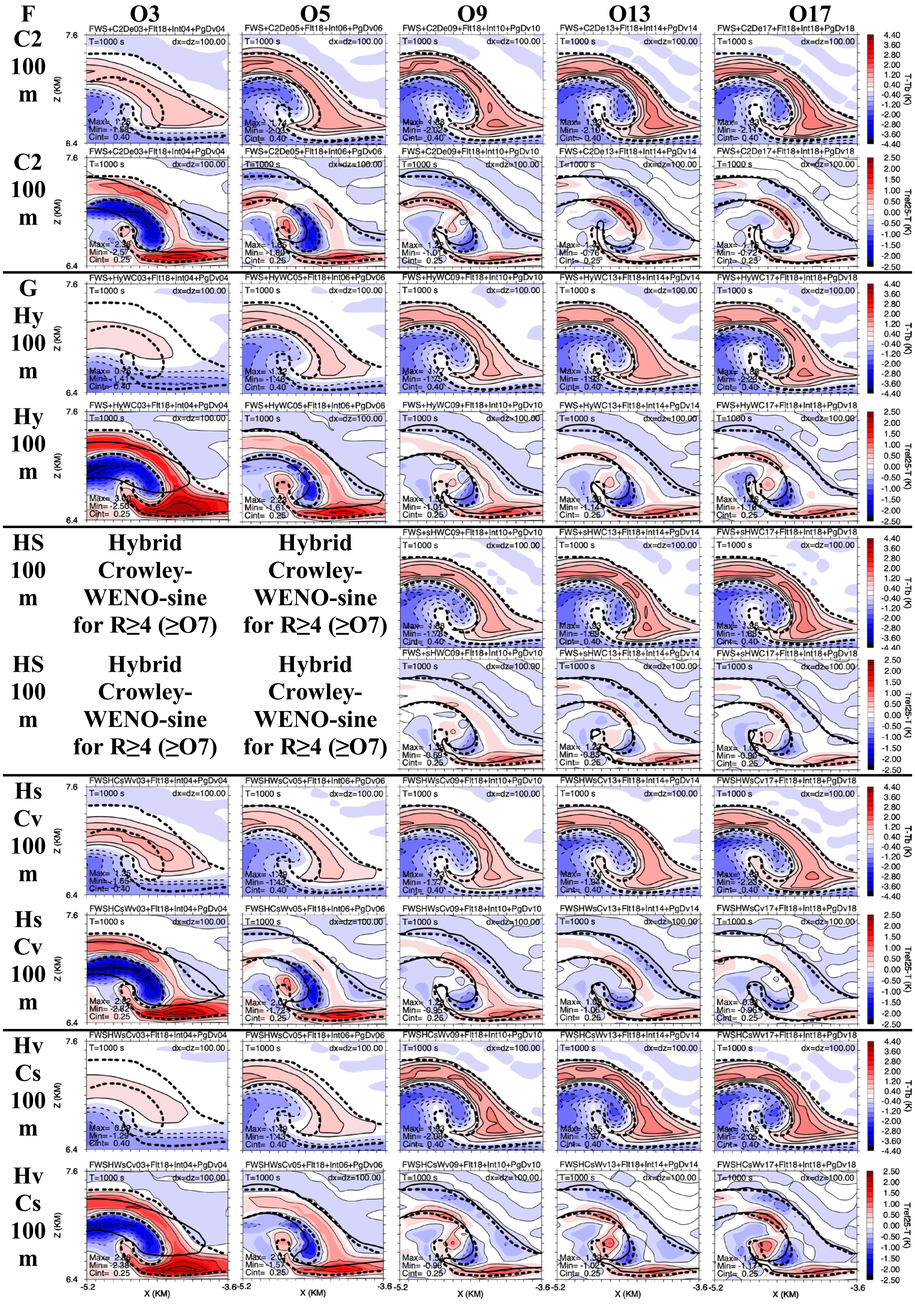

FIGURE 17 Sets F and G Perturbation potential temperature ($T - T_b$; K; rows one, three, five, seven, and nine) and difference between reference and test solution potential temperature ($T_{Ref} - T$; K; rows two, four, six, eight and ten) at t = 1000 s made with grid resolution $\Delta x = \Delta z$ = 100 m, with odd order O3, 5, 9, 13, and 17 upwind-biased constant grid flux Crowley and hybrid-WENO/Crowley schemes, comparable order interpolations and pressure gradient/divergence, O18 spatial filter, same Courant number C, and constant eddy mixing coefficient of K_m = 10 m^2 s^{-1}. The top two rows are for upwind-biased odd order O3, 5, 9, 13, and 17 constant grid flux Crowley scheme using only the stabilizing second derivative (C2), rather than N

derivatives for an Nth order scheme. Rows three and four are for hybrid-WENO/Crowley (Hy) flux schemes (Set G in rows three and four and all remaining rows). Rows five and six are for hybrid-WENO/Crowley flux schemes made with sine wave-based WENO-s smoothness indicators and $p = 1$ (HS). Rows seven and eight are for hybrid-WENO/Crowley flux schemes for scalars (Hs) and Crowley for velocity and pressure (Cv). Rows nine and ten for hybrid-WENO/Crowley fluxes on velocities and pressure (Hv) and Crowley on scalars (Cs). Maximum (Max) and minimum (Min) values and contour interval (Cint) values are on each plot. The bold dashed line is the 0.2 K perturbation potential temperature contour of the upwind-biased constant grid flux O17, 25 m reference solution interpolated to the grid in each plot. The bold solid line is the 0.2 K perturbation potential temperature contour of the simulation in the plot. Only a zoomed-in subdomain from $x = -5.2$ to -3.6 km and $z = 6.4$ to 7.6 km on the left side of the simulation domain is shown.

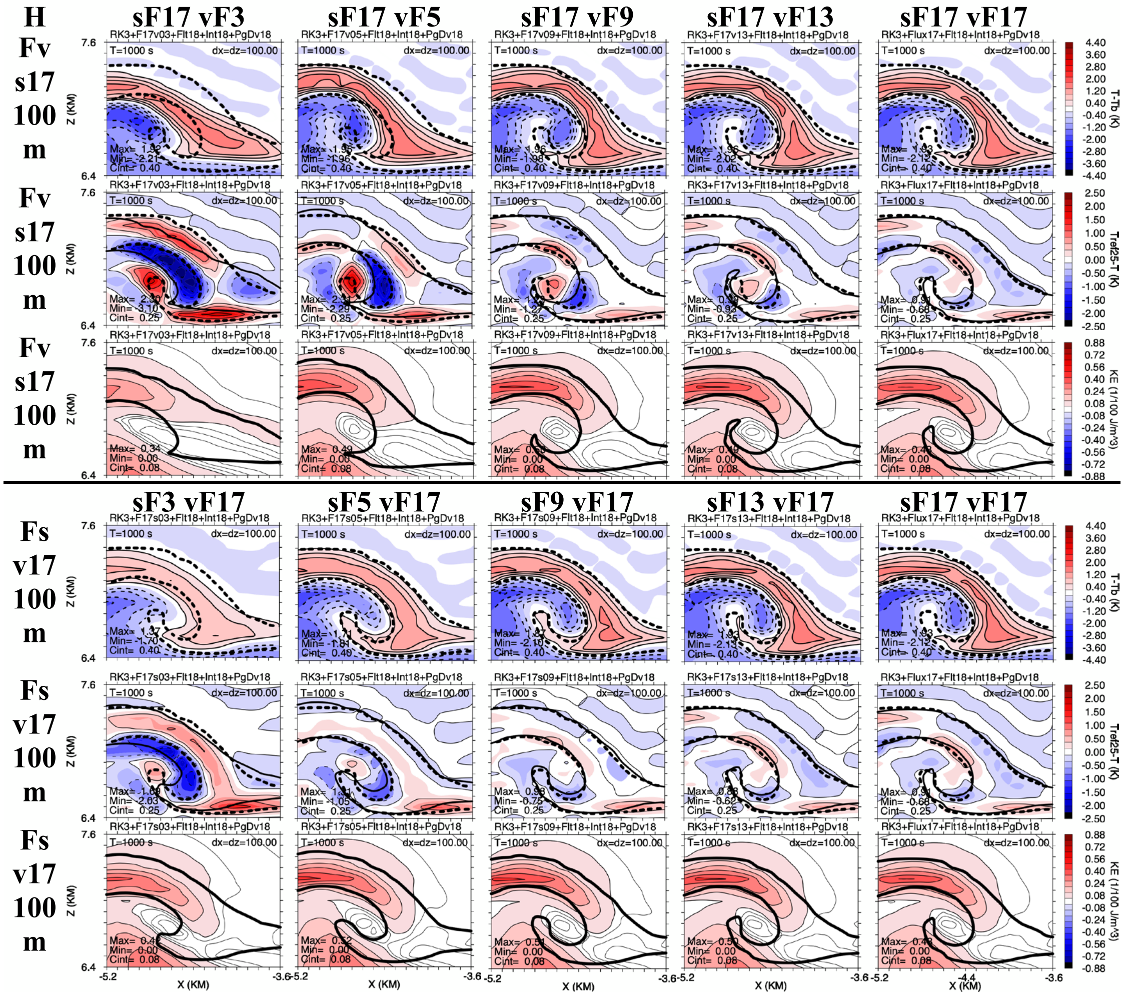

FIGURE 18 Set H perturbation potential temperature ($T - T_b$; K; rows one and four), difference between reference and test solution potential temperature ($T_{Ref} - T$; K; rows two and five), and Kinetic Energy per unit volume (KE; 1/100 J m^{-3}; rows three and six) fields at t = 1000 s made with grid resolution $\Delta x = \Delta z$ = 100 m, with O3, 5, 9, 13, and 17 constant grid flux schemes, all with O18 interpolations and pressure gradient/divergence, O18 spatial filter, same Courant number C, and eddy mixing coefficient of K_m = 10 m^2 s^{-1}. The top three rows are for odd order O3, 5, 9, 13, and 17 constant grid flux schemes for velocity and pressure (Fv) and the O17 constant grid flux scheme for scalars (s17). The second three rows are for odd order O3, 5, 9, 13, and 17 constant grid flux schemes for scalars (Fs) and the odd order O17 upwind-biased constant grid flux scheme for velocity and pressure (v17). Maximum (Max) and minimum (Min) values and contour interval (Cint) values are on each plot. The bold dashed line is the 0.2 K perturbation potential temperature contour of the upwind-biased constant grid flux O17, 25 m reference solution interpolated to the grid in each plot. The bold solid line is the 0.2 K perturbation potential temperature contour of the simulation in the plot. Only a zoomed-in sub-domain from x = –5.2 to –3.6 km and z = 6.4 to 7.6 km on the left side of the simulation domain is shown.

APPENDIX A

TABLE AI CFL and critical wave number at which instability appears first based for O1–19 linear odd order upwind biased (by one point) advection schemes with WSO2 O3 Runge-Kutta (LRK3) time integration using and extending the procedures described by Baldauf (2008).

LRK3 ODD	**O1**	**O3**	**O5**	**O7**	**O9**	**O11**	**O13**	**O15**	**O17**	**O19**
CFL	1.256373	1.625891	1.434983	1.243779	1.127174	1.049315	0.9935351	0.9514629	0.9184809	0.8918446
Kcrit	3.141593	2.472898	1.693186	1.763554	1.847447	1.922732	1.988061	2.044338	2.093085	2.135942

TABLE AII CFL and critical wave number at which instability appears first based for O2–20 linear even order centred advection schemes with WSO2 O3 Runge-Kutta (LRK3) time integration using and extending the procedures described by Baldauf (2008).

LRK3 EVEN	**O2**	**O4**	**O6**	**O8**	**O10**	**O12**	**O14**	**O16**	**O18**	**O20**
CFL	1.732051	1.262224	1.092102	1.000839	0.942644	0.901712	0.8710421	0.8470229	0.8275891	0.8114673
Kcrit	1.570796	1.797478	1.936074	2.033371	2.107086	2.165720	2.213967	2.254671	2.289680	2.320252

TABLE AIII CFL at which instability appears first based for O2–20 linear even order centred advection with (LLF) time integration to compare to LRK3. As can be shown, the CFLs for O2–20 linear even order centred advection schemes with WSO2 O3 Runge-Kutta time integrations (see TABLE AII) are always ~1.732051 more than the same order advection and leapfrog time integrations.

LLF EVEN	**O2**	**O4**	**O6**	**O8**	**O10**	**O12**	**O14**	**O16**	**O18**	**O20**
CFL	1.0	0.7287451	0.6305261	0.5778348	0.5442359	0.5206038	0.5028964	0.4890290	0.4778089	0.4685009

APPENDIX B

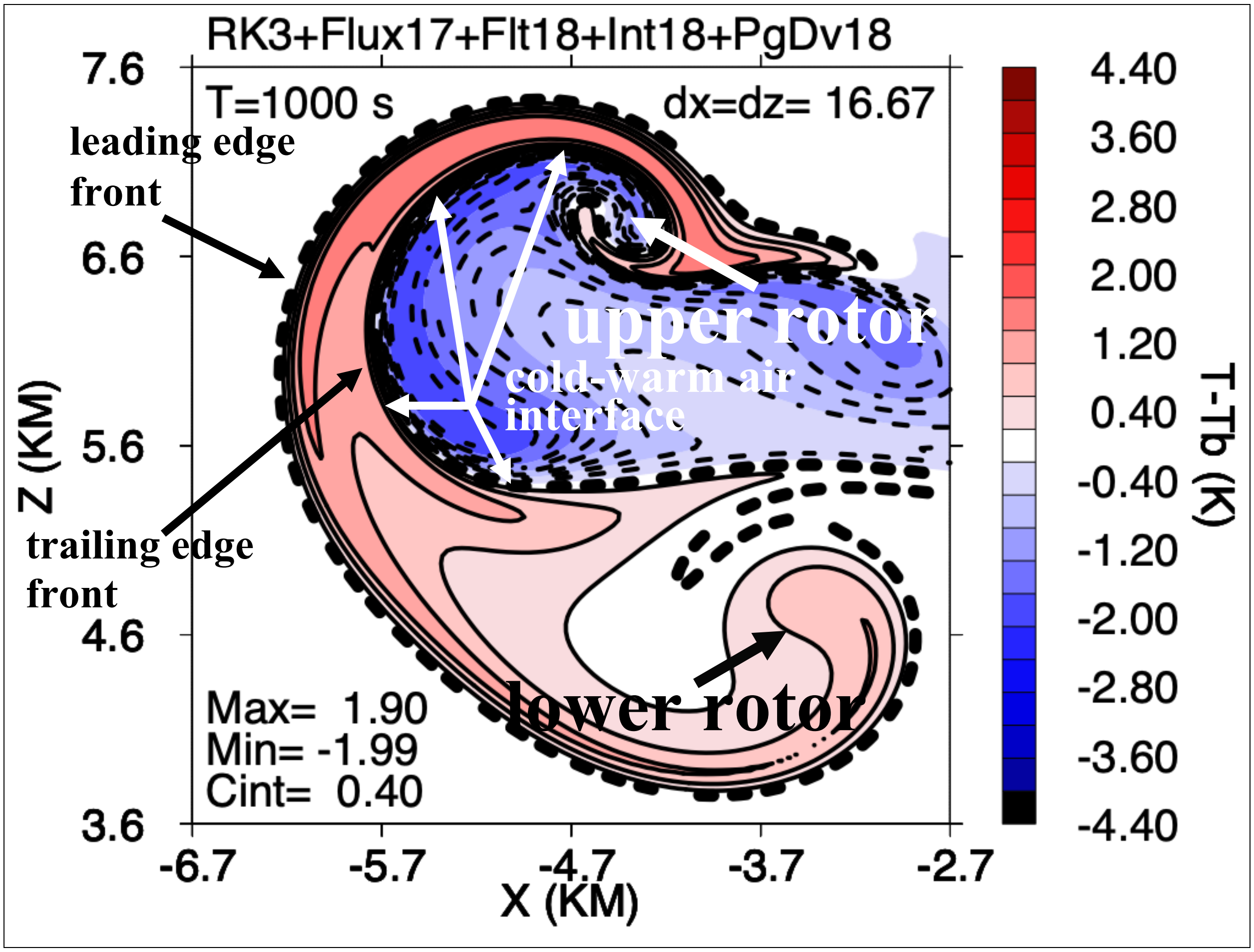

APPENDIX B Locations of flow structures in the perturbation potential temperature field for the colliding plumes circulation in a solution made with O17 constant grid fluxes, O18 interpolations and pressure gradient/divergence, O18 spatial filter, and constant eddy mixing coefficient of $K_m = 10\ \mathrm{m^2\ s^{-1}}$ using $\Delta x = \Delta z = 16.66...$ m and $\Delta t = 0.0520833…$ (adapted from SWK2023).